Spring 2010

Simulation of fluid-structure interaction for surface ships with linear/nonlinear deformations

Kwang Jun Paik
University of Iowa

SIMULATION OF FLUID–STRUCTURE INTERACTION FOR SURFACE SHIPS WITH LINEAR/NONLINEAR DEFORMATIONS

by

Kwang Jun Paik

An Abstract

Of a thesis submitted in partial fulfillment
of the requirements for the Doctor of
Philosophy degree in Mechanical Engineering
in the Graduate College of
The University of Iowa

May 2010

Thesis Supervisor: Associate Professor Pablo M. Carrica

ABSTRACT

The present research develops a numerical fluid–structure interaction (FSI) code based on CFDShip-Iowa version 4, a general-purpose URANS/DES overset fluid solver. Linear and nonlinear FSI methods are developed to compute structural responses on surface ships or marine structures. The modal superposition transient analysis and the nonlinear FEM structure solver are used for small and large deformation FSI problems, respectively.

The gluing method is applied to transfer the forces and displacements on non-matching grids for fluid and structure domains. The linear FEM solver is applied to deform the boundary layer grid with large deformation in the fluid domain, while the deformation is ignored in small deformation problems. Deformation of an interior point in the boundary layer grid is obtained using linear interpolation in both linear and nonlinear deformation problems.

The S175 containership is studied in regular waves as an application example for the linear problem. Heave and pitch responses are compared with the experiments, showing good agreement. Time histories of vertical bending moment (VBM) are calculated using rigid model, one-way coupling, and two-way coupling approaches. The elastic models are able to capture the ringing of the VBM induced by slamming, while the rigid model shows a peak at the moment of slamming without further fluctuations. The two-way coupling method shows the effects of hull deformation on the amplitude and phase of VBM as well as the accelerations of heave and pitch.

For the nonlinear deformation problem three sloshing tanks with an elastic bar clamped to its bottom or top are simulated and compared with the experiments and other

numerical simulation results. The present simulation results show reasonable agreement with the experiments for bar deformation and free surface elevation. A secondary wave on the free surface is creadted by the vorticity generated from the free surface. The effect of the bar on the sloshing impact is studied comparing dynamic pressure acting on the tank wall without bar, with an elatic bar, and with a rigid bar.

Abstract Approved: _____

Thesis Supervisor

_____

Title and Department

_____

Date

SIMULATION OF FLUID–STRUCTURE INTERACTION FOR SURFACE SHIPS WITH LINEAR/NONLINEAR DEFORMATIONS

by

Kwang Jun Paik

A thesis submitted in partial fulfillment
of the requirements for the Doctor of
Philosophy degree in Mechanical Engineering
in the Graduate College of
The University of Iowa

May 2010

Thesis Supervisor: Associate Professor Pablo M. Carrica

Graduate College
The University of Iowa
Iowa City, Iowa

CERTIFICATE OF APPROVAL

_____

PH.D. THESIS

_____

This is to certify that the Ph.D. thesis of

Kwang Jun Paik

has been approved by the Examining Committee for the thesis requirement for the Doctor of Philosophy degree in Mechanical Engineering at the May 2010 graduation.

Thesis Committee: _____
Pablo M. Carrica, Thesis Supervisor

_____
Frederick Stern

_____
Ching-Long Lin

_____
H. S. Udaykumar

_____
M. Asghar Bhatti

To my beloved wife, Youngjin

ACKNOWLEDGMENTS

I would like to express the deepest appreciation to my advisor, Associate Professor Pablo M. Carrica, who had supported me thoughout my thesis with his patience and knowledge. This thesis would not have been possible without his guidance, support, and constructive discussions. I would also like to convey my sincere gratitude to my advisory committee, Professors Frederick Stern, Ching-Long Lin, H.S. Udaykumar, and M. Asghar Bhatti. I would like to specially mention the help that I received from Professor Bhatti to develop the structure solver.

I would like to thank Mr. Seung Myun Hwangbo, Dr. Jongsoo Seo, and Mr. Sung Mok Ahn in Samsung Heavy Industries Co., Ltd. who gave me the opportunity to study abroad. I would also like to express my appreciation to Professor Ho Hwan Chun in Pusan National University who inspired me to study for Ph.D. I am grateful to my Korean colleagues in IIHR, especially, Bong Chul, Bonguk, and Dr. Hyun-Se Yoon for the great time we shared together in Iowa.

I am indebted to my parents, my parents-in-law, and my brother for their love, support, and encouragement. I would like to express my special love and gratitude to my wife, Youngjin, my daughter, Jiyun, and my son, Seungmin, who accepted my absences from home-life, but also supported and motivatied through the hard times.

This work is sponsored by the US Office of Naval Research through research grant N00014-06-1-0474 under the administration of Dr. Patrick Purtell. This sponsor is thankfully acknowledged.

ABSTRACT

The present research develops a numerical fluid–structure interaction (FSI) code based on CFDShip-Iowa version 4, a general-purpose URANS/DES overset fluid solver. Linear and nonlinear FSI methods are developed to compute structural responses on surface ships or marine structures. The modal superposition transient analysis and the nonlinear FEM structure solver are used for small and large deformation FSI problems, respectively.

The gluing method is applied to transfer the forces and displacements on non-matching grids for fluid and structure domains. The linear FEM solver is applied to deform the boundary layer grid with large deformation in the fluid domain, while the deformation is ignored in small deformation problems. Deformation of an interior point in the boundary layer grid is obtained using linear interpolation in both linear and nonlinear deformation problems.

The S175 containership is studied in regular waves as an application example for the linear problem. Heave and pitch responses are compared with the experiments, showing good agreement. Time histories of vertical bending moment (VBM) are calculated using rigid model, one-way coupling, and two-way coupling approaches. The elastic models are able to capture the ringing of the VBM induced by slamming, while the rigid model shows a peak at the moment of slamming without further fluctuations. The two-way coupling method shows the effects of hull deformation on the amplitude and phase of VBM as well as the accelerations of heave and pitch.

For the nonlinear deformation problem three sloshing tanks with an elastic bar clamped to its bottom or top are simulated and compared with the experiments and other numerical simulation results. The present simulation results show reasonable agreement with the experiments for bar deformation and free surface elevation. A secondary wave

on the free surface is creadted by the vorticity generated from the free surface. The effect of the bar on the sloshing impact is studied comparing dynamic pressure acting on the tank wall without bar, with an elatic bar, and with a rigid bar.

TALBE OF CONTENTS

LIST OF TABLES

Table

LIST OF FIGURES

Figure

CHAPTER 1

INTRODUCTION

1.1 Background

Fluid–structure interaction (FSI) problems are of special interest for engineers and designers in a wide range of industrial areas including hydrodynamics, aerodynamics, civil engineering, and biomechanics.

In aerodynamics wing flutter as a result of FSI is a critical issue associated with complex phenomena such as boundary layer interactions and flow separation. The importance of reliable and efficient flutter analysis for airplane wings and aircraft-engine turbomachinery blades was described in Chen et al. (2007). Structural dynamic responses of moving fuel-storage tanks with baffles suppressing liquid motion were investigated by Cho and Lee (2003). A nonlinear fluid–structure formulation used by Farhat et al. (2003) predicted aeroelastic parameters for an F-16 fighter. Hansen (2007) investigated aeroelastic instabilities occurred in modern commercial wind turbines due to stall-induced vibrations and classical blade flutter.

Mendes et al. (1999) described the importance of FSI for wind-induced oscillations and aerodynamic stability in long-span bridge, high rise building, high tower, and large dome designs. Maess and Gaul (2007) showed that structural and acoustic behavior of fluid-filled elastic pipes was strongly influenced by the pipe structure coupled with the acoustic fluid at the fluid–structure interface. FSI problems have attracted considerable attention in the biomechanics of blood circulation as well as the design of micromechanical devices (Ishihara and Yoshimur, 2005; Hron and Mádlík, 2007).

In hydrodynamics a typical FSI problem is that of the marine riser, a conductor pipe connecting a fixed or floating offshore platform or vessel to a wellhead at the seabed.

For three decades vortex-induced vibrations on risers caused by currents and waves have been a critical issue (Kirk et al., 1979; Duggal and Niedzwecki, 1995; Chaplin et al., 1997; Le Cunff et al., 2002).

Calculation of unsteady structural loads on surface ships due to ocean waves is another longstanding FSI problem of interest (Watanabe et al. 1989; Fonseca and Guedes Soares, 1998 and 2004a; Singh and Sen, 2007). Most research has been very limited in the simulation of free surface. To overcome this Idelsohn et al. (2006) simulated FSI problems with the free surface, later extending their simulations to more complicated FSI problems incorporating large solid deformation with the free surface (Idelsohn et al., 2008a and 2008b).

In this thesis a numerical method based on an arbitrary Lagrangian–Eulerian (ALE) formulation is developed. The method uses an unsteady Reynolds-averaged Navier–Stokes (URANS) solver based on the finite difference method (FDM) for computational fluid dynamics (CFD) and the modal superposition or the finite element method (FEM) for computational structure dynamics (CSD). This is applied to FSI problems for hydroelastic ship structures on the free surface.

There are three essential components to simulate FSI problems. The first involves choosing numerical methods for fluid and structure solvers and frameworks for fluid and structure references. The second is the coupling of fluid and structure domains. The third is numerical methods for dynamic deformation of fluid grid. The literature review will focus on these components.

1.1.1 Numerical Method Literature Review

Formulations for FSI simulations are categorized into Lagrangian (material), Eulerian (spatial), or arbitrary Lagrangian–Eulerian (ALE) frameworks. The Lagrangian formulation describes convection by placing a set of axes over the material particles that move according to the equations of motion. In the Eulerian formulation, axes are fixed in

space and convection terms are incorporated into equations describing the fluid transport. Therefore, structures are usually described by Lagrangian formulations, while fluids are usually described by Eulerian formulations. Coupling of these approaches is generally accomplished through an ALE formulation for the fluid domain and a Lagrangian formulation for the structure domain. On the other hand, some researchers use Lagrangian or Eulerian formulations exclusively for both fluid and structure domains.

1) Arbitrary Lagrangian–Eulerian (ALE) Formulation

A purely Lagrangian method for the kinematical description of the fluid domain is unable to conveniently treat strong distortions which often characterize flows of interest. On the other hand, if fluid motions were described in Eulerian coordinates, strong distortions could be handled with relative ease (Donea et al., 1982). Therefore, an ALE formulation is applied to model the governing equations for the fluid, while a Lagrangian formulation is applied to the equations for the structure domain.

The finite element method (FEM) is generally used for the structure solver, while a variety of methods such as the finite difference method (FDM), the finite volume method (FVM), or the FEM can serve as the fluid solver in the ALE formulation. For problems with small structural deformations, the modal superposition is computationally economic and very accurate (Feng and Soulaïmani, 2006 and 2007; Chen et al., 2007).

The ALE finite element method is widely applied to free surface, moving boundary, large deformation, and interface contact problems (Braess and Wriggers, 2000; Cho and Lee, 2003; Kuhl et al., 2003; Engel and Griebel, 2006; Hron and Mádlík, 2007). Some researchers applied the FVM rather than the FEM as the fluid solver, using the FEM as the structure solver (Glück et al., 2001; Bathe and Zhang, 2004; Schäfer et al., 2006). Shi and Lim (2007) solved the flow field with the lattice Boltzmann method (LBM), while solid body deformation was solved with the FEM. A distributed Lagrange

multiplier (DLM) imposed kinematical constraints in the solid or fictitious fluid domain. That is known as the LBM-DLM/FD method.

Lv et al. (2007) discretized Cauchy's equations for structural dynamics as well as the fluid solver using the FVM. This permitted simulation of the FSI problem without a matrix. Xia and Lin (2008) introduced a new cell-vortex unstructured FVM for structural dynamics simulations in response to fluid motions. The method incorporated a fluid dynamics solver for structural dynamics, providing a viable alternative to the FEM structural solver.

Other approaches have extended commercial codes for fluid and/or structure solvers to treat FSI problems. Cavagna et al. (2005) attempted to create specific procedures for aeroelastic analysis using "off-the-shelf" software products, such as the commercially available CFD software FLUENT, to effectively solve transonic aeroelastic problems for industrial environments. To simulate light and thin-walled structures undergoing large displacements subjected to highly turbulent air flows, Bletzinger et al. (2006) used an in-house finite element code as the structure solver and the CFD software package CFX-5 as the fluid solver. Sigrist and Garreau (2007) developed a numerical method for the ANSYS finite element code to produce coupled fluid–structure dynamic analysis with pressure-based finite element formulation as the fluid solver and modal/spectral methods as the structure solver.

2) Lagrangian Formulation

The advantage of a Lagrangian formulation for both solids and fluids is in the capability to simulate breaking waves or separated drops without free surface modeling (Idelsohn et al., 2006). Representative numerical methods include the smooth particle hydrodynamics (SPH) and the particle finite element method (PFEM). These are particle methods that do not require numerical grids.

The SPH is a numerical simulation method invented in the seventies (Gingold and Monaghan, 1977; Lucy, 1977). It is an approximation of Monte Carlo's method for gas dynamics problems. This was extended to incompressible flows with the free surface by Monaghan (1994), and can be especially effective for problems characterized by large displacements and rapidly moving free surfaces. It does not require specific treatment for the free surface. Time shift is not introduced into the fluid or solid dynamics calculation, since both media variables are updated simultaneously. Antoci et al. (2007), for example, studied a safety valve for pressure reduction where water pressure deformed an elastic plate. A study of a passive roll-damper for fishing vessel rolling tanks subjected to large amplitude waves and breaking waves using the SPH was conducted by Souto Iglesias et al. (2004, 2006).

Many other methods are derived from the SPH. One that has shown remarkable results is the moving particle semi-implicit (MPS) method introduced by Koshizuka and Oka (1996). This uses a kernel function to interpolate unknowns. The SPH uses a weak formulation, while the MPS uses a strong governing equation form. Lee et al. (2007) introduced a coupled particle and FEM for fluid–shell structure interaction analysis. The MPS method analyzed fluid flow and 4 nodes mixed interpolation tensional component shell element was used in FEM structural analysis. Partitioned coupling was applied between fluid and structural solvers.

The PFEM uses shape functions introduced by the meshless finite element method (MFEM) to approximate partial differential equations representing fluid motion. The continuum is discretized into particles with properties such as density, viscosity, conductivity, etc., as well as variables that define the temporal state such as velocity and position. Other variables, like temperature, are assigned to particles and transported with particle motion. The PFEM provides a very efficient means to solve contact and free surface problems, simplifying FSI treatment (Idelsohn et al., 2006). Idelsohn et al. (2008a,

2008b) simulated interactions between elastic bar and free surface using the PFEM. The particle methods, on the other hand, are unable to resolve boundary layers and local flows.

3) Eulerian Formulation

Numerical approach using Eulerian formulation is not as popular as the Lagrangian or ALE formulation due to complexity involved in deriving structural numerical formulation in Eulerian framework. Liu and Walkington (2001) developed equations governing fluid flow containing visco-hyperelastic particles for Eulerian formulation. Nevertheless, they simplified numerical codes which typically computed the strain on Lagrangian grids moving through Eulerian grids. Dunne and Rannacher (2006) used a technique similar to the level set method and a mesh adaptation method to solve FSI problems in the Eulerian formulation. They showed results similar to the ALE formulation in their benchmark cylinder with elastic bar.

1.1.2 Fluid–Structure Coupling Literature Review

In FSI problems analysis, a coupling strategy to satisfy geometrical compatibility and equilibrium conditions at the fluid–structure interface is key (Ishihara and Yoshimura, 2005). The main FSI solution approaches can be divided roughly into monolithic (fully-coupled, simultaneous) methods and partitioned (staggered, iterative) methods. The monolithic methods tightly couple fluid and structural discrete equations and solve them together. The partitioned methods solve each field separately and solution variables are passed iteratively from field to field until convergence is achieved.

The monolithic methods have drawbacks. The formulation of a single FSI equation system may increase the number of degrees of freedom to solve and result in an ill-conditioned coefficient matrix from a linearized coupled equation system, especially if the structure is very stiffer or heavier than the fluid. It has the advantage that a relatively larger time step can be used, reducing computational time. There is no time lag between the fluid and structure solvers.

The partitioned methods have the advantage that two solvers for the fluid and structure can be developed separately using different numerical methods. Unmatched grids can be used on the interface between the two media. Implementation of boundary conditions at the interface is simpler since it can be carried out explicitly. A drawback is that there is always a time lag between fluid and structure integration; thus, a relatively small time step is required to maintain stability. This can be avoided using subiterations within each time step.

Alonso and Jameson (1994) and Melville et al. (1997) reduced the time lag in the partitioned method using an implicit algorithm to integrate fluid and structure in time. To achieve full coupling, they updated the interaction after each subiteration. Piperno et al. (1995) and Farhat et al. (1995) investigated various partitioned procedures for the transient solution of coupled aeroelastic problems. They gave particular attention to accuracy and stability with subcycling schemes. Farhat et al. (2003) increased the accuracy-order of their conventional partitioned procedures to improve prediction of deformation and aerodynamic forces. An implicit partitioned method based on a predictor–corrector scheme applied to structural displacements within each time step was developed by Glück et al. (2001). Another implicit approach combining the advantages of weakly and strongly coupled schemes in a complementary manner was introduced by Schäfer et al. (2006). Blom (1998) claimed that a partitioned algorithm converged to a fully coupled scheme with increased subiterations. Kuhl et al. (2003) compared the partitioned and monolithic solutions for fluid–structure coupling. They showed that the partitioned solution procedure introduces an artificial energy production and the monolithic solution procedure is much less sensitive to time step values.

When different numerical methods are required for different media, the only choice is the partitioned approach. Bletzinger et al. (2006) had to use the partitioned method for the coupling to accommodate a commercial software for the fluid solver. Lee

et al. (2007) also used the partitioned procedure with MPS subcycling in their Lagrangian formulation.

1.1.3 Dynamic Deformable Grids Literature Review

The solution of coupled fluid/structure dynamic equations requires deforming a fluid grid for each time step. When the fluid solver is treated in ALE formulation, the fluid grid movement can be independent of the fluid motion itself. The grid deformation method within the fluid domain is an important component of the coupled solution procedure. This is particularly true for large structural deformations. No grid folding must occur and grid volumes may be maintained to prevent deterioration of discretization accuracy and solver efficiency.

A spring analogy is a popular method for movement of unstructured grids (Batina, 1990; Blom and Leyland, 1998). The spring analogy is appropriate for small structural displacements, may result in severe grid distortion when structures are subjected to large deformations (Piperno et al., 1995). To prevent grid folding in large deformations, a torsional spring analogy was developed by Farhat et al. (1998b) for 2D problems. This method was extended by Degand and Farhat (2002) to 3D problems. It was further developed by Zeng and Ethier (2005) as a semi-torsional spring analogy and by Markou et al. (2007) as an ortho-semi-torsional spring analogy.

Chen et al. (2007) used an algebraic grid deformation method assuming zero displacement for the outer boundary. Schäfer et al. (2006) compared algebraic and elliptic mesh generation gird movement techniques. The simple algebraic approach, using the linear transfinite interpolation, deteriorated and even folded grids. The elliptic mesh generation techniques, incorporating the Poisson equation, maintained grid quality, particularly for large grid deformations. Kuhl et al. (2003) and Stein et al. (2003) used linear elasticity equations for grid deformations. Feng and Soulaïmani (2007) also assumed that grid movement was governed by elastodynamic equations.

1.2 Objectives and Approach

This thesis develops a fluid–structure interaction code based on CFDShip-Iowa version 4. The objectives are to simulate structural responses on surface ships and marine structures interacting with the free surface, a long standing issue of concern in naval architecture, and to validate the simulation results comparing with experimental data.

CFDShip-Iowa is used for the fluid solver. The numerical method of CFDShip-Iowa is the FDM. The modal superposition and the nonlinear FEM are used for the structure solver. Coupling the two media in the fluid domain is achieved using an ALE formulation. The number of grid points on the ship surface for the structure solver are usually much smaller than those used for the fluid solver. Grids at the interface of fluid and structure do not match. The partitioned method is applied for fluid–structure coupling.

For the moving grid, the spring analogy code is easier to develop than the linear elastic structure solver. The spring analogy is deficient, however, in maintaining boundary layer quality grid and moving the fluid domain outer boundary. The grid volume tends to decrease near the contracted surface and to increase on the expanded surface. The grid shape near the surfaces can deteriorate with large skew angle. The fluid domain outer boundary should be sufficiently distant from the ship surface to allow shrinking of grid for large deformation problems.

CFDShip-Iowa uses body-fitted curvilinear overset grids, so the initial grid quality near the surface wall should be maintained even for large deformations. The outer boundary should be deformed in proportion to the wall surface deformation. Therefore, a linear elastic equation is applied to deform the outer boundary of fluid boundary grid. Grids inside the boundaries are regenerated, using linear interpolation, along the grid line normal to the ship surface with distance factors. For small deformations, the outer boundary does not need to be deformed, while the inner meshes are moved in the same manner as for large deformations.

1.3 Outline

This thesis is divided into five chapters. The second chapter discusses mathematical modeling and numerical methods for the fluid solver, the structure solver, and fluid–structure coupling. Chapter 3 discusses nonlinear responses of ship motions and structural loads on a containership in regular waves. Rigid body, one-way coupling, and two-way coupling numerical methods for structural loads are compared. Chapter 4 focuses on the structural responses of elastic bars with large deformations. The elastic bars hanging on the top or standing on the bottom of a sloshing tank, are deformed by waves and fluid movements. Chapters 3 and 4 are self-contained and divided into subsections with introduction, solution strategy, simulation design, results and discussion, and conclusions. Finally, Chapter 5 discusses overall conclusions.

CHAPTER 2

COMPUTATIONAL METHODS

2.1 Overview

For the partitioned FSI using the ALE formulation, separate fluid and structure solvers are necessary. An interaction algorithm for fluid–structure domain interfaces and a numerical method for dynamic movement of the fluid grid surrounding a ship are also required.

For this thesis a FDM-based CFD code, CFDShip-Iowa version 4 (Carrica et al., 2007a), was used as the fluid solver. CFDShip-Iowa is a general-purpose URANS/DES overset solver. It uses a blended $k-\omega/k-\varepsilon$ model for turbulence; a single-phase level set approach to model the free surface; and dynamic overset grids to resolve large-amplitude motions (Carrica et al., 2007b). Full, six degrees of freedom (6-DOF), rigid-body motion computations with moving control surfaces and resolved or modeled propulsors are accommodated. Capabilities include the incorporation of incoming regular and irregular waves, autopilot, and maneuvering controllers (Carrica et al., 2008). CFDShip-Iowa has been validated against a variety of steady-state and dynamic problems (Carrica et al., 2007a and 2007b; Sakamoto et al., 2008).

The structure solver can be a linear or nonlinear solver as best serves the solution of the problem. The linear solver suits problems with small deformations, while the nonlinear solver is appropriate for problems with large deformations. The modal superposition is applied for the linear solver in this thesis. The modal superposition is performed in CFDShip-Iowa using the natural frequencies and mode shapes obtained through commercial FEM codes such as ABAQUS and ANSYS. For large deformations,

a nonlinear structure solver based on the FEM (Bhatti, 2006) is developed. The entire nonlinear solver process is carried out in CFDShip-Iowa.

To transfer forces and deformations onto non-matching grids for fluid and structure domains, the gluing method proposed by Maman and Farhat (1995) and Farhat et al. (1998a) is applied. The fluid grid is deformed using a linear elastic solver for the outer boundary and linear interpolation for the interior grids. The dynamic fluid grid movement and the force and deformation transfer are integrated into CFDShip-Iowa.

2.2 Mathematical Modeling of Fluid Solver

2.2.1 Governing Equations

The continuity and momentum equations in non-dimensional vectorial form for the fluid solver are written as

$$\nabla \cdot \mathbf{u} = 0 \tag{2.1}$$

$$\frac{\partial \mathbf{u}}{\partial t} + \mathbf{u} \cdot \nabla \mathbf{u} = -\nabla p + \nabla \cdot \left[\frac{1}{\mathrm{Re}_{eff}} \left(\nabla \mathbf{u} + \nabla \mathbf{u}^T \right) \right] + \mathbf{s} \tag{2.2}$$

where $\mathbf{u}$ is the fluid velocity vector and $\mathbf{s}$ is the source term. The effective Reynolds number is defined as $\mathrm{Re}_{eff} = U_0 L_{PP} / (\nu + \nu_t)$ with the turbulent eddy viscosity ν_t. The dimensionless piezometric pressure is defined as $p = p_{abs} / \rho U_0^2 + z / Fr^2 + 2k/3$, where p_{abs} is the absolute pressure. The Froude number is $Fr = U_0 / \sqrt{g L_{PP}}$. The turbulent kinetic energy is $k = \frac{1}{2}\left(\overline{u'^2} + \overline{v'^2} + \overline{w'^2} \right)$, and u', v', w' denote the velocity fluctuations in the three Cartesian coordinate directions. U_0 and L_{PP} are the reference velocity and length, usually the ship's forward speed and length, respectively.

2.2.2 Free Surface Modeling

The density and viscosity of air are assumed to be negligible, implying that no pressurized air/water interface can exist, resulting in a single-phase problem. Surface tension effects are small and also considered negligible. The free surface is modeled with a level set approach. Transport of the level set function with no mass transfer on the interface is rendered as

$$\frac{\partial \phi}{\partial t} + \mathbf{u} \cdot \nabla \phi = 0 \tag{2.3}$$

where ϕ is the distance function, positive in water. Eq. (2.3) automatically satisfies kinematic free surface boundary conditions, but dynamic free surface boundary conditions (DFSBC) need to be derived from jump conditions at the air/water interface. These result in the following requirements for velocity and pressure:

$$\mathbf{n} \cdot \nabla \mathbf{u}\big|_{\text{int}} = 0 \tag{2.4}$$

$$p_{\text{int}} = \frac{z_{\text{int}}}{Fr^2} \tag{2.5}$$

where **n** is the normal vector from the free surface into air. Subscript 'int' indicates quantities at the interface. To satisfy the DFSBC Eq. (2.4) is solved in air and Eq. (2.5) is enforced on the interface, simultaneously solving Eqs. (2.1) and (2.2) in water to obtain a velocity field that satisfies the mass and momentum conservation equations and the free surface boundary conditions at the interface.

Since the interface is embedded in the grid, the free surface does not generally lay on grid points. Therefore, it is necessary to define an artificial pressure on points in air so that the interface pressure will satisfy Eq. (2.5). Linear interpolation yields a pressure condition on the neighbor point:

$$p_{na} = \frac{p_{\text{int}}}{\eta} - p_p \frac{1-\eta}{\eta} \tag{2.6}$$

where $\eta = \phi_p / (\phi_p - \phi_{na})$ is the distance fraction from the local point to the interface. Subscript 'p' stands for the point in water to be computed and 'na' for any neighbor in air. Equation (2.6) is used in the pressure Poisson equation for any neighbor in air to implicitly enforce the DFSBC for pressure. Details this process is found in Carrica et al. (2007a).

The level set function should remain the distance function throughout whole computation since the free surface normal, obtained from $\mathbf{n} = \nabla\phi$, is required for advection and the distance function is used to detect interface location. The nearest neighbors to the free surface are reinitialized geometrically. The remaining domain is reinitialized using an implicit transport of the level set function with the normal:

$$\mathbf{n} \cdot \nabla\phi = sign(\phi_0) \tag{2.7}$$

where ϕ_0 is the non-reinitialized level set function. Since the normal, $\mathbf{n}$, into the fluid to be reinitialized is a function of ϕ, Eq. (2.7) is nonlinear. Dirichlet boundary conditions for Eq. (2.7) are the geometrically reinitialized close points.

2.2.3 Turbulence Modeling

The turbulence model used is a blended $k-\omega/k-\varepsilon$ model. The $k-\omega$ model has proven to be robust, accurate, and applicable to complex geometries and flows. The transport equations for the $k-\omega$ model are

$$\begin{aligned} &\frac{\partial k}{\partial t} + (\mathbf{u} - \sigma_k \nabla \nu_t) \cdot \nabla k - \frac{1}{P_k} \nabla^2 k + s_k = 0 \\ &\frac{\partial \omega}{\partial t} + (\mathbf{u} - \sigma_\omega \nabla \nu_t) \cdot \nabla \omega - \frac{1}{P_\omega} \nabla^2 \omega + s_\omega = 0 \end{aligned} \tag{2.8}$$

where k is the turbulent kinetic energy and ω is the specific dissipation rate. The turbulent viscosity and the effective Peclet numbers are defined as

$$\nu_t = \frac{k}{\omega},\ P_k = \frac{1}{1/\mathrm{Re} + \sigma_k \nu_t},\ P_\omega = \frac{1}{1/\mathrm{Re} + \sigma_\omega \nu_t}. \tag{2.9}$$

The source terms for k and ω are

$$\begin{aligned} s_k &= -G + \beta^* \omega k \\ s_\omega &= -\gamma \frac{\omega}{k} G + \beta \omega^2 - 2(1 - F_1)\sigma_{\omega 2} \frac{1}{\omega} \nabla k \cdot \nabla \omega \end{aligned} \tag{2.10}$$

where

$$G = \nu_t \tau : \nabla \mathbf{u}$$

$$F_1 = \tanh\left[\left(\min\left(\max\left(\frac{\sqrt{k}}{0.09\omega\delta}; \frac{1}{\mathrm{Re}}\frac{500}{\delta^2\omega}\right); \frac{4\sigma_{\omega 2} k}{CD_{k\omega}\delta^2}\right)\right)^4\right]. \tag{2.11}$$

$$CD_{k\omega} = \max\left(2\sigma_{\omega 2}\frac{1}{\omega}\nabla k \cdot \nabla \omega; 10^{-20}\right)$$

The blending function F_1 is 1 in the sublayer and logarithmic regions of boundary layers. It gradually switches to zero in the wake region. This takes advantage of the strengths of the $k-\omega$ and $k-\varepsilon$ models, i.e., the $k-\omega$ model does not require near-wall damping functions and uses simple Dirichlet boundary conditions and the $k-\varepsilon$ model is less sensitive to the level of free-stream turbulence than the $k-\omega$ model. The distance to the nearest no-slip surface, δ, is required to calculate F_1. Model constants are locally weighted averages, i.e., $\varphi = F_1 \varphi_1 + (1 - F_1)\varphi_2$, where φ_1 are the standard $k-\omega$ model constants and φ_2 are the transformed $k-\varepsilon$ model constants shown in Table 2.1.

With the blended $k-\omega/k-\varepsilon$ model, a shear stress transport (SST) model is incorporated as a user specified option. The SST model accounts for principal turbulent stresses transport and improves results for flows with adverse pressure gradients. It is identical to the blended $k-\omega/k-\varepsilon$ model except for variation in σ_k (see Table 2.1) and the eddy viscosity definition as

$$\nu_t = \frac{0.31k}{\max\left(0.31\omega\,;\,\Omega F_2\right)}$$

$$F_2 = \tanh\left[\left(\max\left(\frac{2\sqrt{k}}{0.09\omega\delta}\,;\,\frac{500\nu}{\delta^2\omega}\right)\right)^2\right] \tag{2.12}$$

where Ω is the absolute value of the vorticity. This model yields better results than most other isotropic two-equation turbulence models for flows with separation (Menter, 1994).

At the free surface, zero normal gradient is generally used for both k and ω, which translates in the following conditions:

$$\nabla k\cdot\mathbf{n} = \nabla\omega\cdot\mathbf{n} = 0\,. \tag{2.13}$$

2.2.4 Rigid-Body Motion

The location and attitude of ship is computed solving rigid-body equations of motion in the ship coordinate system. The ship coordinate system is selected to align with the principal axes of inertia, resulting in a diagonal inertia tensor:

$$\begin{bmatrix} I_x & 0 & 0 \\ 0 & I_y & 0 \\ 0 & 0 & I_z \end{bmatrix} = \begin{bmatrix} m\left(r_{g,x}^2 + y_G^2 + z_G^2\right) & 0 & 0 \\ 0 & m\left(r_{g,y}^2 + z_G^2 + x_G^2\right) & 0 \\ 0 & 0 & m\left(r_{g,z}^2 + x_G^2 + y_G^2\right) \end{bmatrix} \tag{2.14}$$

where $r_{g,j}$ is the radius of gyration with respect to coordinate axis j and $x_G = x_{rot} - x_{CG}$ is the distance between the point of rotation (defined by the mount geometry or zero

gross moments of inertia) and the center of gravity. Under these conditions, the rigid-body motion equations for the ship are written as

$$\begin{aligned}
&m\left[\dot{u}-vr+wq-x_G\left(q^2+r^2\right)+y_G\left(pq-\dot{r}\right)+z_G\left(pr+\dot{q}\right)\right]=X\\
&m\left[\dot{v}-wp+ur-y_G\left(r^2+p^2\right)+z_G\left(qr-\dot{p}\right)+x_G\left(qp+\dot{r}\right)\right]=Y\\
&m\left[\dot{w}-uq+vp-z_G\left(p^2+q^2\right)+x_G\left(rp-\dot{q}\right)+y_G\left(rq+\dot{p}\right)\right]=Z\\
&I_x\dot{p}+(I_z-I_y)qr+m\left[y_G\left(\dot{w}-uq+vp\right)-z_G\left(\dot{v}-wp+ur\right)\right]=K\\
&I_y\dot{q}+(I_x-I_z)rp+m\left[z_G\left(\dot{u}-vr+wq\right)-x_G\left(\dot{w}-uq+vp\right)\right]=M\\
&I_z\dot{r}+(I_y-I_x)pq+m\left[x_G\left(\dot{v}-wp+ur\right)-y_G\left(\dot{u}-vr+wq\right)\right]=N
\end{aligned} \tag{2.15}$$

where X, Y, Z, K, M, N are the surge, sway, and heave forces and the roll, pitch, and yaw moments. u, v, w are the linear velocities and $\dot{u}$, $\dot{v}$, $\dot{w}$ are the linear accelerations in x, y, z directions in the ship coordinate system. p, q, r and $\dot{p}$, $\dot{q}$, $\dot{r}$ are the angular velocities and accelerations around the x, y, z directions in the ship system, respectively. Dynamic equations for the rigid-body motion are solved numerically using a predictor–corrector implicit approach. This numerical scheme is explained in detail in Carrica et al. (2007b).

2.2.5 Convective Terms

The total time derivative has to be modified to account for gird velocities. The total time derivative is expressed as the ALE formulation for a generic variable φ:

$$\frac{\mathrm{D}\varphi}{\mathrm{D}t}=\frac{\partial\varphi}{\partial t}+\nabla\cdot\left[\left(\mathbf{u}-\dot{\mathbf{x}}\right)\varphi\right] \tag{2.16}$$

where $\dot{\mathbf{x}}$ is the grid velocity vector. The grid velocity is computed using a second-order backward difference approximation:

$$\dot{\mathbf{x}}^{t}_{i,j,k} = \frac{1.5\,\mathbf{x}^{t}_{i,j,k} - 2\,\mathbf{x}^{t-1}_{i,j,k} + 0.5\,\mathbf{x}^{t-2}_{i,j,k}}{\Delta t}. \tag{2.17}$$

2.3 Numerical Methods for Fluid Solver

2.3.1 Coordinate Transformation

To accommodate complex body geometries, generalized curvilinear coordinates are used. Equations are transformed from physical domain (x, y, z, t) into computational domain (ξ, η, ζ, τ). Using transformation relations, the continuity and momentum equations, Eqs. (2.1) and (2.2), in tensor form are written as

$$\frac{1}{J}\frac{\partial}{\partial \xi^{j}}\left(b_i^{j} u_i\right) = 0 \tag{2.18}$$

$$\begin{aligned}\frac{1}{J}\frac{\partial (J u_i)}{\partial \tau} + \frac{1}{J} b_j^{k}\left(u_j - \frac{\partial x_j}{\partial \tau}\right)\frac{\partial u_i}{\partial \xi^{k}} &= -\frac{1}{J} b_i^{k}\frac{\partial p}{\partial \xi^{k}} \\ &+ \frac{1}{J}\frac{\partial}{\partial \xi^{j}}\left(\frac{b_i^{j} b_i^{k}}{J\,\mathrm{Re}_{eff}}\frac{\partial u_i}{\partial \xi^{k}}\right) + \frac{b_j^{k}}{J}\frac{\partial \nu_t}{\partial \xi^{k}}\frac{b_i^{l}}{J}\frac{\partial u_j}{\partial \xi^{l}} + s_i\end{aligned} \tag{2.19}$$

where u_i, J, and b_j^{k} are the velocity components, the Jacobian, and the matrices of the transformation, respectively. A new convective term related to the grid velocity for moving or deforming grids is added to the convective term of Eq. (2.19).

2.3.2 Discretization Strategy

A second-order Euler backward difference is applied to time derivatives for all variables. Convection and viscous terms of Eq. (2.2) are discretized with a second-order upwind scheme and a second-order central difference scheme, respectively. Convection terms of Eq. (2.3) are discretized with a second-order upwind scheme. Convection and viscous terms of Eq. (2.8) are computed with a first-order upwind scheme and a second-order central difference scheme, respectively.

After splitting viscous term of Eq. (2.19) into normal and cross components, applying temporal and spatial discretization, it can be written as the discretized momentum equations for any interior point:

$$a_{ijk}u_i + \sum_{nb} a_{nb}u_{i,nb} = S_i - \frac{1}{J} b_i^k \frac{\partial p}{\partial \xi^k} \tag{2.20}$$

where a_{ijk} and a_{nb} are the pivot and neighbor coefficients from the discretization scheme. The source term, S_i, contains mixed derivative terms and velocities from the previous two time steps. The continuity equation (2.18) is enforced using Eq. (2.20) resulting in the pressure Poisson equation:

$$\frac{\partial}{\partial \xi^j}\left(\frac{b_i^j b_i^k}{J a_{ijk}} \frac{\partial p}{\partial \xi^k}\right) = \frac{\partial}{\partial \xi^j} \frac{b_i^j}{a_{ijk}} \left(\sum_{nb} a_{nb}u_{i,nb} - s_i\right). \tag{2.21}$$

2.3.3 Solution Strategy

Flow field variables are solved sequentially. Subiterations converge nonlinearities in coupled equations. For the nonlinear loop, grids are moved in concert with motions from the 6-DOF predictor or corrector step. Overset information of grids is updated by SUGGAR. The turbulence equations are solved implicitly. The level set transport equation is next solved. The level set function is reinitialized in two steps. The close points are first reinitialized geometrically, and then all the other points are reinitialized by solving Eq. (2.7). This equation is nonlinear, so a few iterations are needed to reach convergence. The pressure implicit split operator (PISO) algorithm (Issa, 1986), consisting of predictor and corrector steps, is finally used to calculate the pressure. A flowchart for the solution strategy is shown in Fig. 2.1. To be coupled with the structure solver, the fluid solver receives displacements from the structure solver before moving or deforming grid, and it sends forces to the structure solver after computing fluid forces.

Parallel implementation in CFDShip-Iowa is accomplished through a MPI-based domain decomposition approach. An information exchange is required between blocks at the block-to-block interface, and it is necessary between donor and interpolating blocks for overset grid implementations. For equations other than the pressure equation, overset interpolation information is exchanged between processors during alternating direction implicit (ADI) iterations. The pressure equation is built into a sparse pressure matrix and solved with the PETSc toolkit (Balay et al., 2002).

2.4 Numerical Methods for Structure Solver

2.4.1 Linear Solver for Small Deformation

For problems with small deformations, the modal superposition transient analysis predicts the ship elastic responses. Coupling fluid and structure solvers can be performed with either a one-way or two-way approach. The structural model responds to the fluid forces in either method. In one-way coupling, the fluid solver does not receive structural response information. In two-way coupling, the ship surface of fluid grid is deformed in concert with structural responses.

In one-way coupling modal analysis must account for effects of added-mass forces due to elastic degrees of freedom. For surface vessels, the added-mass of the water must be considered due to elastic vibrations. This is especially important when slamming occurs (Faltinsen, 2000; Greco et al., 2004). Water presence is incorporated into the finite element model using acoustic fluid elements. Results of the modal analysis are thus 'wet' modes. Assuming the fluid is compressible and inviscid, the equilibrium equation is

$$\nabla p + \gamma \dot{\mathbf{v}} + \rho_f \ddot{\mathbf{v}} = 0 \tag{2.22}$$

where p is the dynamic pressure in the fluid; ρ_f is the density of the fluid; γ is the volumetric constant for dissipation effects; and $\dot{\mathbf{v}}$ and $\ddot{\mathbf{v}}$ are the fluid particle velocity

and acceleration, respectively. Dynamic pressure relates the bulk modulus of fluid K_f with the volumetric strain:

$$p = -K_f \nabla \cdot \mathbf{v} . \tag{2.23}$$

The equation of motion for the fluid in terms of fluid pressure is derived from Eqs. (2.22) and (2.23):

$$\frac{1}{K_f}\ddot{p} + \frac{\gamma}{\rho_f K_f}\dot{p} - \frac{1}{\rho_f}\nabla^2 p = 0 . \tag{2.24}$$

Discretized finite element equations resulting from Eq. (2.24) can be written as

$$\mathbf{M_f}\ddot{\mathbf{p}} + \mathbf{C_f}\dot{\mathbf{p}} + \mathbf{K_f}\mathbf{p} - \mathbf{S_{fs}}\ddot{\mathbf{d}} = \mathbf{0} \tag{2.25}$$

where $\mathbf{p}$ is the fluid node pressure vector and $\mathbf{d}$ is the displacement vector on a fluid–structure interface. $\mathbf{S_{fs}}$ is the coupling matrix, representing the effective surface area associated with each interface node. By virtue of fluid pressure at the interface, the structural equation of motion is written as

$$\mathbf{M_s}\ddot{\mathbf{d}} + \mathbf{C_s}\dot{\mathbf{d}} + \mathbf{K_s}\mathbf{d} + \mathbf{S}_{\mathbf{fs}}^T\mathbf{p} = \mathbf{F_s} . \tag{2.26}$$

From Eqs. (2.25) and (2.26), the complete finite element equations for the FSI problem are described as

$$\begin{bmatrix} \mathbf{M_s} & \mathbf{0} \\ -\mathbf{S_{fs}} & \mathbf{M_f} \end{bmatrix}\begin{Bmatrix} \ddot{\mathbf{d}} \\ \ddot{\mathbf{p}} \end{Bmatrix} + \begin{bmatrix} \mathbf{C_s} & \mathbf{0} \\ \mathbf{0} & \mathbf{C_f} \end{bmatrix}\begin{Bmatrix} \dot{\mathbf{d}} \\ \dot{\mathbf{p}} \end{Bmatrix} + \begin{bmatrix} \mathbf{K_s} & \mathbf{S}_{\mathbf{fs}}^T \\ \mathbf{0} & \mathbf{K_f} \end{bmatrix}\begin{Bmatrix} \mathbf{d} \\ \mathbf{p} \end{Bmatrix} = \begin{Bmatrix} \mathbf{F_s} \\ \mathbf{0} \end{Bmatrix} . \tag{2.27}$$

Introducing an auxiliary variable, $\boldsymbol{\psi} = \mathbf{p}/\omega^2$, the non-symmetric eigenvalue problem from Eq. (2.27) yields a symmetric eigenvalue problem as

$$\left(\begin{bmatrix} \mathbf{K}_s & \mathbf{S}_{fs}^T & \mathbf{0} \\ \mathbf{S}_{fs} & -\mathbf{M}_f & \mathbf{K}_f \\ \mathbf{0} & \mathbf{K}_f^T & \mathbf{0} \end{bmatrix} - \omega^2 \begin{bmatrix} \mathbf{M}_s & \mathbf{0} & \mathbf{0} \\ \mathbf{0} & \mathbf{0} & \mathbf{0} \\ \mathbf{0} & \mathbf{0} & \mathbf{K}_f \end{bmatrix} \right) \begin{Bmatrix} \mathbf{d} \\ \mathbf{p} \\ \boldsymbol{\psi} \end{Bmatrix} = \begin{Bmatrix} \mathbf{0} \\ \mathbf{0} \\ \mathbf{0} \end{Bmatrix} \tag{2.28}$$

where ω is the eigenvalue. This equation can be solved using Lanczos method.

Because forces on the structure due to fluid–structure interaction, $\mathbf{S}_{fs}^T\mathbf{p}$, are very small compared to other structural forces, this term is negligible for structural analysis. Equation (2.26) can be simplified as

$$\mathbf{M}_s\ddot{\mathbf{d}} + \mathbf{C}_s\dot{\mathbf{d}} + \mathbf{K}_s\mathbf{d} = \mathbf{F}_s \tag{2.29}$$

where $\mathbf{F}_s$ is the fluid force vector obtained from the CFD solver. Defining the displacement vector as

$$\mathbf{d} = \sum_{i=1}^{n} \boldsymbol{\varphi}_i z_i \tag{2.30}$$

and introducing mass and stiffness orthogonality properties of mode shapes, Eq. (2.29) becomes a set of decoupled modal equations:

$$\ddot{z}_i + 2\omega_i\xi_i\dot{z}_i + \omega_i^2 z = f_i \tag{2.31}$$

where for the i th mode $\boldsymbol{\varphi}_i$, ω_i, ξ_i, and z_i are the mode shape vector, the natural frequency, the damping ratio, and the modal coordinate, respectively. The right hand side of the equation incorporates fluid forces due to rigid-body motion, $f_i = \boldsymbol{\varphi}_i^T\mathbf{F}_s$. General Newmark's method (Newmark, 1959) is applied for time integration of Eq. (2.31).

In two-way coupling, the CFD solver explicitly accounts for added-mass forces due to flexure. In this case the structural model need not include acoustic fluid elements. The modal analysis result is 'dry' modal representation. Natural frequencies and mode shapes for the dry mode are obtained from Eq. (2.29). Dry mode natural frequencies provided are different from natural frequencies in water since elastic displacement effects,

and resulting pressure and viscous forces are accounted for explicitly by the CFD solver. This yields additional damping by energy transfer from the elastic structure to the fluid, absent in the one-way coupled approach. Acoustical representation of water in the one-way coupling does allow for energy dissipation due to acoustic waves radiation in a compressible medium.

2.4.2 Nonlinear Solver for Large Deformation

The structural behavior is governed by the conservation of momentum:

$$\rho_s \ddot{\mathbf{d}} = \nabla \cdot \boldsymbol{\sigma} + \mathbf{s} \tag{2.32}$$

where $\ddot{\mathbf{d}}$ is the deformation acceleration, and $\boldsymbol{\sigma}$ and $\mathbf{s}$ are the Cauchy's stress tensor and the body forces on the structure, respectively. ρ_s denotes the density of the structure material. According to the magnitude of the displacements and rotations, Eq. (2.32) can be analyzed either as linear or nonlinear. A linear relationship between strains and displacements can be applied only to small displacements and rotations. In the presence of large deformations there can be significant changes in the configuration. In such case the relationship between strains and displacements cannot be treated as linear.

The equivalent weak form, derived from Eq. (2.32), for geometric nonlinearity is expressed as

$$\iiint_{V^0} \rho_s \delta\mathbf{d}^T \ddot{\mathbf{d}}\, dV^0 + \iiint_{V^0} \hat{\mathbf{S}} : \delta\hat{\boldsymbol{\varepsilon}}\, dV^0 = \iint_{A^0} \delta\mathbf{d}^T \mathbf{q}^0\, dA^0 + \iiint_{V^0} \delta\mathbf{d}^T \mathbf{b}^0\, dV^0 \tag{2.33}$$

where $\hat{\mathbf{S}}$ is the second Piola–Kirchhoff stress tensor and $\hat{\boldsymbol{\varepsilon}}$ is the Green–Lagrange strain tensor. The virtual displacement vector is defined as $\delta\mathbf{d} = \{\delta u, \delta v, \delta w\}^T$. The applied surface and body force vectors are denoted as $\mathbf{q}$ and $\mathbf{b}$, respectively. Superscript 0 describes force vectors, area, and volume in the initial configuration.

Equation (2.33) is nonlinear in terms of displacements, and must be linearized to element tangent equations. Introducing a directional derivative notation, Eq. (2.33) is linearized for finite element formulation with matrix-vector notation as follows:

$$\begin{aligned}&\iiint_{V^0}\rho_s\delta\mathbf{d}^T\ddot{\mathbf{d}}\,dV^0+\iiint_{V^0}\left[\delta\mathbf{H}^T\overline{\mathbf{S}}\Delta\mathbf{H}+\delta\mathbf{H}^T\overline{\mathbf{F}}^T\mathbf{C}\overline{\mathbf{F}}\Delta\mathbf{H}\right]dV^0\\&\quad=-\iiint_{V^0}\delta\mathbf{H}^T\overline{\mathbf{F}}^T\mathbf{S}\,dV^0+\iint_{A^0}\delta\mathbf{d}^T\mathbf{q}^0\,dA^0+\iiint_{V^0}\delta\mathbf{d}^T\mathbf{b}^0\,dV^0\end{aligned}\tag{2.34}$$

where $\mathbf{H}$ is the displacement gradient in vector form and $\overline{\mathbf{S}}$ is a 9×9 matrix composed of the second Piola–Kirchhoff stress tensor:

$$\mathbf{H}=\left\{\frac{\partial u}{\partial x^0},\frac{\partial u}{\partial y^0},\frac{\partial u}{\partial z^0},\frac{\partial v}{\partial x^0},\frac{\partial v}{\partial y^0},\frac{\partial v}{\partial z^0},\frac{\partial w}{\partial x^0},\frac{\partial w}{\partial y^0},\frac{\partial w}{\partial z^0}\right\}^T\tag{2.35}$$

$$\overline{\mathbf{S}}=\begin{bmatrix}S_{xx}&S_{xy}&S_{zx}&0&0&0&0&0&0\\S_{xy}&S_{yy}&S_{yz}&0&0&0&0&0&0\\S_{zx}&S_{yz}&S_{zz}&0&0&0&0&0&0\\0&0&0&S_{xx}&S_{xy}&S_{zx}&0&0&0\\0&0&0&S_{xy}&S_{yy}&S_{yz}&0&0&0\\0&0&0&S_{zx}&S_{yz}&S_{zz}&0&0&0\\0&0&0&0&0&0&S_{xx}&S_{xy}&S_{zx}\\0&0&0&0&0&0&S_{xy}&S_{yy}&S_{yz}\\0&0&0&0&0&0&S_{zx}&S_{yz}&S_{zz}\end{bmatrix}.\tag{2.36}$$

For compressible neo-Hookean material, the 6×6 constitutive matrix $\mathbf{C}$ is determined from the strain energy density function with respect to the right Cauchy–Green tensor:

$$C_{ijkl}=\lambda c_{ij}^{-1}c_{kl}^{-1}+\left(\mu-\lambda\ln\left(\det\mathbf{F}\right)\right)\left(c_{ik}^{-1}c_{jl}^{-1}+c_{il}^{-1}c_{kj}^{-1}\right);\qquad i,\,j,\,k,\,l=1,\,2,\,3\tag{2.37}$$

$$\mathbf{C}=\begin{bmatrix} C_{1111} & C_{1122} & C_{1133} & \frac{1}{2}\left(C_{1112}+C_{1121}\right) & \frac{1}{2}\left(C_{1123}+C_{1132}\right) & \frac{1}{2}\left(C_{1113}+C_{1131}\right) \\ C_{2211} & C_{2222} & C_{2233} & \frac{1}{2}\left(C_{2212}+C_{2221}\right) & \frac{1}{2}\left(C_{2223}+C_{2232}\right) & \frac{1}{2}\left(C_{2213}+C_{2231}\right) \\ C_{3311} & C_{3322} & C_{3333} & \frac{1}{2}\left(C_{3312}+C_{3321}\right) & \frac{1}{2}\left(C_{3323}+C_{3332}\right) & \frac{1}{2}\left(C_{3313}+C_{3331}\right) \\ C_{1211} & C_{1222} & C_{1233} & \frac{1}{2}\left(C_{1212}+C_{1221}\right) & \frac{1}{2}\left(C_{1223}+C_{1232}\right) & \frac{1}{2}\left(C_{1213}+C_{1231}\right) \\ C_{2311} & C_{2322} & C_{2333} & \frac{1}{2}\left(C_{2312}+C_{2321}\right) & \frac{1}{2}\left(C_{2323}+C_{2332}\right) & \frac{1}{2}\left(C_{2313}+C_{2331}\right) \\ C_{3111} & C_{3122} & C_{3133} & \frac{1}{2}\left(C_{3112}+C_{3121}\right) & \frac{1}{2}\left(C_{3123}+C_{3132}\right) & \frac{1}{2}\left(C_{3113}+C_{3131}\right) \end{bmatrix} \tag{2.38}$$

where λ and μ are Lamé's constants, and c_{ij}^{-1} is the ij th component of the inverse matrix of the right Cauchy–Green tensor $\mathbf{c}=\mathbf{F}^T\mathbf{F}$. $\mathbf{F}$ is the deformation gradient defined as

$$\mathbf{F}=\begin{bmatrix} \frac{\partial x}{\partial x^0} & \frac{\partial x}{\partial y^0} & \frac{\partial x}{\partial z^0} \\ \frac{\partial y}{\partial x^0} & \frac{\partial y}{\partial y^0} & \frac{\partial y}{\partial z^0} \\ \frac{\partial z}{\partial x^0} & \frac{\partial z}{\partial y^0} & \frac{\partial z}{\partial z^0} \end{bmatrix}. \tag{2.39}$$

Using the relational equations $\Delta\mathbf{d}=\mathbf{N}^T\Delta\boldsymbol{\delta}$ and $\Delta\mathbf{H}=\mathbf{B}^T\Delta\boldsymbol{\delta}$, where $\Delta\mathbf{d}$ is the nodal displacement vector; $\mathbf{N}$ is the interpolation function matrix; and $\Delta\boldsymbol{\delta}$ is the displacement increment vector, Eq. (2.34), known as the tangent element equations, is expressed as follows:

$$\mathbf{M_S}\ddot{\mathbf{d}}+\left(\mathbf{K_C}+\mathbf{K_G}\right)\Delta\boldsymbol{\delta}=\mathbf{R_I}+\mathbf{F_S} \tag{2.40}$$

where $\mathbf{K_C}$ is the current stiffness matrix; $\mathbf{K_G}$ is the geometric (or stress) stiffness matrix; $\mathbf{R_I}$ is the equivalent nodal load vector due to stresses in the currently known configuration; and $\mathbf{F_S}$ is the equivalent nodal load vector due to surface and body forces. These matrices are defined as

$$\mathbf{M_S} = \iiint_{V^0} \rho_s \mathbf{N}\mathbf{N}^T \, dV^0$$

$$\mathbf{K_C} = \iiint_{V^0} \mathbf{B}\overline{\mathbf{F}}^T \mathbf{C}\overline{\mathbf{F}}\mathbf{B}^T \, dV^0$$

$$\mathbf{K_G} = \iiint_{V^0} \mathbf{B}\overline{\mathbf{S}}\mathbf{B}^T \, dV^0 \quad . \tag{2.41}$$

$$\mathbf{R_I} = -\iiint_{V^0} \mathbf{B}\overline{\mathbf{F}}^T \mathbf{S} \, dV^0$$

$$\mathbf{F_S} = \iint_{A^0} \mathbf{N}\mathbf{q}^0 \, dA^0 + \iiint_{V^0} \mathbf{N}\mathbf{b}^0 \, dV^0$$

The second Piola–Kirchhoff stress vector, $\mathbf{S}$, is obtained from this relation:

$$\hat{\mathbf{S}} = \lambda(\ln(\det \mathbf{F}))\mathbf{c}^{-1} + \mu(\mathbf{I} - \mathbf{c}^{-1}). \tag{2.42}$$

Derivation for linearization of the weak form is described in detail in Bhatti (2006).

The equations of motion for transient solution, including damping matrix $\mathbf{C_S}$, are described at time $t^{i+1} = t^i + \Delta t$ from Eq. (2.40):

$$\mathbf{M_S}\ddot{\mathbf{d}}^{i+1} + \mathbf{C_S}\dot{\mathbf{d}}^{i+1} + \left(\mathbf{K_C}^{i+1} + \mathbf{K_G}^{i+1}\right)\Delta\boldsymbol{\delta}^{i+1} = \mathbf{R_I}^{i+1} + \mathbf{F_S}^{i+1}. \tag{2.43}$$

where the damping matrix is defined as $\mathbf{C_S} = \alpha_1 \mathbf{M_S} + \alpha_2 (\mathbf{K_C} + \mathbf{K_G})$. α_1 and α_2 are the Rayleigh damping coefficients for mass and stiffness, respectively. Using the displacement increment vector and the displacement increment vector in the nonlinear subiteration at t^{i+1}, $\boldsymbol{\delta}^{i+1}$ and $\Delta\boldsymbol{\delta}^{i+1}$, the displacements, velocities, and accelerations for general Newmark's expressions are described as follows:

$$\Delta\mathbf{d}^i = \boldsymbol{\delta}^{i+1} + \Delta\boldsymbol{\delta}^{i+1} \tag{2.44}$$

$$\mathbf{d}^{i+1} = \mathbf{d}^i + \Delta\mathbf{d}^{i+1} \tag{2.45}$$

$$\dot{\mathbf{d}}^{i+1} = \dot{\mathbf{d}}^{i} + \frac{\gamma}{\beta \Delta t}\Delta \mathbf{d}^{i} - \frac{\gamma}{\beta}\dot{\mathbf{d}}^{i} + \Delta t\left(1 - \frac{\gamma}{2\beta}\right)\ddot{\mathbf{d}}^{i} \tag{2.46}$$

$$\ddot{\mathbf{d}}^{i+1} = \ddot{\mathbf{d}}^{i} + \frac{1}{\beta \Delta t^{2}}\Delta \mathbf{d}^{i} - \frac{1}{\beta \Delta t}\dot{\mathbf{d}}^{i} - \frac{1}{2\beta}\ddot{\mathbf{d}}^{i}. \tag{2.47}$$

Substituting Eqs. (2.44) to (2.47) into Eq. (2.43), the equations of motion can be simplified as

$$\hat{\mathbf{K}}\,\Delta \boldsymbol{\delta}^{i+1} = \hat{\mathbf{F}} \tag{2.48}$$

where

$$\hat{\mathbf{K}} = \frac{1}{\beta \Delta t^{2}}\mathbf{M}_{\mathrm{S}} + \frac{\gamma}{\beta \Delta t}\mathbf{C}_{\mathrm{S}} + \mathbf{K}_{\mathrm{C}}^{i+1} + \mathbf{K}_{\mathrm{S}}^{i+1} \tag{2.49}$$

$$\begin{aligned}\hat{\mathbf{F}} = \mathbf{R}_{\mathrm{I}}^{i+1} + \mathbf{F}_{\mathrm{S}}^{i+1} - \left(\frac{1}{\beta \Delta t^{2}}\mathbf{M}_{\mathrm{S}} + \frac{\gamma}{\beta \Delta t}\mathbf{C}_{\mathrm{S}}\right)\boldsymbol{\delta}^{i+1} + \left(\frac{1}{\beta \Delta t}\mathbf{M}_{\mathrm{S}} + \left(\frac{\gamma}{\beta} - 1\right)\mathbf{C}_{\mathrm{S}}\right)\dot{\mathbf{d}}^{i} \\ + \left(\left(\frac{1}{2\beta} - 1\right)\mathbf{M}_{\mathrm{S}} + \Delta t\left(\frac{\gamma}{2\beta} - 1\right)\mathbf{C}_{\mathrm{S}}\right)\ddot{\mathbf{d}}^{i}\end{aligned}. \tag{2.50}$$

The parameters, β and γ, are selected according to the assumed variation of acceleration over the time step. For each nonlinear subiteration, the stiffness matrix and force vectors in the tangent element equations, Eq. (2.48), are updated until the displacement increment vector, $\Delta \boldsymbol{\delta}^{i+1}$, converges.

While the nodal velocity vector at t^{i+1} is obtained from Eq. (2.46), the nodal acceleration vector can be calculated to reduce the numerical error, remained in the subiteration, with the assumption of $\Delta \boldsymbol{\delta}^{i+1} = 0$ as

$$\mathbf{M}_{\mathrm{S}}\ddot{\mathbf{d}}^{i+1} = \mathbf{R}_{\mathrm{I}}^{i+1} + \mathbf{F}_{\mathrm{S}}^{i+1} - \mathbf{C}_{\mathrm{S}}\dot{\mathbf{d}}^{i+1}. \tag{2.51}$$

2.4.3 Solution Strategy

The structure solver is effective whether deformations in the problem are small or large. For small deformation problems, the modal superposition is used in CFDShip-Iowa. Mode shapes and natural frequencies should be obtained externally, using commercial codes such as ABAQUS and ANSYS. The nonlinear structure solver is useful for problems with large deformation.

The subiteration in the nonlinear structure solver is repeated until structure displacements converge. The structure solver for linear or nonlinear problem is iterated at each time-step until fluid variables converge. The structure solver process is illustrated in Fig. 2.2.

2.5 Interaction of Fluid and Structure Solvers

2.5.1 Interface of Fluid and Structure Grids

To achieve FSI time integration, suitable conditions must be prescribed along fluid–structure interfaces to permit relative sliding of the fluid and solid. Fluid nodes must remain contiguous to structural nodes, so that all nodes on the sliding interface maintain permanently aligned (Donea et al., 1982). It is necessary to transfer fluid forces to appropriate nodal forces on the structure grid and to project structural deformations onto the fluid grid, since the fluid and structure grids on the ship surface generally do not match. The present case, requiring different grid densities for the fluid and structure solvers, is very common. Geometric disparities between the grids demand a careful strategy to transfer force and displacement data back and forth accurately and stably. The gluing method, proposed by Maman and Farhat (1995) and Farhat et al. (1998a), is applied for this thesis.

Nodal forces on the structure grid are determined through Gauss integration. Nine Gauss points are used for each structure element. It is necessary to determine fluid forces for each point. In the gluing method, an associate point on a fluid element for the Gauss

point on a structure element is chosen as the nearest point on the fluid element intersected by the structure element normal including the relevant Gauss point. On the other hand, association for the fluid node deformation is determined choosing the nearest point on the structure elements as shown in Fig. 2.3. The fluid force and deformation at the associate point are interpolated using the Lagrange interpolation function for the associate element. The process of establishing the association between the grids must be performed only once prior to initiaton of the iterative solution coupling fluid and structural solvers. During the gluing process, associated element numbers and weight functions for the Lagrangian interpolation are stored for later transfer of forces and deformations. The modal superposition transient analysis for small deformations or the nonlinear elastic solver for large deformations is carried out in the structure solver using the forces provided by the fluid solver. The structure solver then projects the structure grid displacements onto the fluid grid.

2.5.2 Dynamic Deformation of Fluid Grid

Since the fluid grid may be moved due to structure deformation and motion for the ALE formulation, the fluid grid deformation should be treated carefully to maintain the initial mesh quality.

CFDShip-Iowa uses overset grids, and the fluid domain is divided into static and moving grids. The moving grids move and deform, while the static grids are fixed to the earth system and do not move. The moving grids are usually boundary layer grids surrounding ships or other objects. The boundary layer grid domains are usually near the ship surfaces. If the outer boundary of the boundary layer grid is not deformed in conjunction with the ship deformation, grid quality deteriorates or the grid becomes folded in a shrunk region, particularly in a case with large deformations.

For this thesis the boundary layer grid is assumed as a fictitious elastic structure. Like the structure grid, it is solved using the FEM. The deformation of fluid boundary

layer grid is governed by the conservation of momentum, as with the structure solver for large deformation problems:

$$\nabla \cdot \boldsymbol{\sigma} + \mathbf{s} = \mathbf{0}. \tag{2.52}$$

The weak form is derived multiplying fictitious displacements and using the Green–Gauss theorem assuming a linear relationship between strains and displacements:

$$\iiint_V \bar{\boldsymbol{\varepsilon}} \boldsymbol{\sigma} \, dV = \iint_A \bar{\mathbf{d}}^T \mathbf{q} \, dA + \iiint_V \bar{\mathbf{d}}^T \mathbf{b} \, dV. \tag{2.53}$$

The element equations are expressed as

$$\mathbf{K}_S \mathbf{d} = \mathbf{0} \tag{2.54}$$

where the force terms of right hand side are zero. The stiffness matrix, $\mathbf{K}_S$, is described as

$$\mathbf{K}_S = \iiint_V \mathbf{B}_L \mathbf{C} \mathbf{B}_L^T \, dV. \tag{2.55}$$

The strain-displacement matrix, $\mathbf{B}_L$, is different from $\mathbf{B}$ used in the nonlinear structure solver:

$$\mathbf{B}_L^T = \begin{bmatrix} \frac{\partial N_1}{\partial x} & 0 & 0 & \frac{\partial N_2}{\partial x} & 0 & 0 & \cdots \\ 0 & \frac{\partial N_1}{\partial y} & 0 & 0 & \frac{\partial N_2}{\partial y} & 0 & \cdots \\ 0 & 0 & \frac{\partial N_1}{\partial z} & 0 & 0 & \frac{\partial N_2}{\partial z} & \cdots \\ \frac{\partial N_1}{\partial y} & \frac{\partial N_1}{\partial x} & 0 & \frac{\partial N_2}{\partial y} & \frac{\partial N_2}{\partial x} & 0 & \cdots \\ 0 & \frac{\partial N_1}{\partial z} & \frac{\partial N_1}{\partial y} & 0 & \frac{\partial N_2}{\partial z} & \frac{\partial N_2}{\partial y} & \cdots \\ \frac{\partial N_1}{\partial z} & 0 & \frac{\partial N_1}{\partial x} & \frac{\partial N_2}{\partial z} & 0 & \frac{\partial N_2}{\partial x} & \cdots \end{bmatrix} \tag{2.56}$$

where $\mathbf{N}$ is the Lagrange interpolation function. The Kirchhoff material is used for the constitutive matrix $\mathbf{C}$:

$$\mathbf{C}=\frac{E}{(1+\nu)(1-2\nu)}\begin{bmatrix} 1-\nu & \nu & \nu & 0 & 0 & 0 \\ \nu & 1-\nu & \nu & 0 & 0 & 0 \\ \nu & \nu & 1-\nu & 0 & 0 & 0 \\ 0 & 0 & 0 & \frac{1-2\nu}{2} & 0 & 0 \\ 0 & 0 & 0 & 0 & \frac{1-2\nu}{2} & 0 \\ 0 & 0 & 0 & 0 & 0 & \frac{1-2\nu}{2} \end{bmatrix} \tag{2.57}$$

where E and ν are Young's modulus and Poisson's ratio, respectively.

If movement of the entire boundary layer grid is calculated using the FEM method, computational expense may exceed that for the fluid and structure solvers even though MPI is used to solve linear algebra. This thesis reduces this expense by computing only the outer boundaries of the boundary layer grid. Deformation at an arbitrary point inside the boundary layer grid is then obtained by linear interpolation along the grid line normal to the ship surface using distance factor:

$$\mathbf{d_a}=\mathbf{d_s}\frac{l_b-l_a}{l_b}+\mathbf{d_b}\frac{l_a}{l_b} \tag{2.58}$$

where $\mathbf{d}_a$, $\mathbf{d}_s$, and $\mathbf{d}_b$ are the displacement vectors at an arbitrary boundary layer grid point and points on the ship surface and the outer boundary, respectively. The girth length from the ship surface point to the arbitrary point inside the boundary layer grid and to the point on the outer boundary edge along the same grid line are respectively denoted by symbols l_a and l_b. A schematic sketch of the boundary layer grid deformation is illustrated in Fig. 2.4.

In the small deformation problems it is assumed that ship surface deformations create no outer boundary edge deformation. Interior grid movement of the boundary layer grid is obtained using Eq. (2.58) without solving Eq. (2.54) for outer boundary movement.

2.6 Overall Solution Strategy

The overall solution strategy for FSI is shown in Fig. 2.5. Previous to the first time step, the association functions of fluid–structure interface are computed. The linear interpolation function for interior grid movement of boundary layer grid is then computed. At each time step, subiterations for FSI are performed until fluid variables converge. The fluid solver supplies pressure and friction forces to associate the fluid forces to the structure grid, while the structure solver provides structure displacements to the fluid grid.

For large deformation cases, the shape of the fluid boundary layer grid can be changed extremely from its initial position. Therefore, overset information for hole cutting needs to be reinitialized at each time step. The reinitialization does not need to be performed in every subiteration for the fluid–structure interaction, since boundary layer grid deformation is very small during subiterations.

The computations related to the structure solver are peformed in a single processor, while the other tasks are executed in multiple processors based on MPI. Because the computation for the structure solver could be much more expensive than for the fluid solver, the stiffness matrix for the structure solver is built into a sparse matix and solved with the PETSc toolkit to save the cost.

Table 2.1 Blended $k-\omega/k-\varepsilon$ model constants

φ	φ_1	φ_2	$\varphi_{1,SST}$
σ_k	0.5	1.0	0.85
σ_ω	0.5	0.856	0.5
β	0.075	0.0828	0.075
β^*	0.09	0.09	0.09
γ	0.0553	0.04403	0.0553

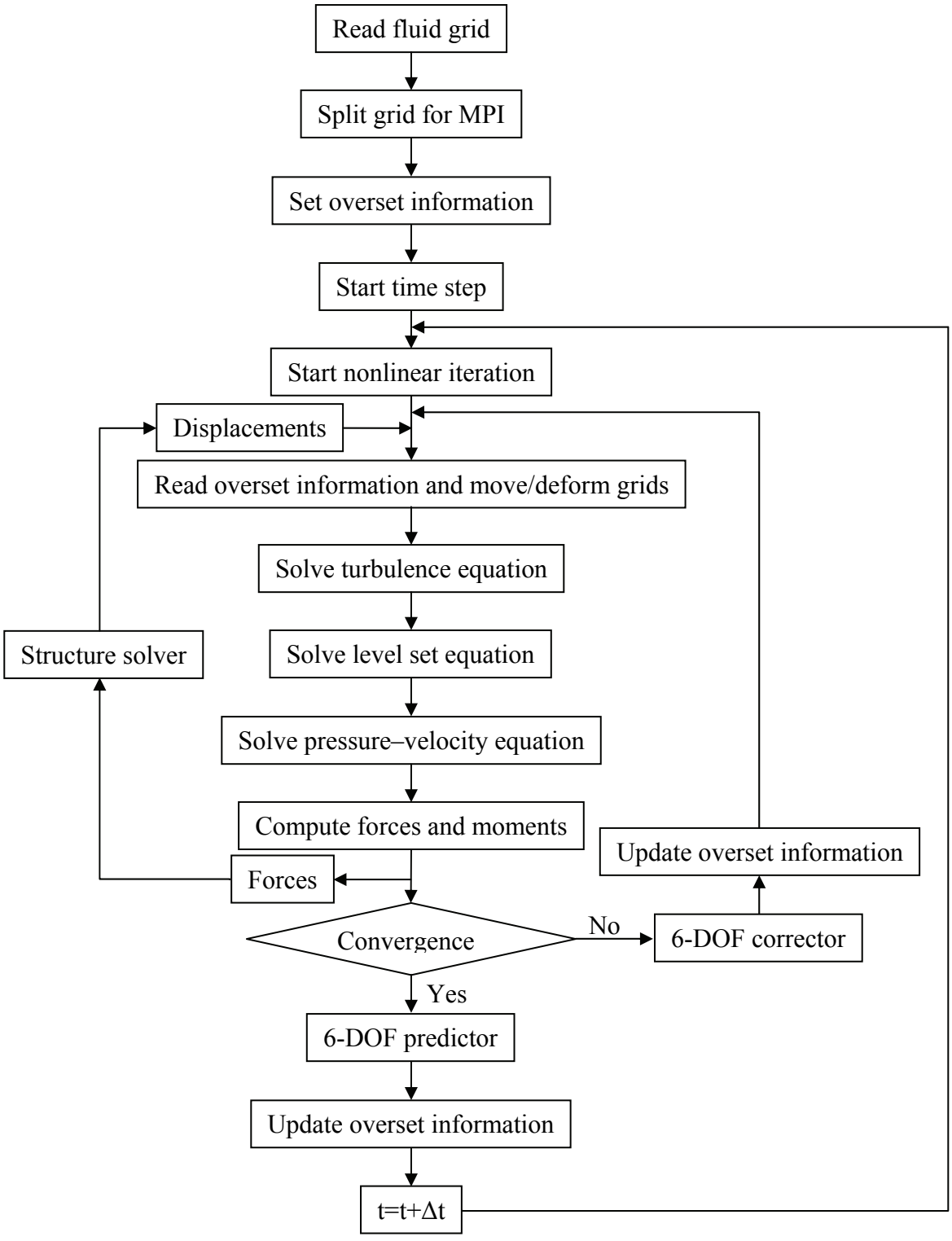

Figure 2.1 Flowchart for solution procedure of the fluid solver

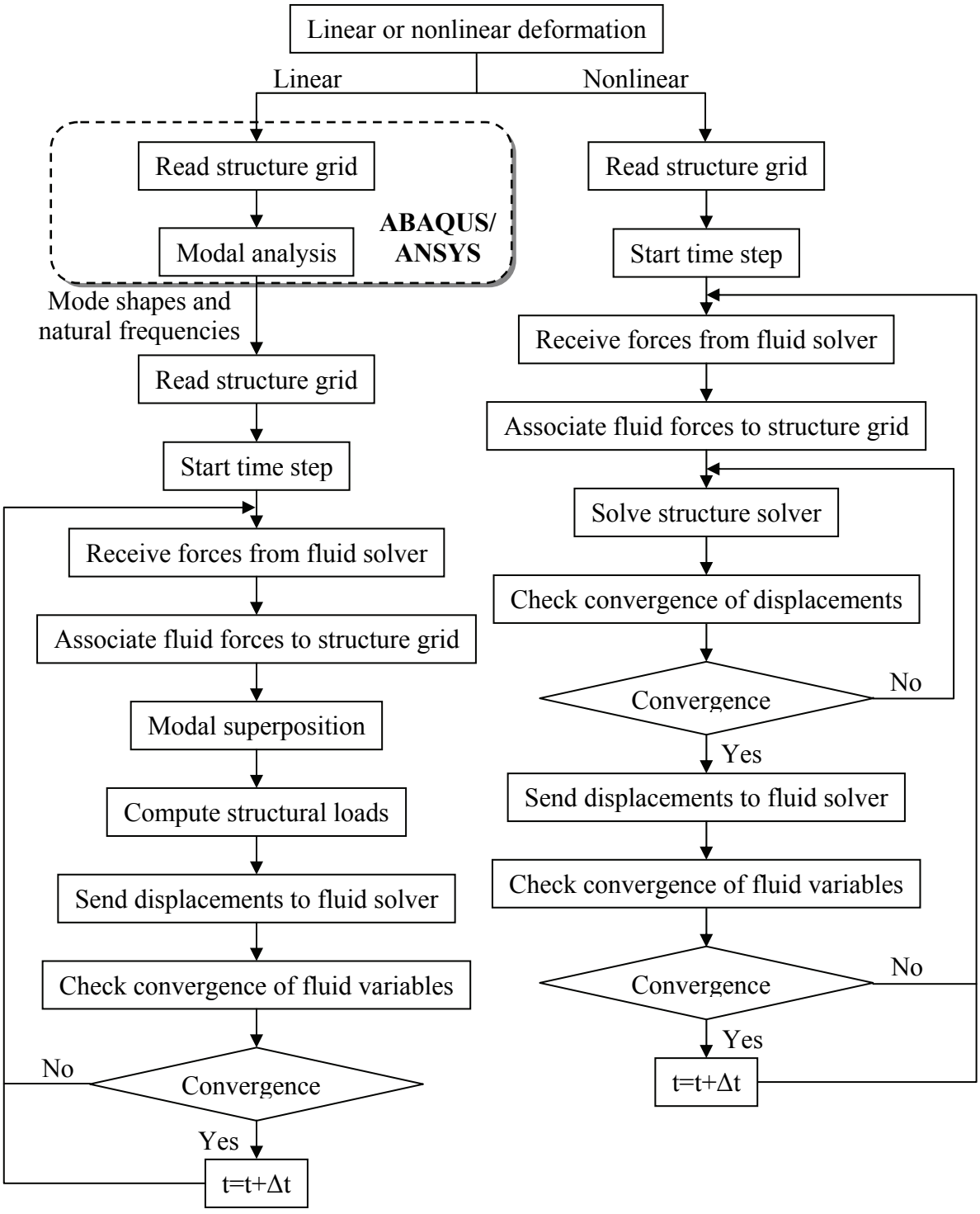

Figure 2.2 Flowchart for solution procedure of the structure solver

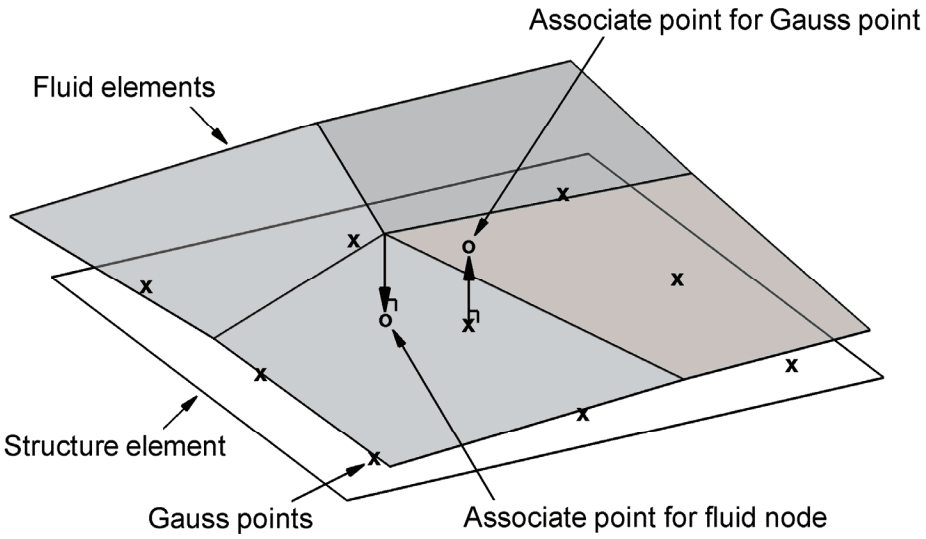

Figure 2.3 Associate points for Gauss points and fluid nodes

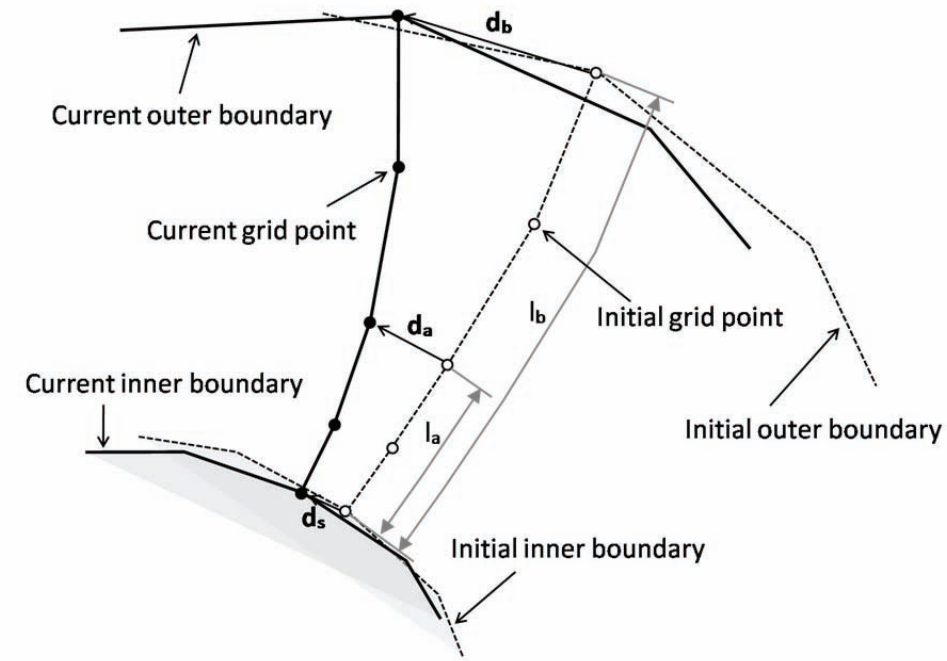

Figure 2.4 Schematic sketch of the mesh movement

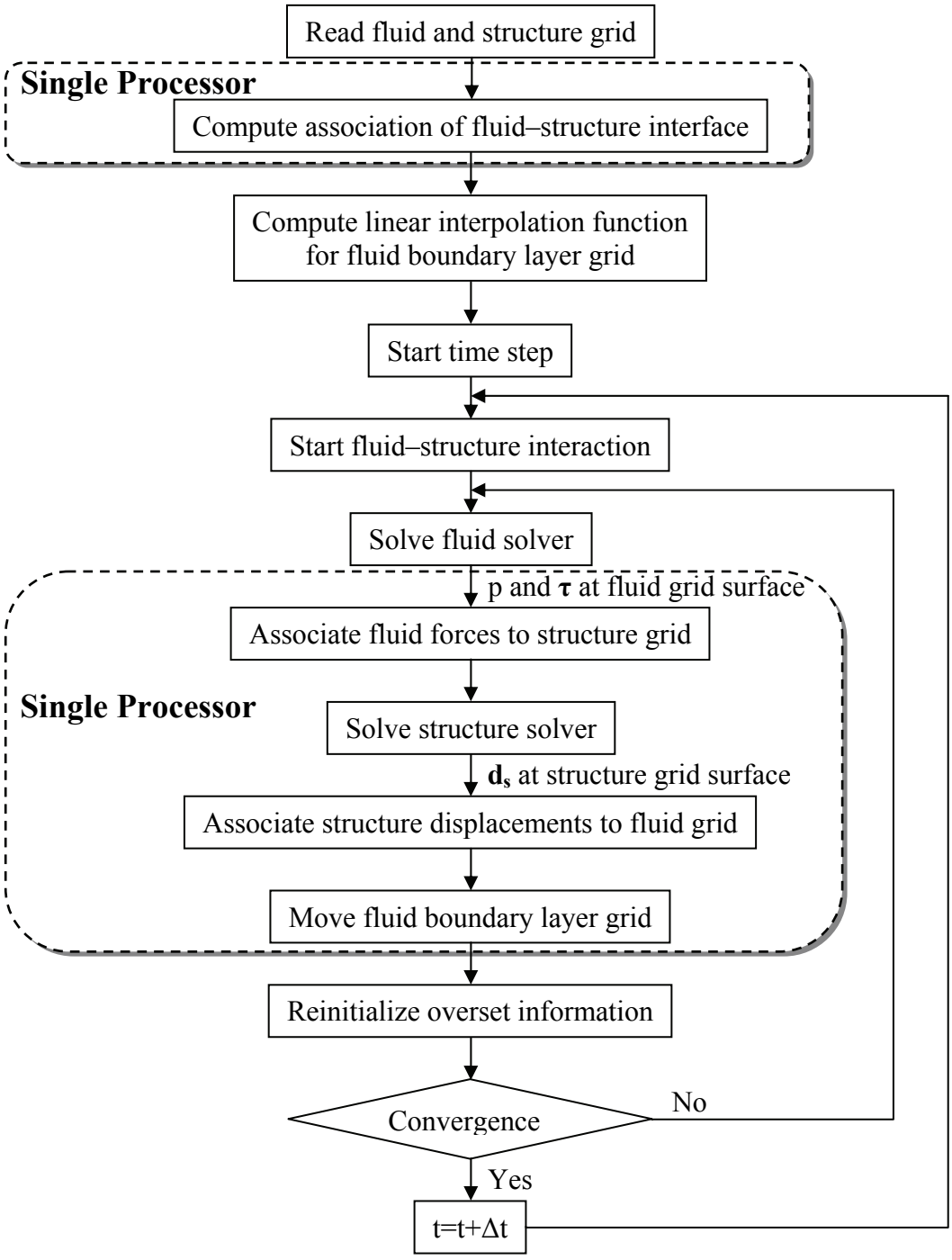

Figure 2.5 Flowchart of coupled solution procedure for FSI

CHAPTER 3
STRUCTURAL LOADS ON A CONTAINERSHIP

3.1 Introduction

Fluid–structure interactions, wave-induced loads, and hydroelastic responses are of primary importance in the structural design of a surface ship. Since nonlinear effects are significant for wave-induced structural loads, traditional approaches use nonlinear methods. These include time-domain strip theories and time-domain panel methods, to calculate unsteady structural loads (Fonseca and Guedes Soares, 1998; Fonseca and Guedes Soares, 2004a; Singh and Sen, 2007). Though useful in many cases, these methods have limited capabilities to compute complex free-surface topologies, such as very steep or overturning waves, surface piercing appendages, and water on deck. In addition, viscous effects cannot be computed from first principles.

Vertical structural loads are highly asymmetric with respect to motion cycle due to the fact that ships typically have asymmetrical vertical geometry. For example, a large bow flare can cause a sagging moment that is larger than a corresponding hogging moment. Nonlinear effects can be classified by the inverse proportion of transfer-function values to wave amplitude, the amplitude variations at the higher-order harmonic frequencies, the phase angle between the motion and forcing, and the offset of the mean values in motions and loads (Fonseca and Guedes Soares, 2002). The nonlinearity of wave response may be particularly significant in ships with small block coefficient and a large bow flare (Fonseca and Guedes Soares, 2004b).

Many researchers have focused on nonlinearities in vertical motions and wave-induced loads in recent decades through numerical simulation and physical experiment. Watanabe et al. (1989) experimented with two bow shapes of the S175 containership to

show the effects of bow flare shapes on vertical bending moment (VBM) and relative motion. They found that pitching motion and the peak value of VBM were significantly influenced by the flare shape. Nonlinear effects on the motions and loads were investigated by Fonseca and Guedes Soares (2004b, 2004c) with a 3-segment model of the S175 containership for design conditions in regular and irregular waves. The model was mounted on a steel backbone which made elastic hull deformations negligible. They demonstrated that nonlinear characteristics were much stronger for loads than motions, and found that sagging maxima were larger than hogging maxima due to the geometry with a large flare at the bow.

Ramos et al. (2000) carried out experiments for ship motions and structural loads with a 4-segment model of the S175 containership in ballast condition. Each segment was connected with a flexible bar allowing elastic deformation. They measured motions and VBMs at the segment connectors for several of wave amplitude and frequency values. They compared results with those from linear theories using empirical formulations for calculation of slamming loads and whipping stresses. Their experimental results showed that the total bending moment could be separated into linear low frequency and whipping components.

Fonseca and Guedes Soares (2002) compared numerical results from time-domain strip theories with experimental data (Watanabe et al., 1989; O'Dea et al., 1992). Their method assumed hydrostatic and Froude–Krylov forces and effects of green water on the deck to be nonlinear, while radiation and diffraction hydrodynamic forces were linear. Transfer functions of motions from numerical methods in the bow region showed results similar to experiments with respect to wave amplitude, except in the high wave-amplitude range. The numerical method exhibited nonlinear effects for VBM, even though mean offset and amplitude were slightly overestimated at the first harmonic frequency. Experimental results of Fonseca and Guedes Soares (2004b) were compared with numerical results using the time-domain strip method in a later paper (Fonseca and

Guedes Soares, 2005), investigating effects of vertical viscous forces due to flow separation. While the introduction of vertical viscous forces had small effects on vertical-plane motions and loads, it improved prediction compared to experimental results.

Sames et al. (1999) investigated bow flare slamming loads on modern container ships using a FVM. A two-phase formulation was used to simulate overturning waves. A linear panel method, however, was applied to predict ship motions. They concluded that accurate prediction of velocity histories or coupling with a rigid-body motion solver was required to obtain realistic pressures.

To overcome these limitations in this thesis, an unsteady Reynolds averaged Navier–Stokes (URANS) solver is coupled here with a reduced set of natural modes obtained from the structure solver. As a viscous CFD solver, discretization of the geometry is explicit; viscous damping of motions is predicted; Froude–Krylov, diffraction and radiation excitation are all resolved and need not to be modeled separately.

3.2 Solution Strategy

There are several approaches to structural analysis; three ways are evaluated here to incorporate CFD predicted loads. The simplest is the assumption of rigid-body motion, in which stress and bending moment are computed by integration of forces on the ship surface. This approach is limited by its inability to model effects where elastic response is relevant, such as in whipping. The second, more complex approach is to compute forces based on rigid-body motion with CFD, and then apply those forces on a wet elastic model to predict flexural responses. The deformed geometry is not fed back into the fluid solver, so this is a one-way coupling. It requires modeling the added-mass and damping due to body flexure, since water acceleration due to deformation, viscous, and radiation effects on structural vibration are not explicitly solved in the fluid domain. The third method is to compute the flow field and elastic deformations in a two-way coupled manner. It

allows feedback of the elastic motions of the structure into the fluid solver. This can be important for computing pressure release when the hull deforms during slamming or when large deformations influence the flow field. The two-way coupling also eliminates the need to model the added-mass or fluid damping due to flexure.

This thesis investigates these three approaches. The S175 containership is studied in regular waves and the results are compared with experimental data from Ramos et al. (2000). The elastic analysis uses the commercial code, ABAQUS version 6.8, to obtain natural frequencies and mode shapes of the ship. For the one-way and two-way coupling approaches, the modal superposition transient analysis is performed using forces provided by the fluid solver. For transfer of forces and deformations between non-matching grids for fluid and structural analysis, the gluing method proposed by Maman and Farhat (1995) and Farhat et al. (1998) is applied.

3.3 Structural Load Calculation

The structural loads in the rigid model were computed using direct integration of forces. In a dynamic condition, vertical shear force due to the inertia of the ship is computed as

$$W_z(x_1) = \int_0^{x_1} m(x)\left[\dot{w} - uq + vp + (x - x_G)(rp - \dot{q}) - g_z\right] dx \tag{3.1}$$

where $m(x)$ is the longitudinal mass distribution and g_z is the z component of the gravity vector. The hydrodynamic shear force at an arbitrary location x_1 is calculated as

$$B_z(x_1) = \int_0^{x_1} F_z dA \,. \tag{3.2}$$

Assuming that hogging moment is positive, the VBM is obtained as

$$M_y(x_1) = \int_0^{x_1} [W_z(x) - B_z(x)] x dx \,. \tag{3.3}$$

Otherwise, the VBM in the elastic models is calculated by the relation between the bending moment and the curvature of the beam connector as

$$M_y = EI_y \frac{1}{r_z} \tag{3.4}$$

where EI_y is the flexural rigidity and r_z is the radius of curvature of deflected beam connector.

3.4 Simulation Design

3.4.1 Geometry and Grid

The geometry of interest was the S175 containership, used by the ITTC Seakeeping and Maneuvering committees for validation studies. Main particulars are shown in Table 3.1. Figure 3.1 presents the body plan with the draft corresponding to the ballast condition. Experimental results are available for a 1:70 model (Ramos et al., 2000) including ship flexural natural frequencies and damping ratios, measured VBM at segment connectors, and transfer functions of heave and pitch. In the structural model, the ship was split into four rigid segments, connected by elastic beams at sections $x/L_{PP} = 0.30$, 0.55, and 0.70 as shown in Fig. 3.2, mimicking the experimental setup. Two coordinate systems were used. The first was a ship system where the x-axis pointed toward the bow from the AP, the z-axis pointed upward, and the y-axis followed the right hand rule. The second was the Earth system, where the axes were fixed and chosen to be coincident with the ship coordinates at rest. CFD computations were performed in the Earth system, while the rigid-body motion equations and the elastic equations were solved in the ship system.

Figure 3.3 shows an outline of overset grid system for the fluid solver. One double-O boundary layer grid was used for the boundary layer grid, while a Cartesian grid was used for the background grid. The boundary layer grid moves following 6-DOF

motions computed for the ship. In a general problem, the background grid follows the ship in surge, sway, and yaw motions, but is not allowed to pitch, heave, or roll. This guarantees a fine grid near the free surface. For this case where only pitch and heave were present, only the starboard side was computed using a symmetry condition on the center plane. The grid sizes were 749k and 1481k for the boundary layer and background grids, respectively.

The finite element model used for the one-way coupling is shown in Fig. 3.4. The hull surface and basic internal frames were modeled with shell elements, and each segment was connected with beam elements. The shell elements on hull surface were triangles, and the acoustic fluid elements were tetrahedrons. The structure grid for hull surface and internal frame are shown in detail in Fig. 3.5. The fluid region was removed for the dry modes. The discrepancy between fluid and structure grids as associated by the gluing method is presented in Fig. 3.6, which shows the hull deformation of the fluid grid strongly associated with the structure grid in large deformation situations.

3.4.2 Natural Frequencies and Mode Shapes

The material properties of different model components for the structural analysis are summarized in Table 3.2. Seventy-seven concentrated point masses were distributed along the top nodes of the internal frame. Mass distribution used in this thesis satisfied total mass, longitudinal center of gravity location, and radius of gyration for pitch of the model. It is compared with the mass distribution proposed by Ramos et al. (2000) in Fig. 3.7. Both of these mass distributions failed to predict the experimental static vertical bending moments, which could not be matched with an all-positive mass distribution while at the same time satisfying the total mass, pitch radius of gyration, and longitudinal location of the center of gravity. Figure 3.8 compares the static VBMs with the experimental data. The static VBMs, as computed by each of the numerical models, showed similar values, whereas there was still a large discrepancy between the numerical

and experimental data. The reasons for these differences were unclear. Unfortunately, mass distribution was not measured by Ramos et al. (2000) and could not be uniquely defined with the available data.

The mode shapes corresponding to the first three natural frequencies obtained through the modal analysis are presented in Fig. 3.9, which were used for the modal superposition analysis. The natural frequencies for the two-way coupling were calculated through numerical free vibration tests using CFDShip-Iowa with considering FSI, while those for the one-way coupling were obtained from the structural analysis in the wet mode. The natural frequencies for the one-way and two-way coupling approaches are compared to experimental results in Table 3.3. Differences with experiments were smaller than 3% for the first and second modes in the two-way coupling. They were between 5% and 7% in the one-way coupling. The third mode underpredicted by about 14%. Damping ratios reported in Ramos et al. (2000) were used for both the one-way and two-way coupling approaches. These are listed in Table 3.4.

3.4.3 Test Cases

Seven cases were studied, as summarized in Table 3.5. Some directly corresponded to Ramos et al. (2000). The wave height (H) was non-dimensionalized with the ballast draft (T_b), and the wave length (λ) was non-dimensionalized with the ship length (L_{PP}). Test cases covered a wide range of wave heights with $H/T_b = 0.32$, 0.71, 0.87, and 1.08 for wave length $\lambda/L_{PP} = 1.0$ (Cases 1, 4, 6, and 7). The ship was free to heave and pitch so that the effect of both bottom and flare slamming on ship motions and structural loads were monitored. Operations in regular seas, characterized by wave lengths of $\lambda/L_{PP} = 0.68$, 1.0, 1.5, and 2.0 at height $H/T_b = 0.71$, were also simulated to evaluate the transfer functions for heave and pitch degrees of freedom (cases 2 through 5). The Froude number was 0.2 for all cases. The time step was chosen so that

the cases with $\lambda / L_{PP} = 1.0$ had 216 time steps per wave period, while all others had 100 time steps per period (T).

3.5 Results and Discussion

3.5.1 Ship Motions

Figures 3.10 and 3.12 show time histories and harmonic amplitudes of heave and pitch motions for wave length $\lambda / L_{PP} = 1.0$ at different wave heights. ξ_3 and ξ_5 represent the motions for heave and pitch, respectively. ζ_a and k is the wave amplitude and number, respectively. The harmonic amplitudes of heave and pitch motions in Fig. 3.12 are nondimensionalized as same manner as in Fig. 3.11. Mean heave increased in proportion with wave height, while the first harmonic amplitude decreased. For small wave heights, the ship exhibited dynamic sinkage, but tended to emerge from $H / T_b = 0.87$ as the wave height increased. For pitching motion, the zeroth and first harmonic amplitudes decreased with increasing wave height. Mean pitch was positive for $H / T_b = 0.32$ (bow-down attitude), but this reversed for larger wave heights. The second harmonic amplitudes of heave and pitch motions tended to increase with wave height.

Heave and pitch accelerations for various wave heights and $\lambda / L_{PP} = 1.0$ are shown in Fig. 3.11. α_3 and α_5 represent heave and pitch accelerations, respectively. It was clear that the acceleration showed slamming-induced response for steeper waves around $t / T = 0.1$. This was due to a bow bottom slamming event, while the flattening region around $t / T = 0.3$ corresponded to bow flare slamming. Strength of the events increased with wave height and bottom impacts occurred later at larger waves. Flare slamming was primarily responsible for the nonlinear reduction in the amplitudes of heave and pitch and the increase of the mean heave, by effectively preventing the bow from sinking but not from rising. Harmonic amplitudes of heave and pitch accelerations at $\lambda / L_{PP} = 1.0$ are compared in Fig. 3.13 for various wave heights. The harmonic amplitudes are nondimensionalized as same manner as the time histories of accelerations.

Mean of heave acceleration increased with wave height as the heave motion, while mean of pitch acceleration did not have significant variation. The trends of the first and second harmonic amplitudes of accelerations were similar to those of motions.

Sequential underwater views, including the slamming events for case 7, are illustrated in Fig. 3.14, showing the boundary layer and pressure distribution on the hull. At $t/T = 0.01$, the bow was out of the water, showing a pair of vortices at $x/L_{PP} = 0.8$ that were generated by the upward motion of the bow. At $t/T = 0.10$, the bow bottom slammed against the free surface with a consequent peak in pressure. At this moment, a portion of the bottom around $x/L_{PP} = 0.84$ was still dry, while the boundary layer thickened downstream near the impact point. As the bow descended further, the pressure decreased, but at $t/T = 0.29$ the bow flare was submerging, creating a large area of high pressure characteristic of flare slamming. Other salient flow features visible in the solutions were the evolution of the bilge vortices developed due to the ship motions, and the variation of the boundary layer thickness at the stern and wake.

Figures 3.15 and 3.16 depict the predicted transfer functions of heave and pitch. They also show the experimental data (Ramos et al. 2000) and linear strip theory predictions from Ramos and Guedes Soares (1998). After a peak in the pitch response occurring at dimensionless wave frequency $\omega_0\sqrt{L_{PP}/g} = 2$, it rolled off quickly. The ship response for frequencies higher than three was essentially zero. The numerical results agreed well with the experimental results. The heave response exhibited no peak for either experiments or CFD computations, and rolled off slower than the pitch response at higher wave frequencies. For $\lambda/L_{PP} = 1.0$, the heave and pitch transfer functions showed nonlinear effects with significant decrease on the response as the wave height increased as shown in Fig. 3.12. This behavior was caused by the flared bow that resulted in significantly increased buoyancy for large bow-down motions. The decrease of the heave transfer function with the increase of wave height at $\lambda/L_{PP} = 1.0$ was

relatively smaller than that in the pitch transfer function. These trends were consistently predicted by the CFD computations.

3.5.2 Structural Loads

For the analysis of structural loads the study concentrates on cases 4 and 6, for which experiments are available, but some results are also shown for cases without experimental data. A positive bending moment indicates that the model is hogging. SG1, SG2, and SG3 are the cut positions indicated in Fig. 3.2. The experimental VBM is reported in model scale.

Figures 3.17 and 3.18 show the time histories of the VBMs for cases 4 and 6, respectively. These include rigid and elastic model results and experimental data from Ramos et al. (2000). The VBM is reported relative to the static value. The slamming events could be clearly observed on the rigid-body model around $t/T = 0.1$ (bottom slamming) and $t/T = 0.3$ (flare slamming). These events were coincident in time with those reported in Fig. 3.11 for the acceleration. The VBMs of the elastic models did not peak during the slamming events; instead, they oscillated as in the experimental observations. The response of the VBMs for the elastic models was similar to the experiments, though CFD tended to overpredict sagging moment. The VBM of the one-way coupling showed a phase-lag after the slamming in case 6, while the two-way coupled approach could properly predict the resonance frequency and phase. The overprediction of the VBMs by CFD is difficult to explain, but may be due to the uncertainties in the mass distribution.

Spectral analysis results for the time histories of the VBMs in Figs. 3.17 and 3.18 are presented in Figs. 3.19 and 3.20. The first mode peak at around 9.5 Hz was evident in the both elastic models and experiments. In the both elastic models, the second mode was clearly observed around 25 Hz at SG1 and SG3, while the third mode was detected around 43 Hz only at SG3. The peaks for the second and third modes were less

pronounced in the two-way than in the one-way coupling approach, and the responses of these modes were essentially non-existent in the experiments.

Figures 3.21 to 3.23 show dimensionless VBMs for various wave heights in the rigid, one-way coupling, and two-way coupling approaches, respectively. The rigid model did not detect both bottom and flare slamming at $H/T_b = 0.32$. For larger wave heights, slamming effects increased significantly with wave height. This was true also for the nonlinearity of the response, in particular for SG2 and SG3 near the bow. The one-way and two-way coupling approaches showed similar results. It was clear that the elastic models essentially responded to the flare slamming because the amplitude of fluctuation increased significantly after the flare slamming. In all models the bottom slamming occurred later as the wave height increased, due to higher rise of the bow as the pitch angle increased, whereas the flare slamming occurred slightly earlier as the falling bow found a higher crest on its way down. The two-way coupling provides similar solution to the one-way coupling, since the deformation in all cases is very small. However, the VBM of the two-way coupling shows the changes in the phase and amplitude after the slamming as shown in Fig. 3.24. Note that the changes increase with wave height, showing an evident increase in elastic response.

The zeroth, first and second harmonic amplitudes of the dimensionless VBMs at SG2 are shown in Fig. 3.25 for various wave lengths at wave height $H/T_b = 0.71$. All models showed the same results essentially, with the exception of the dimensionless encounter frequency 2.5, corresponding to $\lambda/L_{PP} = 1.0$, which was near the ship's resonance frequency. All models showed good agreement with the experiment for the first and second harmonics, while the zeroth harmonic had offset. The zeroth harmonic was negative for all wave lengths, indicating that sagging moment dominated through the wave period. All harmonic amplitudes were largest for the resonant wave length $\lambda/L_{PP} = 1.0$. This was an interesting result since it was expected that larger heave and pitch responses occurred at lower wave frequencies (see Figs. 3.15 and 3.16) would cause

larger fluctuation in the VBM. On the other hand, maximum response could also be expected for λ / L_{PP} around 1.0, which would cause wave crests located at the bow and stern with a trough at midships for the 0 degrees phase, and troughs at the bow and stern with crest at midships for the 180 degrees phase. The rigid model had no apparent second harmonic response, while the elastic models showed a second harmonic response at wave length $\lambda / L_{PP} = 1.0$.

The harmonic amplitudes of the dimensionless VBMs at SG2 for various wave heights at $\lambda / L_{PP} = 1.0$ are compared in Fig. 3.26. All models showed similar trend in all harmonics. The slopes of amplitude variation at all harmonics changed after slamming events were occurred. The trend of the numerical simulations for the zeroth harmonic was different from the experiment, while the first and second harmonics showed a same tendency. The variation in the second harmonic amplitude was more dominant than the other harmonic amplitudes.

To investigate the differences on motions and accelerations between the one-way and two-way coupling approaches, the time histories of case 7 for the both elastic models are compared in Figs. 3.27 and 3.28. The accelerations for the two-way coupling oscillated around those for the one-way coupling, while there were no perceptible differences in motions for the both models.

3.5 Conclusions

Three FSI methods to compute structural loads on surface ships were presented. One-way and two-way coupled elastic methods as well as a rigid model method were described. In the rigid model the bending moment was obtained by direct integration of the forces on the rigid-body surfaces. The elastic representation used the same forces applied to an elastic model based on the modal superposition. The two-way coupling method deformed the fluid grid according to the structural displacements, while the structural deformation did not feed back to the fluid solver in the one-way coupling.

These models were applied to the S175 containership to calculate wave-induced structural loads in regular waves.

The numerical results of heave and pitch responses agreed well with the experimental data except for a slight underestimation of pitch response at shorter wave frequencies. The time histories of the VBMs from the rigid and elastic models showed trends similar to the experiments. The significant changes in the VBMs due to the slamming events were coincident in time with the variation of accelerations. Spectral analyses of the VBMs showed peaks at the natural frequencies for the first, second, and third mode as predicted by the numerical models. The experiments had one peak only at the first natural mode. The VBMs predicted by the elastic models did not peak during the bottom slamming events, while the effect was clearly seen with the rigid model. On the other hand, the elastic models captured the ringing of the VBMs observed in the experiments, which was caused primarily by the bow flare slamming. The one-way coupled approach provided solution quality similar to the two-way coupled approach. The two-way coupling method, however, showed the effects of structural deformation on the amplitude and phase of VBMs and the fluctuation of heave and pitch accelerations.

Table 3.1 Main particulars of the model ship

L_{PP} (m)	2.50
B (m)	0.363
T_b (m)	0.10
Mass (kg)	48.8
L_{CG} (aft of midship)	0.8% L_{PP}
Pitch radius of gyration (m)	0.61

Table 3.2 Material properties for the structural analysis

	Structure	Connector	Fluid
Density (kg/m^3)	0.01	1200	997
Young's Modulus (Pa)	1.7×10^{13}	1.4×10^{10}	2.2×10^{9}
Poisson Ratio	0.29	0.29	-

Table 3.3 Natural frequencies for the experiment and elastic models

	Experiment (Hz) (Ramos et al. 2000)	One-way (Hz)	Two-way (Hz)
Mode 1	9.8	9.1	9.5
Mode 2	26.4	25.2	25.8
Mode 3	53.9	46.8	46.1

Table 3.4 Damping ratio

Mode 1	2.79%
Mode 2	5.58%
Mode 3	9.97%

Table 3.5 Summary of the test cases

Case ID	Fr	λ/L_{PP}	H/T_b	Run ID (Ramos et al. 2000)
1	0.2	1.00	0.32	4
2	0.2	2.00	0.72	7
3	0.2	1.50	0.70	8
4	0.2	1.00	0.71	9
5	0.2	0.68	0.71	-
6	0.2	1.00	0.87	12
7	0.2	1.00	1.08	-

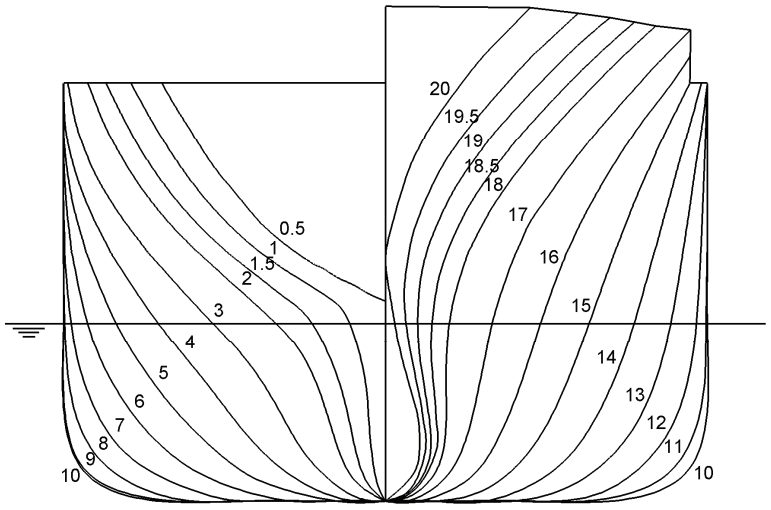

Figure 3.1 Body plan of the model ship (S175)

Figure 3.2 Coordinate system and position of the strain gages

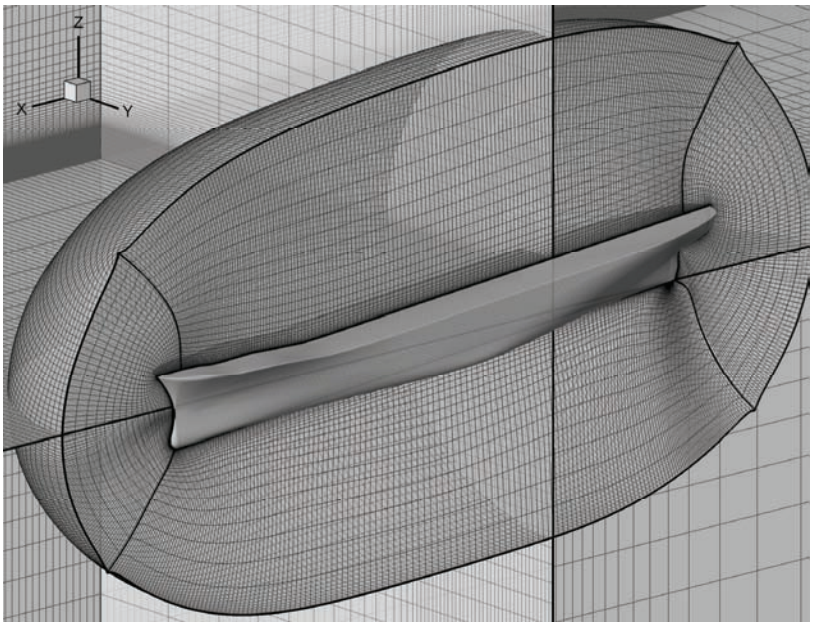

Figure 3.3 Outline of the overset grid system for the fluid analysis

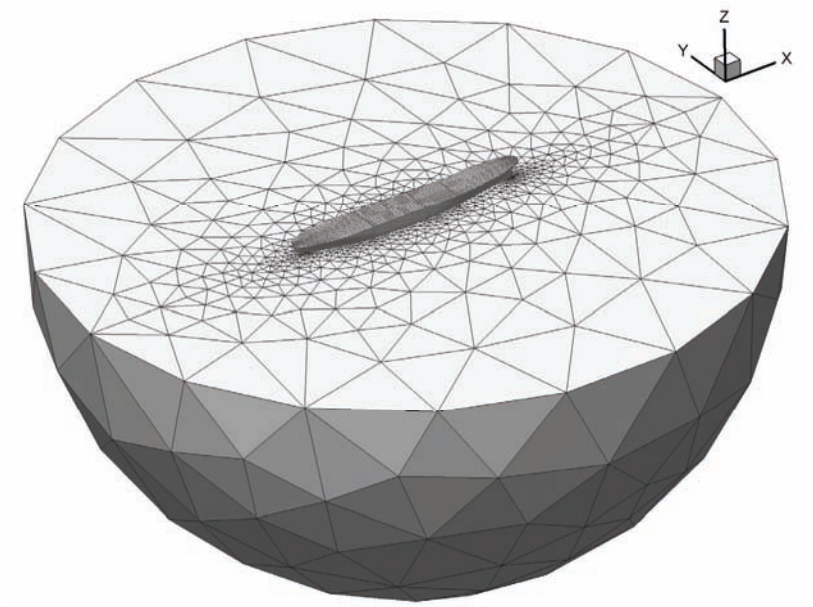

Figure 3.4 Overview of the grid system for the structural analysis at the wet condition

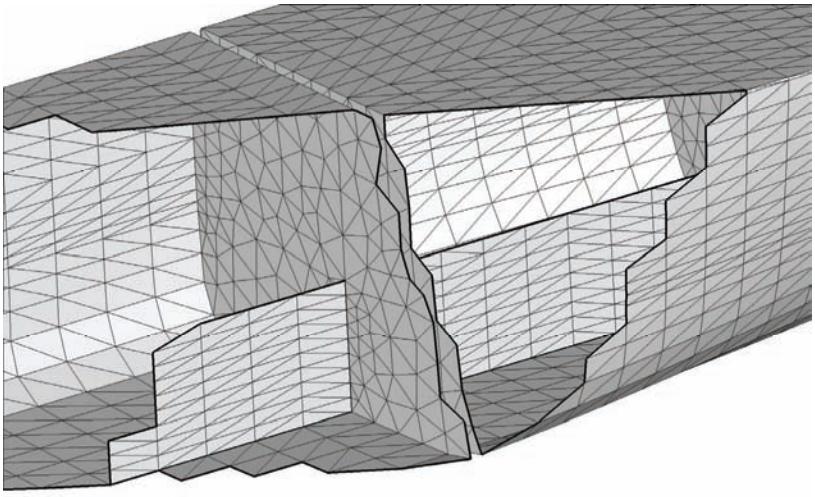

Figure 3.5 Structure grid for the hull surface and the internal frame

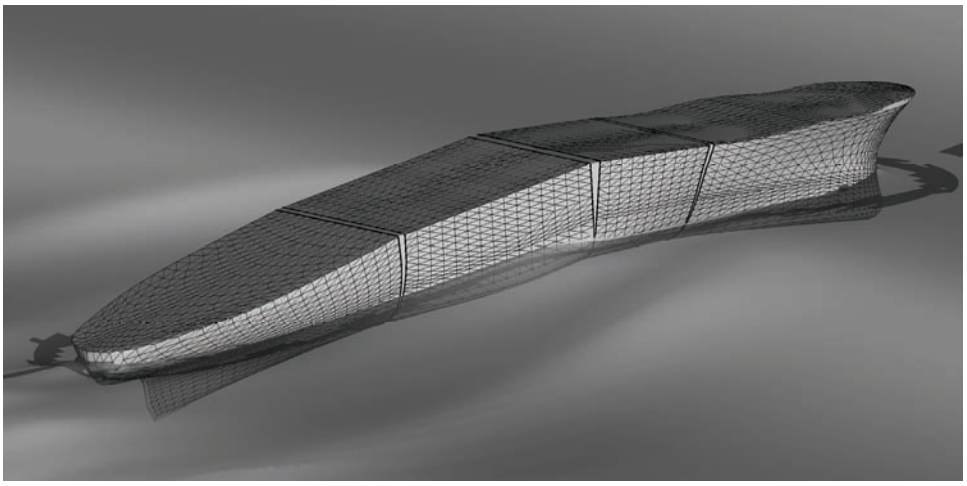

Figure 3.6 Hull deformation of the fluid grid strongly associated with the structure grid (shaded hull: fluid grid surface, meshed hull: structure grid)

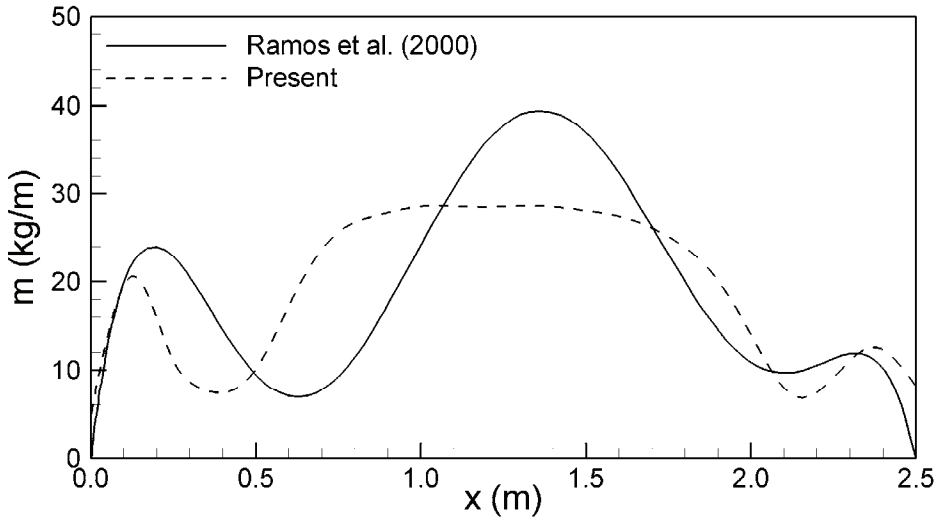

Figure 3.7 Applied mass distribution

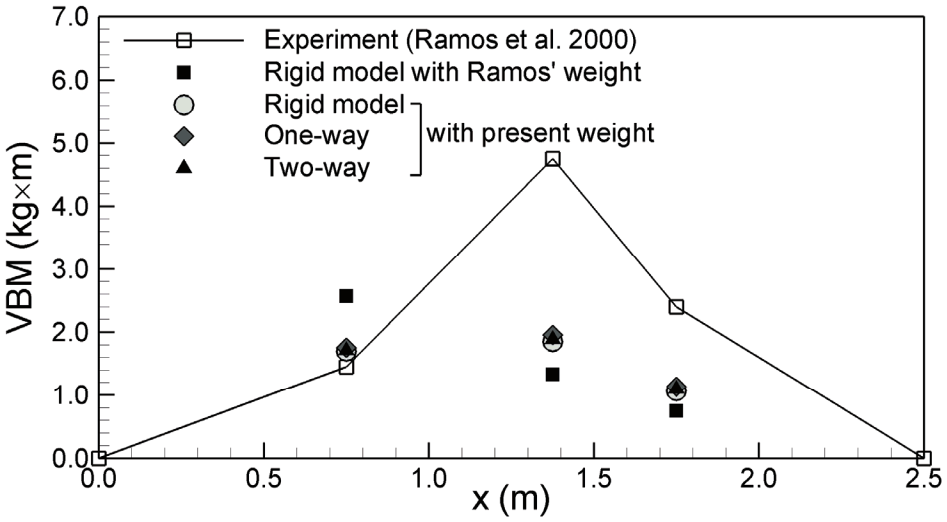

Figure 3.8 Comparison of still water bending moments

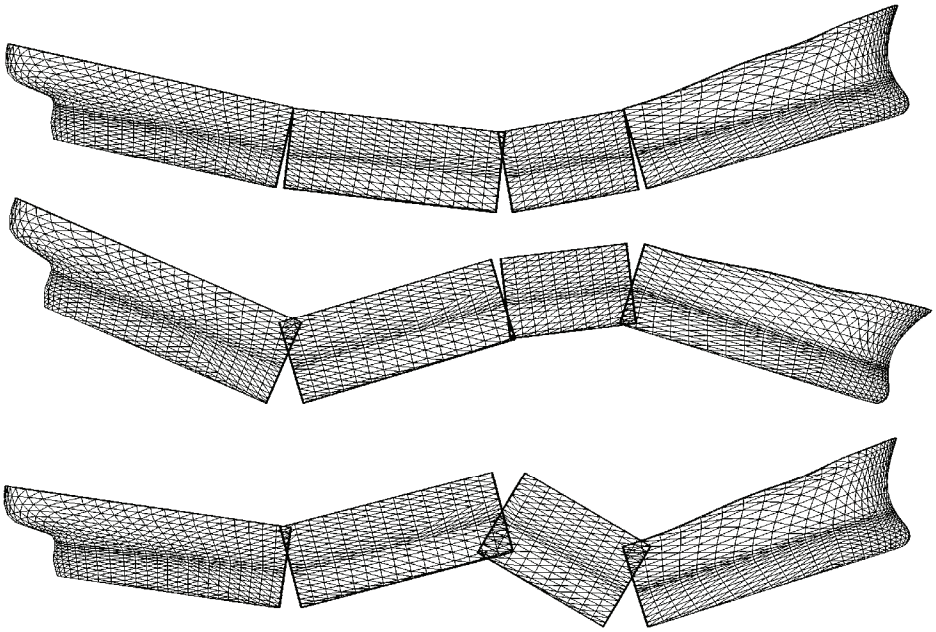

Figure 3.9 Natural mode shapes for the elastic models (top: mode 1, middle: mode 2, bottom: mode 3)

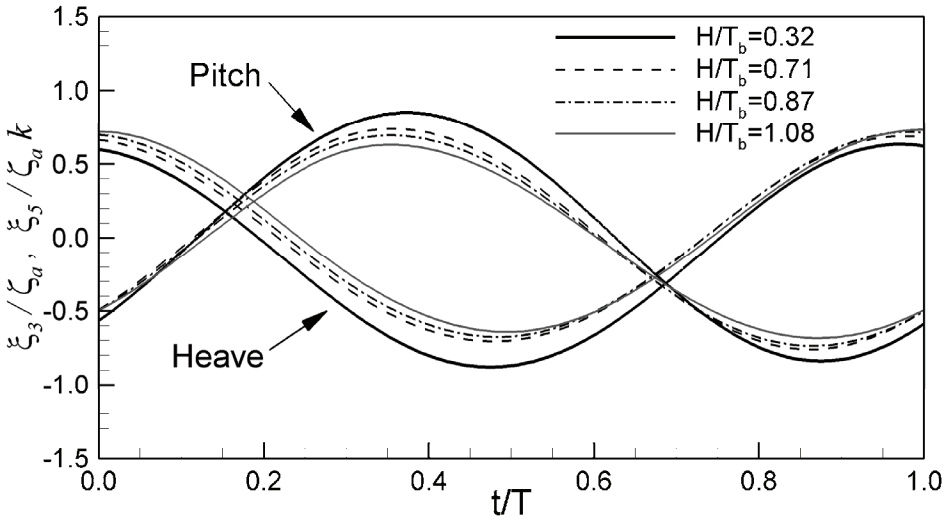

Figure 3.10 Heave and pitch motions for $\lambda / L_{PP} = 1.0$

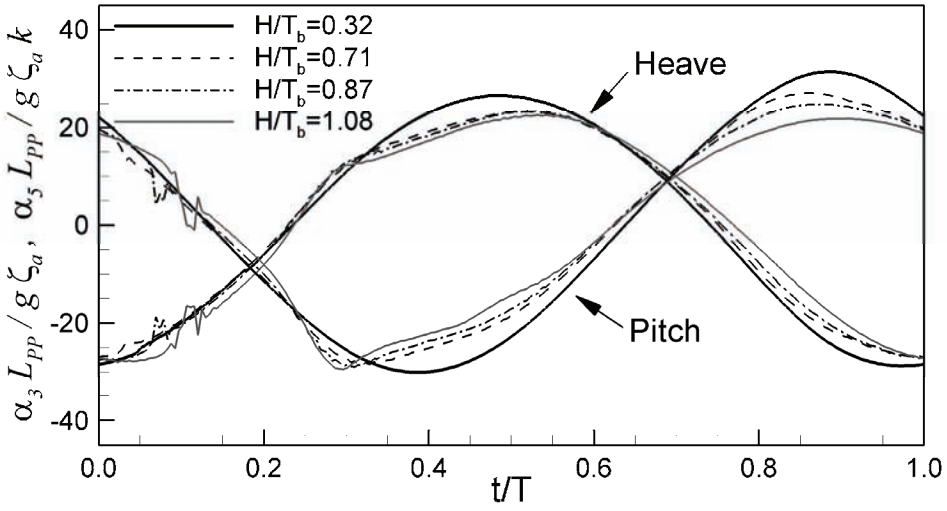

Figure 3.11 Heave and pitch accelerations for $\lambda / L_{PP} = 1.0$

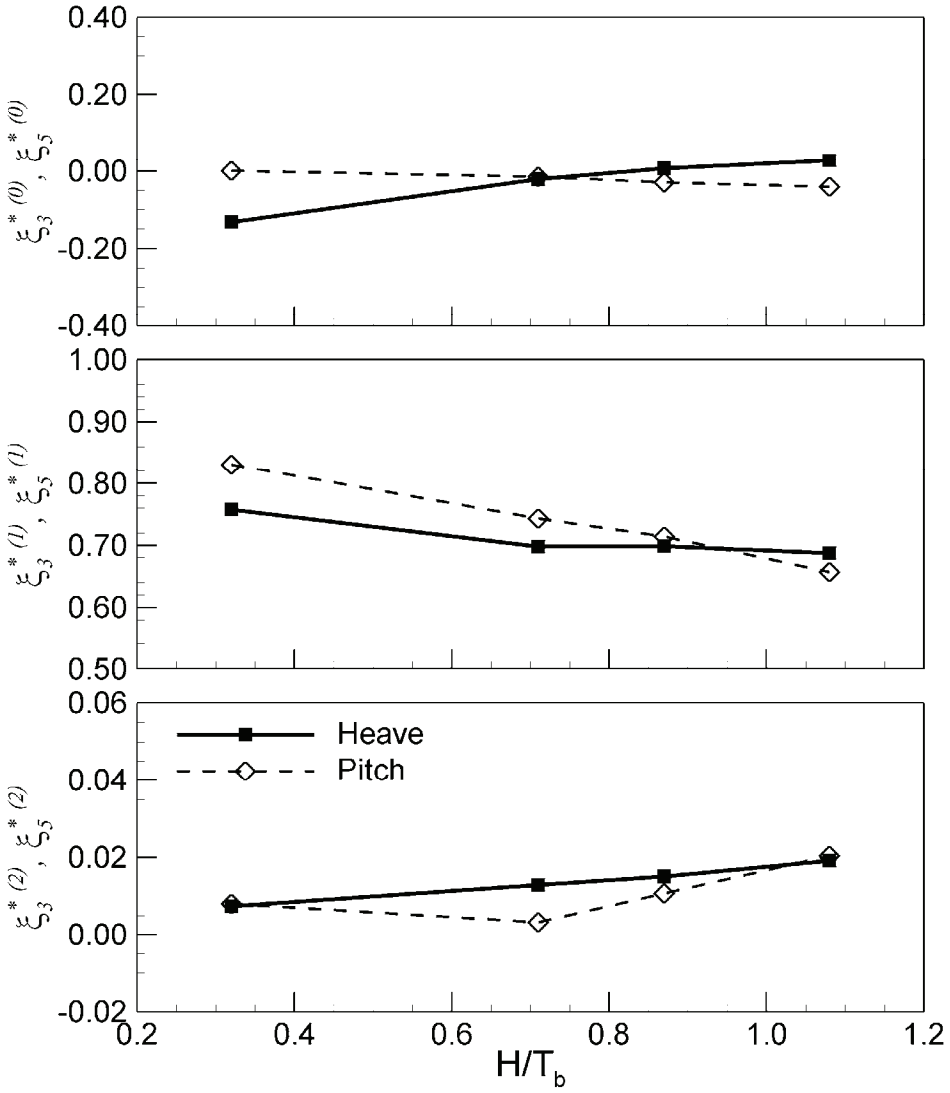

Figure 3.12 Harmonic amplitudes of heave and pitch motions for various wave heights at $\lambda / L_{PP} = 1.0$ (top: zeroth harmonic, center: first harmonic, bottom: second harmonic)

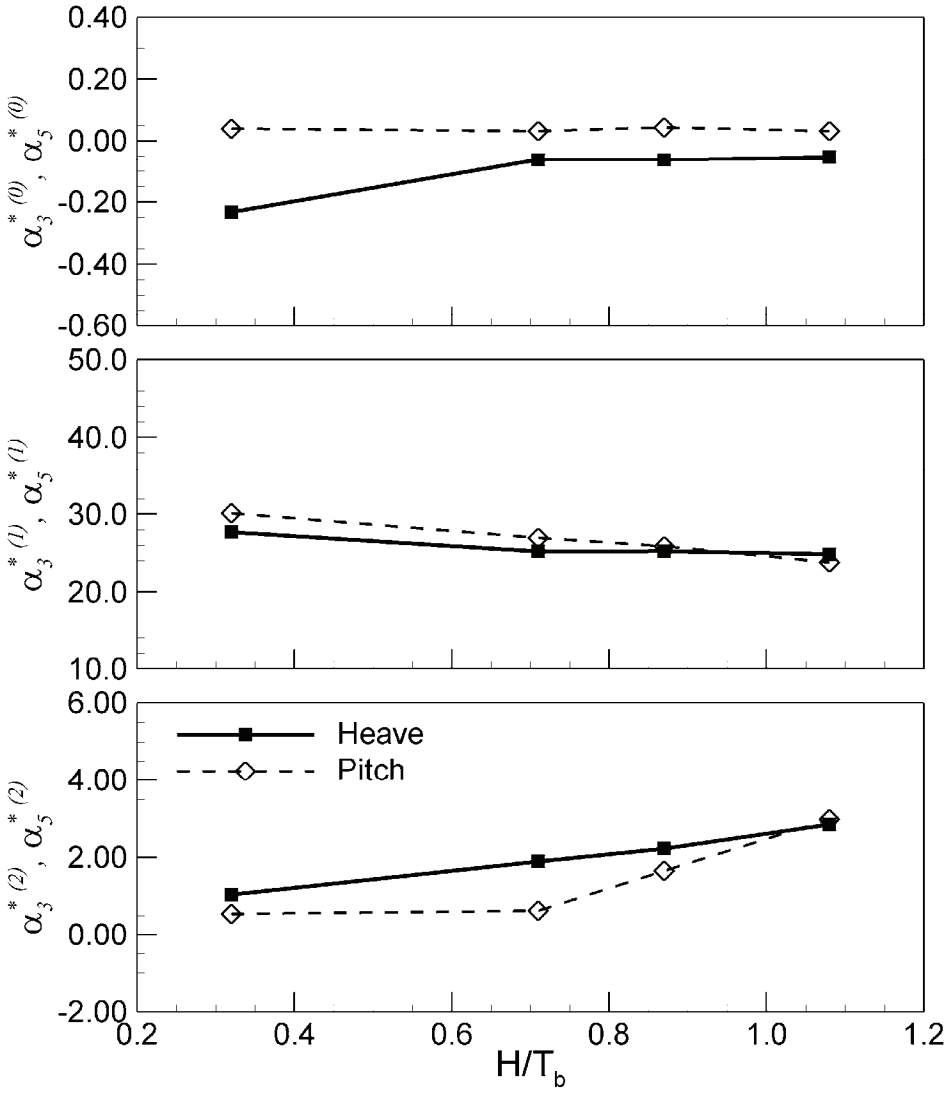

Figure 3.13 Harmonic amplitudes of heave and pitch accelerations for various wave heights at $\lambda / L_{PP} = 1.0$ (top: zeroth harmonic, center: first harmonic, bottom: second harmonic)

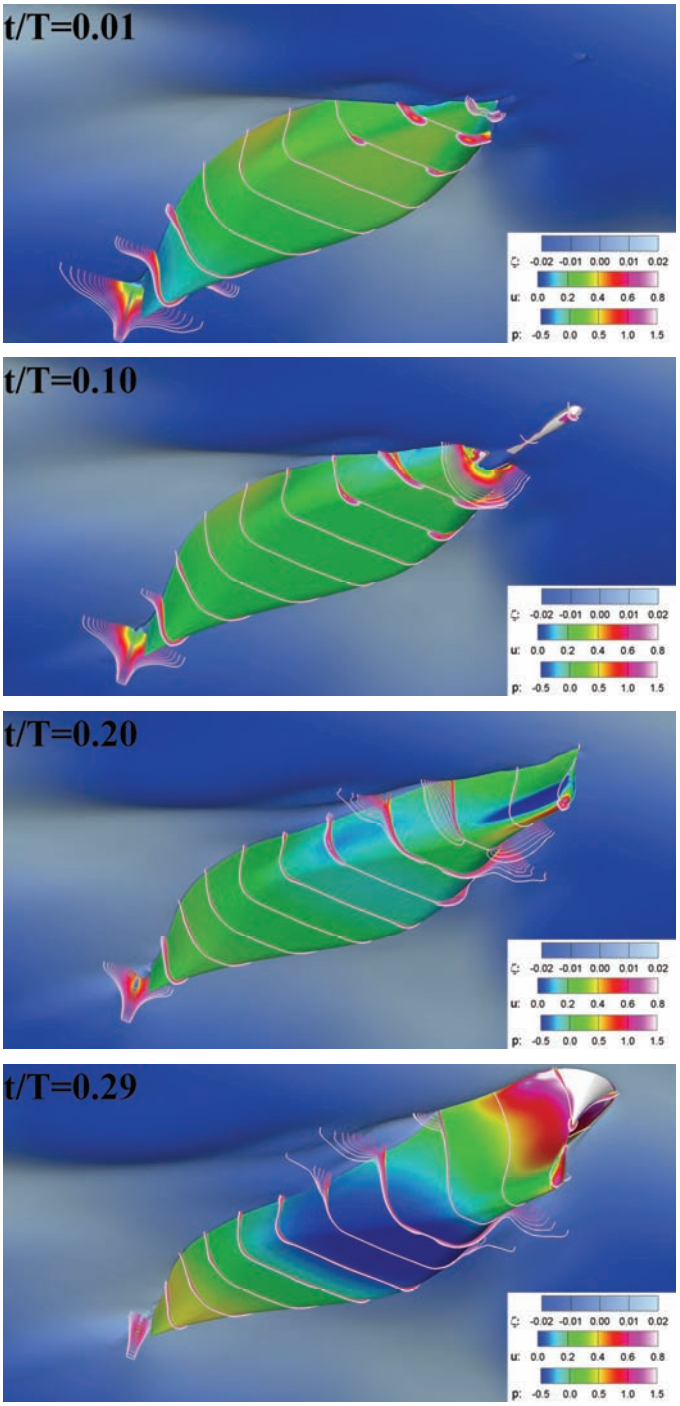

Figure 3.14 Sequential underwater views for case 7 ($t/T = 0.10$: bottom slamming, $t/T = 0.29$: flare slamming)

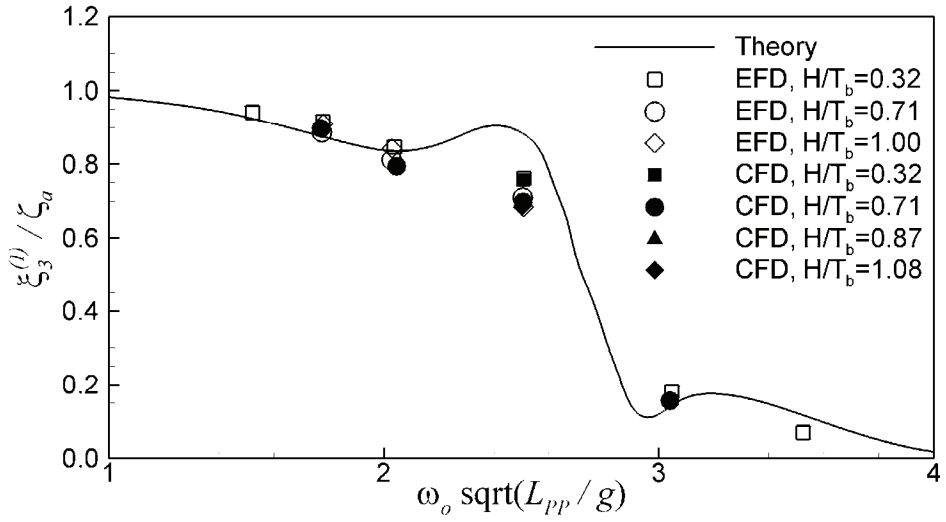

Figure 3.15 Transfer functions of heave motion

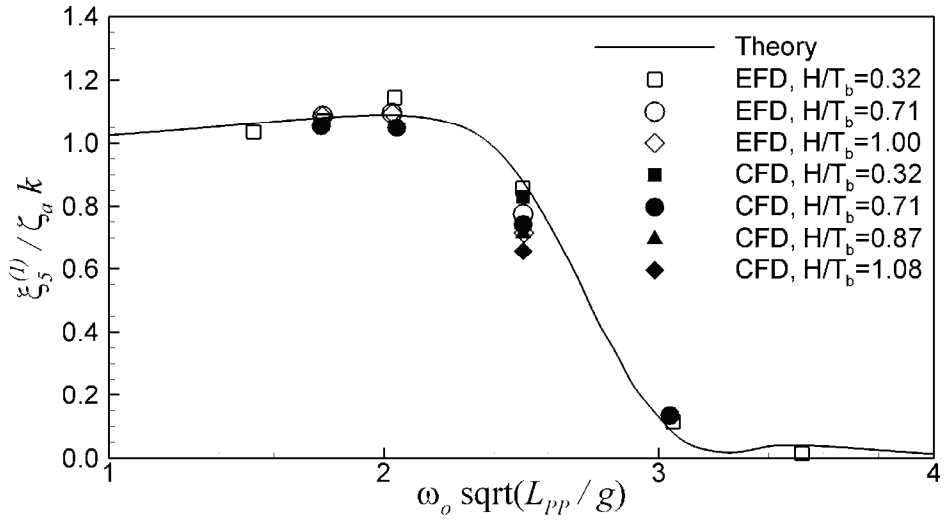

Figure 3.16 Transfer functions of pitch motion

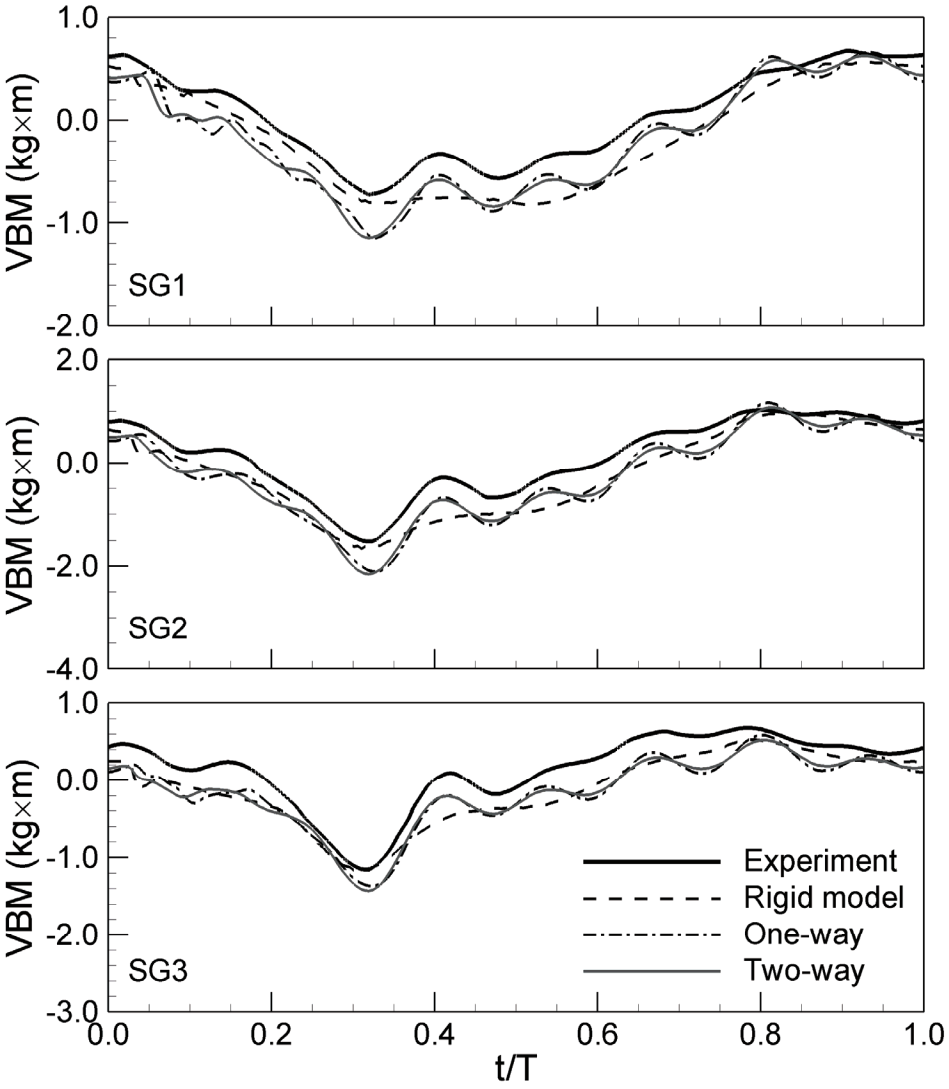

Figure 3.17 Time histories of the VBMs for case 4

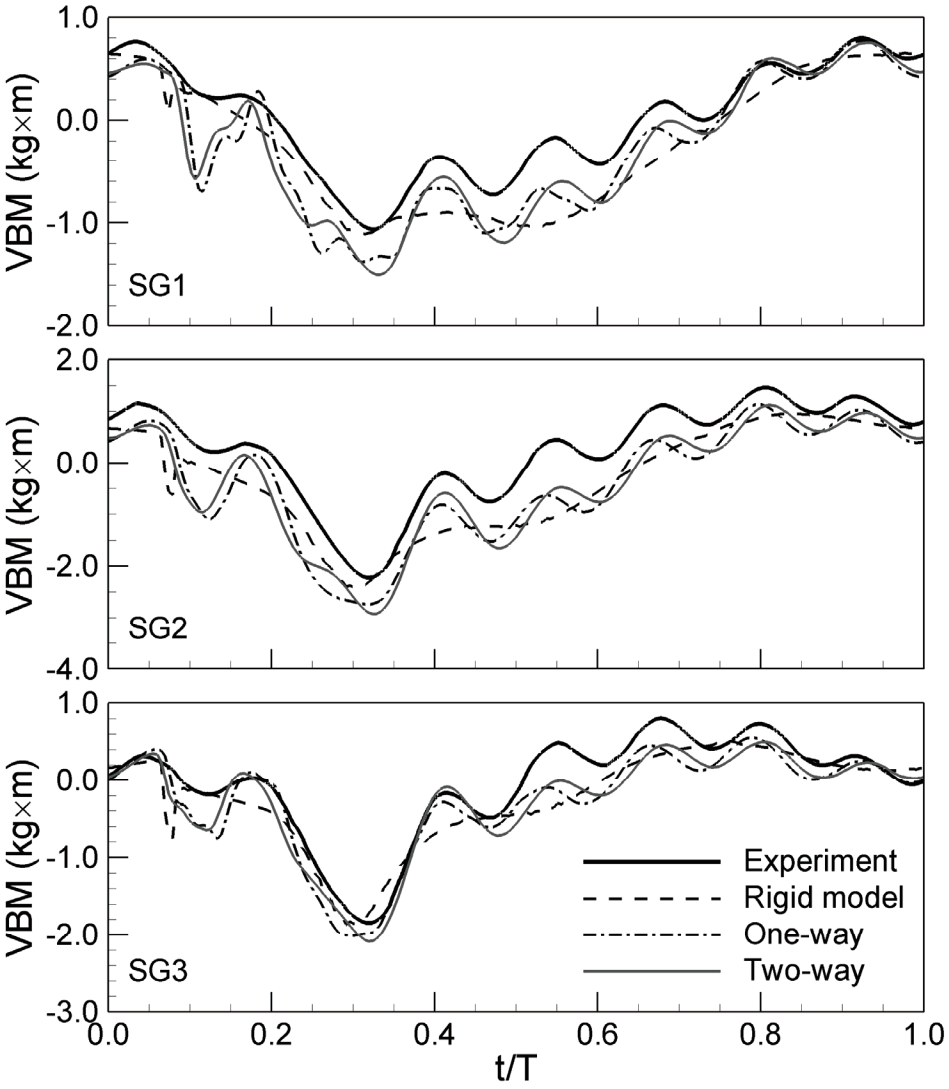

Figure 3.18 Time histories of the VBMs for case 6

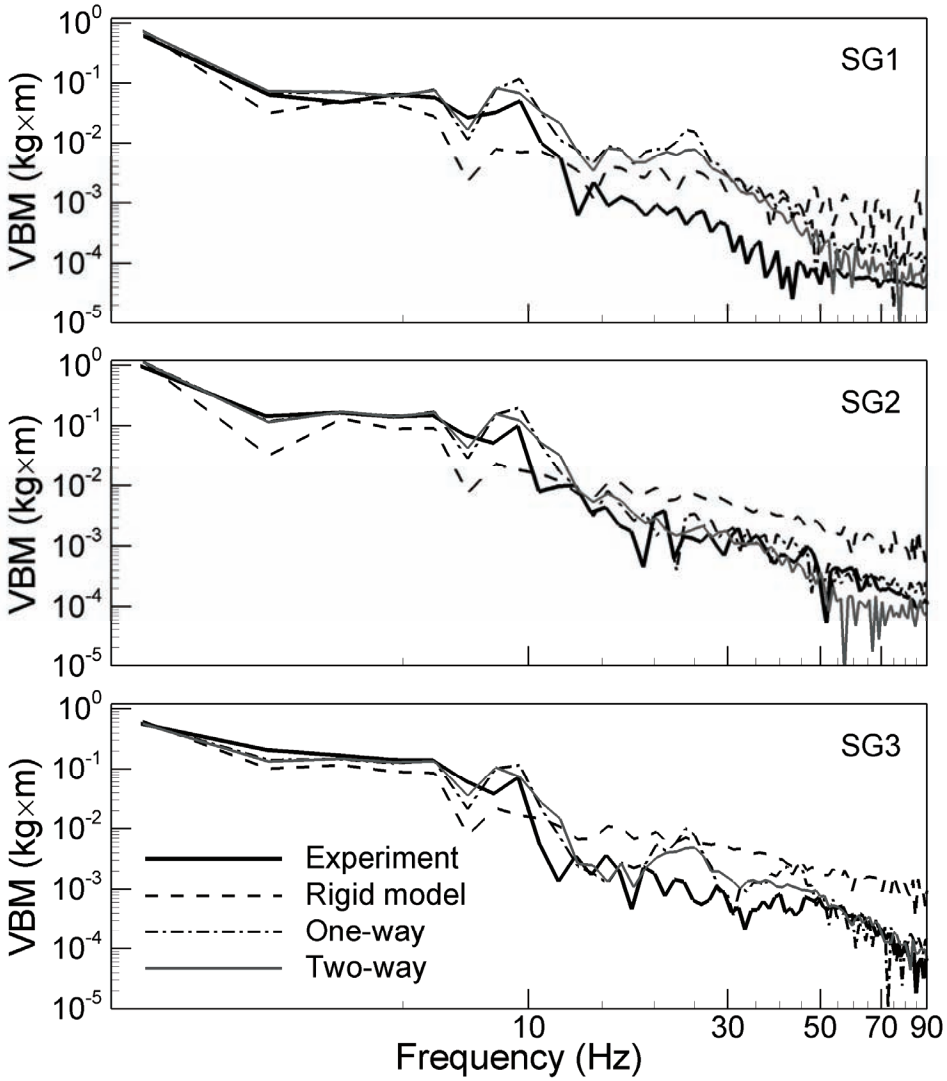

Figure 3.19 Spectral analyses of the VBMs for case 4

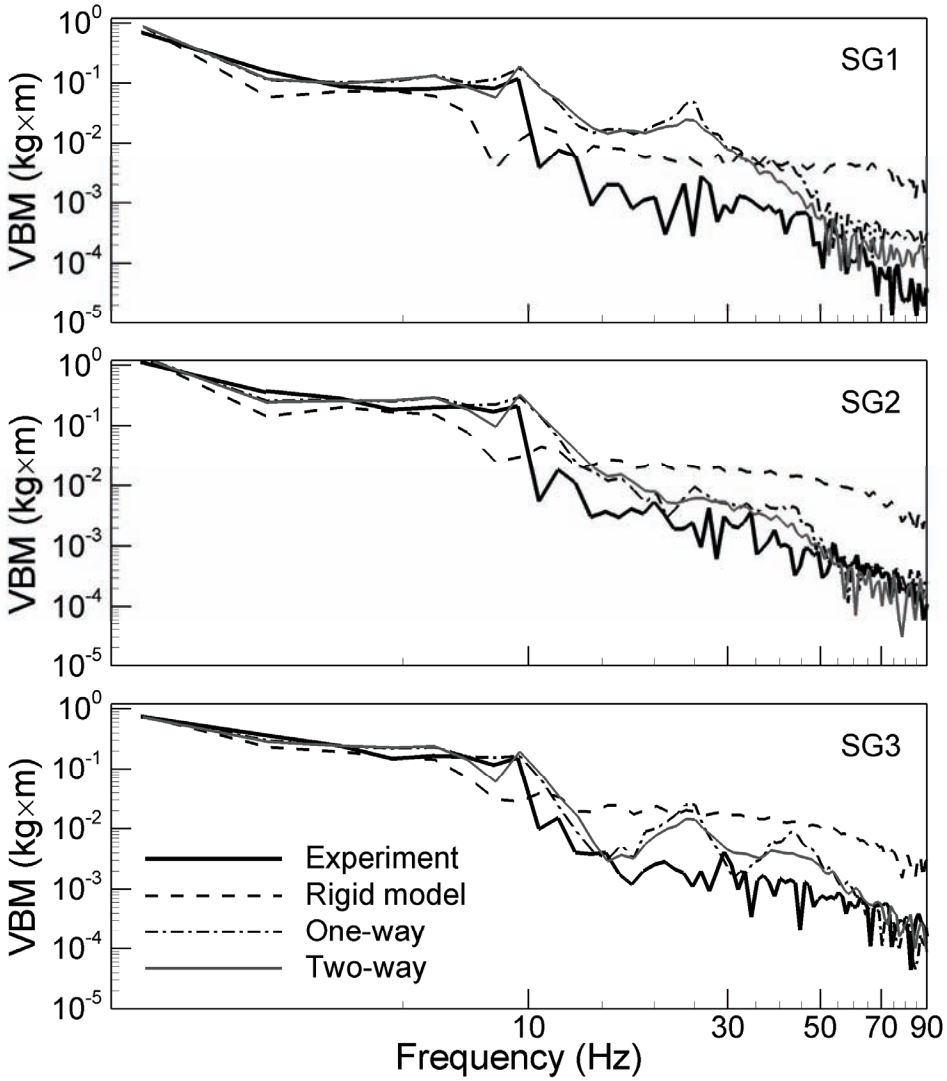

Figure 3.20 Spectral analyses of the VBMs for case 6

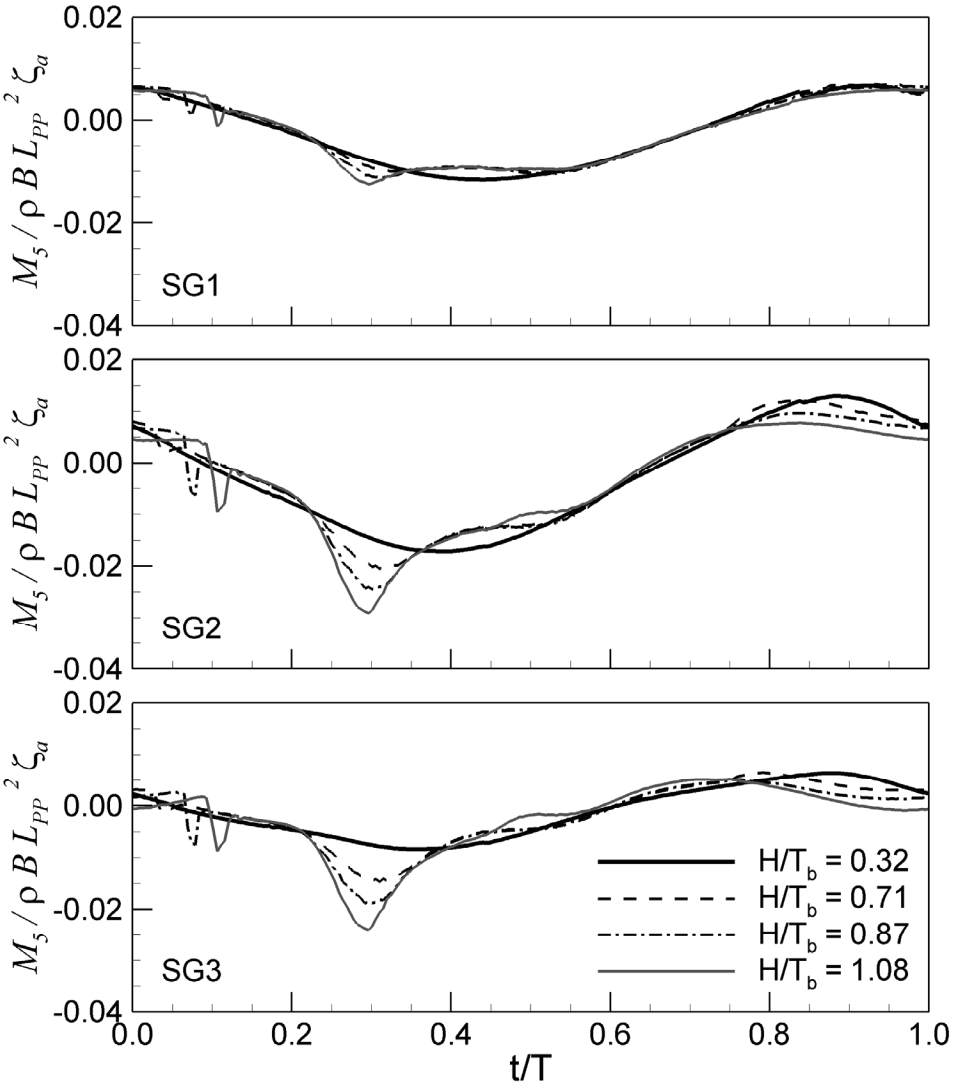

Figure 3.21 Dimensionless VBMs for various wave heights at $\lambda / L_{PP} = 1.0$ (rigid model)

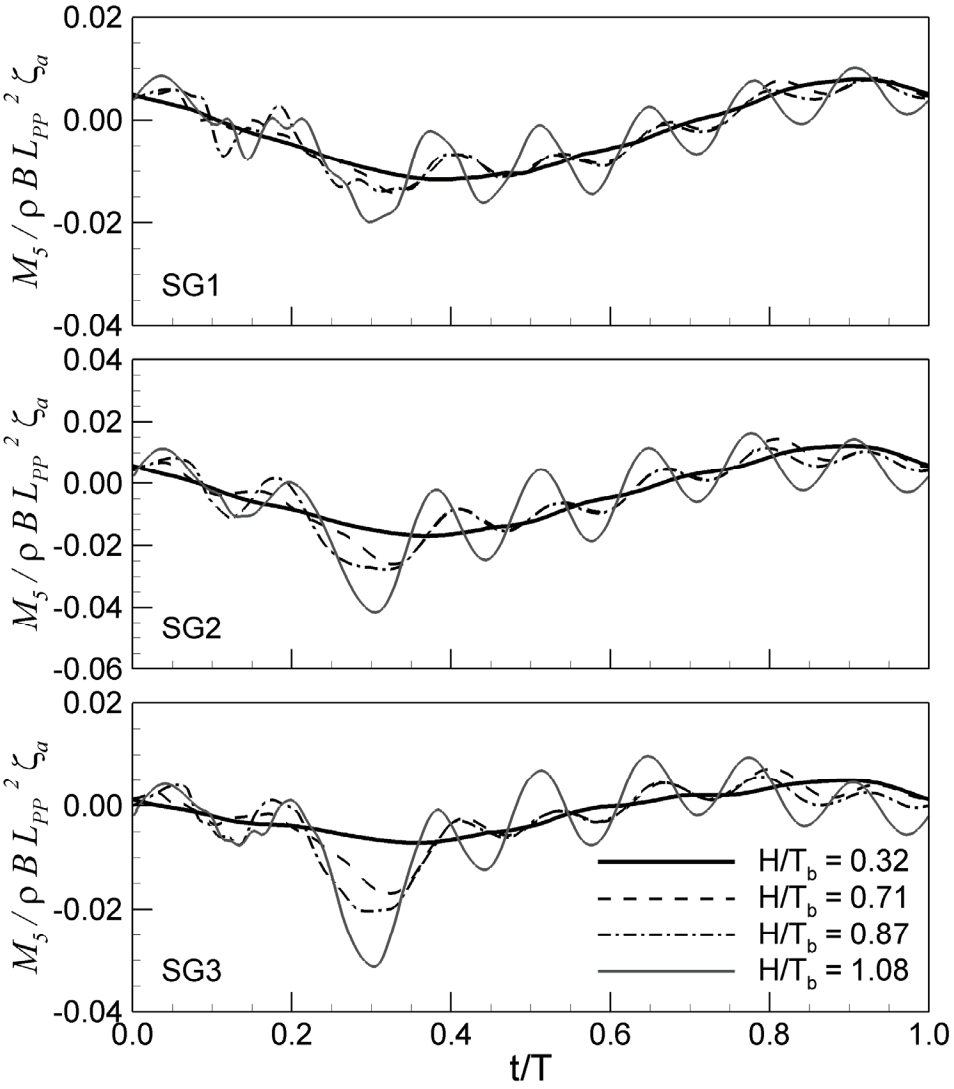

Figure 3.22 Dimensionless VBMs for various wave heights at $\lambda / L_{PP} = 1.0$ (one-way)

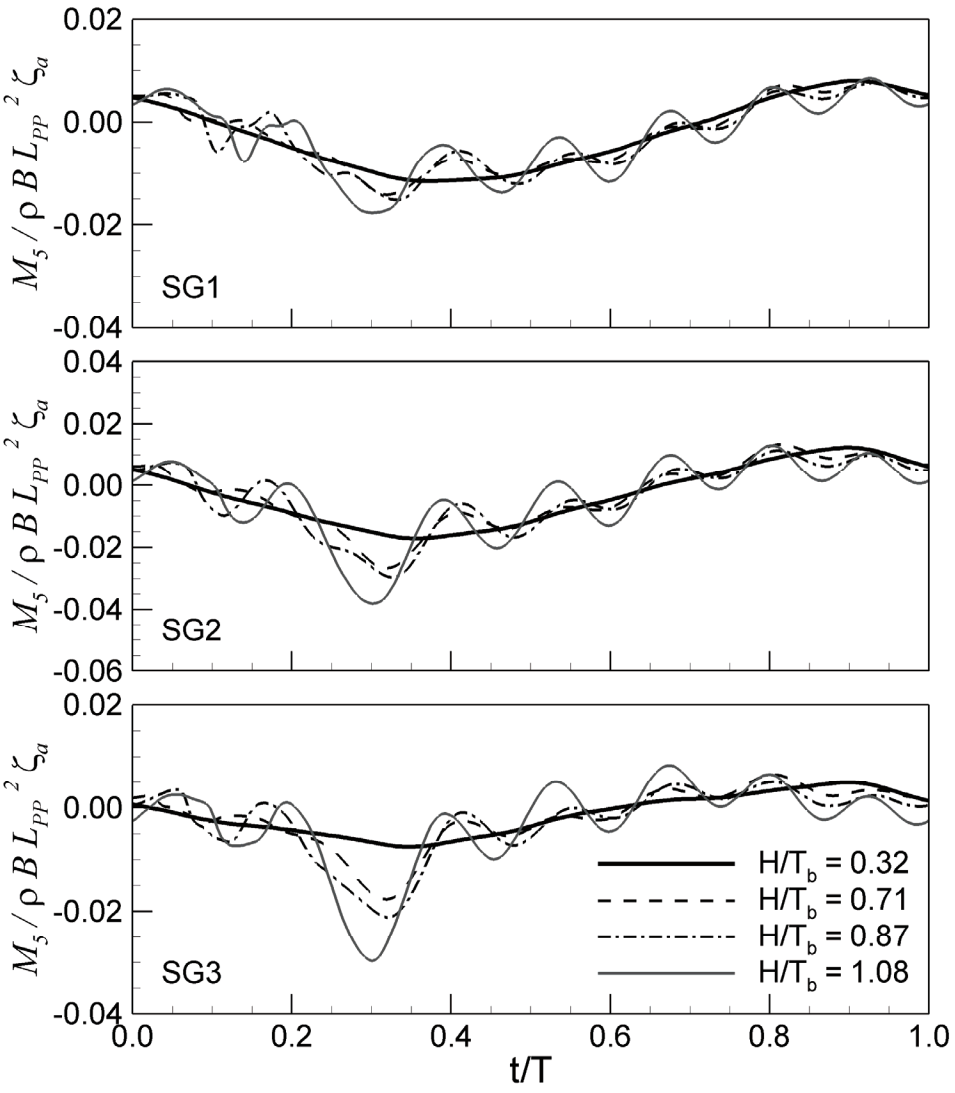

Figure 3.23 Dimensionless VBMs for various wave heights at $\lambda / L_{PP} = 1.0$ (two-way)

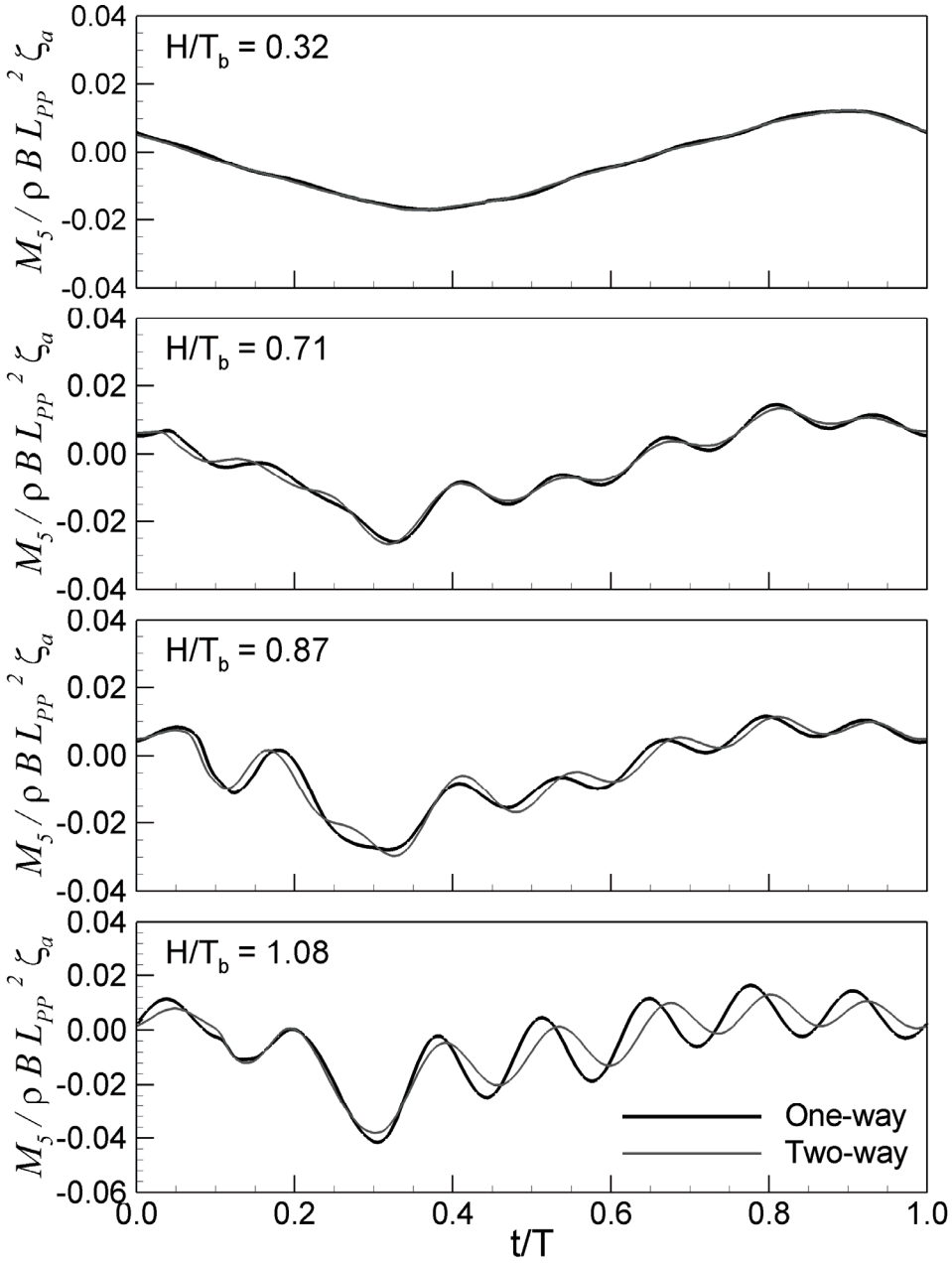

Figure 3.24 Comparison of the dimensionless VBMs at SG2 for the one-way and two-way coupling at various wave heights and $\lambda / L_{PP} = 1.0$

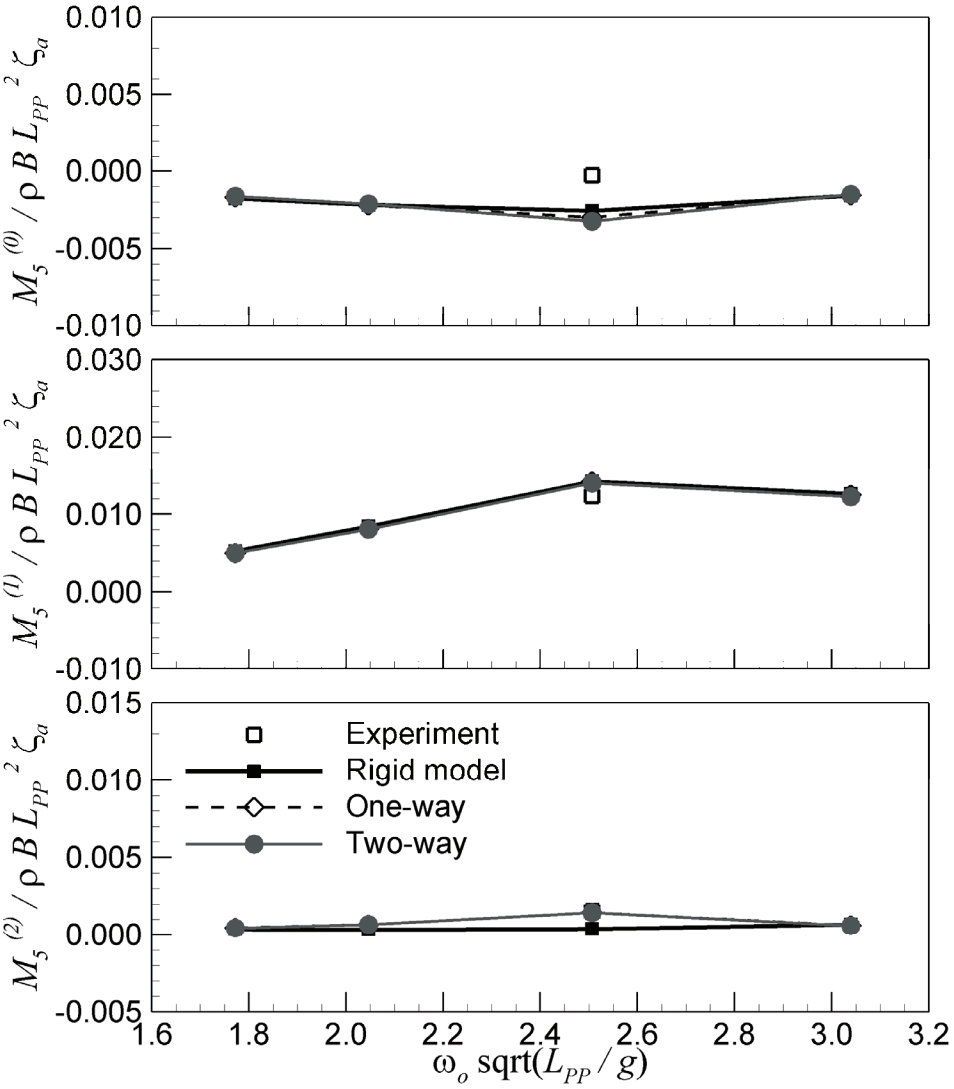

Figure 3.25 Harmonic amplitudes of the VBMs at SG2 for various wave lengths at $H/T_b = 0.71$ (top: zeroth harmonic, center: first harmonic, bottom: second harmonic)

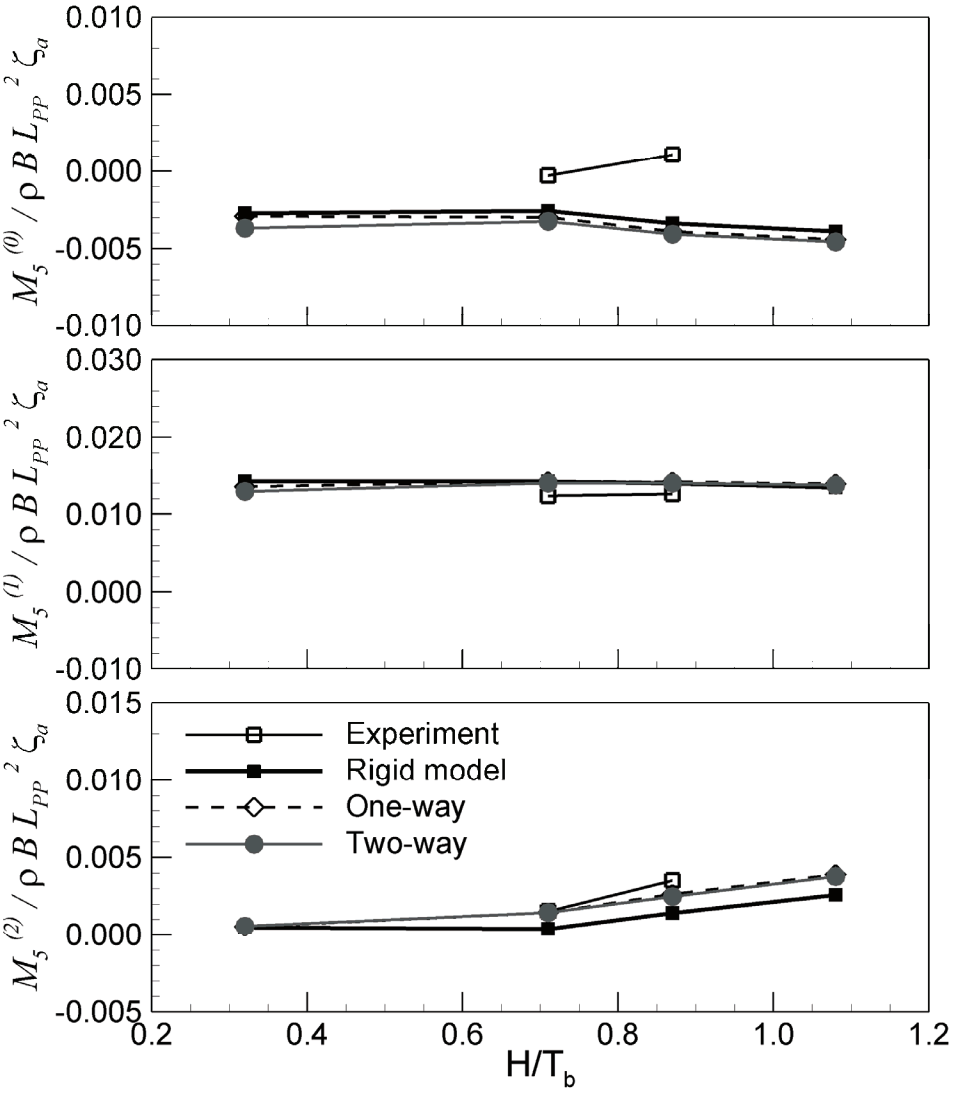

Figure 3.26 Harmonic amplitudes of the VBMs at SG2 for various wave heights at $\lambda / L_{PP} = 1.0$ (top: zeroth harmonic, center: first harmonic, bottom: second harmonic)

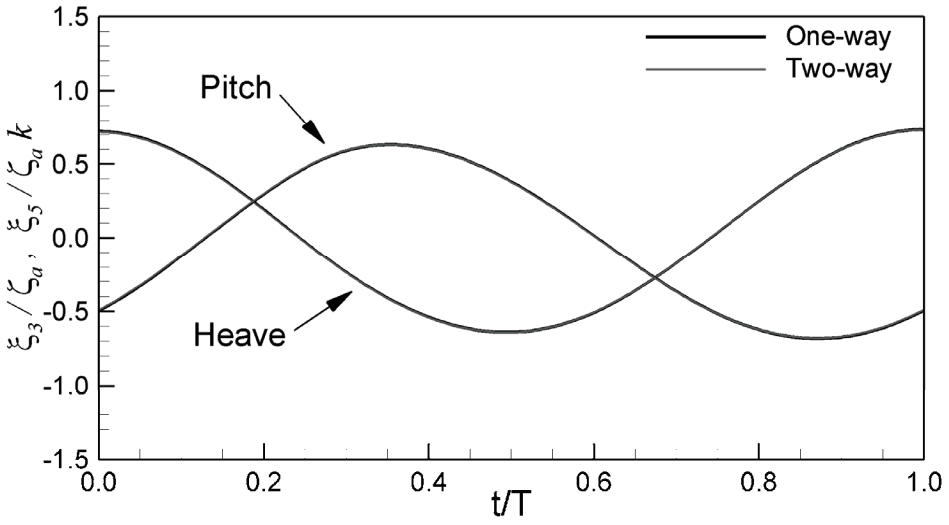

Figure 3.27 Comparison of heave and pitch motions for case 7

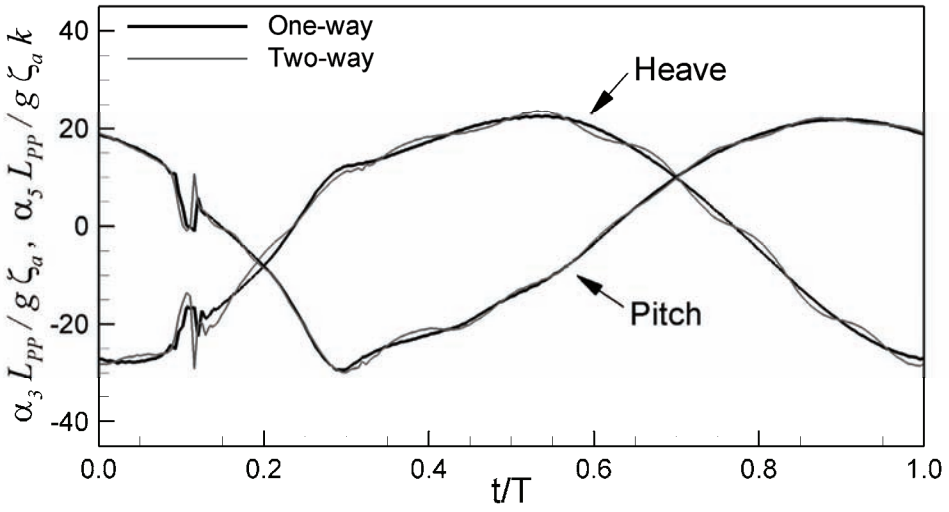

Figure 3.28 Comparison of heave and pitch accelerations for case 7

CHAPTER 4

SLOSHING TANK WITH AN ELASTIC BAR

4.1 Introduction

Sloshing is the dynamic load acting over a tank structure as a result of the fluid motion with free surface confined inside a tank (Delorme et al., 2005). It is an important problem in the design of marine structures such as floating production systems (FPS), floating production storage and offloading (FPSO), and membrane liquefied natural gas (LNG) carrier. FPS and FPSO units are normally subjected to complex waves and currents under varying sea conditions. Consequently, the topside tank performance, especially when partially filled, is adversely affected by liquid sloshing (Lu et al., 2008). LNG carriers usually operate in fully loaded condition or with minimum liquid cargo filling during the ballast voyage. Sloshing loads are of great concern for LNG carriers. The sloshing impact load on the insulation system and the pump tower as well as the hull at low-filling levels has been one of main issues in ship damage history (Shin et al., 2003).

Liquid sloshing has a very significant effect on the dynamics of vessels containing liquids. For instance, an oil tanker traveling in rough seas may suffer from dynamic instabilities due to the coupling of the fluid motion in its internal tanks (Lee et al., 2002). This issue is crucial to understand passive anti-rolling tanks (ARTs), used mainly to dampen roll movements of fishing and container vessels. The fluid in the tank behaves as a resonant fluid system, and this resonant behavior justifies their usage as counter-moment generators for sea waves. Since the reduction of rolling amplitude by sloshing phenomena is the main purpose of ARTs, analysis of the interaction between roll motion and sloshing flow is essential. However, the sloshing loads in the ART have occasionally

caused structure problems; thus methods to mitigate the sloshing loads have been also of great concern in the ship and marine industries.

Sloshing problems have been widely investigated in the last half century (Souto Iglesias et al., 2006). Early stage research was based on mechanical models of the phenomenon by adjusting terms in the harmonic equation of motion. The next stage investigated potential flows using a multimodal analysis of the free surface extended from linear wave theory. Nonlinear shallow water equations were next studied. Recently, the incompressible Navier–Stokes equations were applied to resolve highly nonlinear free surface problems.

Rhee (2005), Lu et al. (2008), and Chen et al. (2009) used RANS to simulate the fluid motion in sloshing tanks. Rhee (2005) and Lu et al. (2008) used a volume of fluid (VOF) formulation to track the free surface in a generic membrane type LNG carrier tank and storage tanks of FPSO, respectively. Chen et al. (2009) used a level set method to capture the free surface and a thin artificial buffer zone to accurately predict the sloshing loads. On the other hand, Souto Iglesias et al. (2004) numerically simulated passive roll-damper tanks for fishing vessels using the SPH. This method was improved to obtain accurate values for the moment amplitude in Souto Iglesias et al. (2006).

Souto Iglesias et al. (2004) used the SPH to demonstrate the sloshing load could be suppressed or mitigated with rigid baffles. Antoci et al. (2007) simulated an elastic gate, interacting with water initially confined in a free surface tank behind the gate, using the SPH. The gate was clamped at its upper end and free at the lower. Idelsohn et al. (2008b) simulated the interaction between an elastic structure and free surface flows in a sloshing tank using the PFEM. Their simulation results were compared with their own experiments. Nevertheless, it is difficult to find literatures on the interaction between elastic structures and free surface flows. Most researches on the FSI problem with the free surface were carried out using particle methods, since those could be relatively easy

to deal with the nonlinear free surface behavior and the interaction between fluid and structure.

In this thesis an URANS solver is used to overcome the limitation of the particle methods, which is unable to resolve boundary layers. The URANS solver, CFDShip-Iowa, is coupled with a nonlinear FEM structure solver to simulate large deformation problems. The developed nonlinear FEM structure solver is validated through comparision with ANSYS results. Non-matching grids between fluid and structure domains are associated using the gluing method. The fluid boundary layer grid deformation is obtained using a linear FEM structure solver for the outer boundary line and a linear interpolation function for the interior grid. Sloshing tanks with an elastic bar are studied and compared with the experimental data and simulation results from Idelsohn et al. (2008b). Before the simulation of sloshing tanks, grid sizes for structure grid are optimized. The effects on the sloshing impact on the tank wall are studied for the the cases without bar, with an elastic bar, and with a rigid bar.

4.2 Simulation Design

4.2.1 Simulation Set-Up

The simulated geometries were two-dimensional rolling tanks with an elastic bar clamped to its bottom or top. The first case was a sloshing tank with an elastic bar clamped on the bottom of tank, which was immersed in sunflower oil. As shown in Fig. 4.1, the height and length of the tank were 344.5 mm and 609.0 mm, respectively. The size of the bar was 57.4 mm long and 4.0 mm wide. In the experiment the thicknesses of the tank and bar were 39.0 mm and 33.2 mm, respectively. There was a gap of 2.9 mm between the tank wall and bar. The material of the bar was a dielectric polyurethane resin. The density and Young's modulus of the bar were 1100 kg/m^3 and 6×10^6 Pa, respectively. The sunflower oil level filled in the tank was matched at the tip of the bar. The oil density and kinematic viscosity were 917 kg/m^3 and 5×10^{-5} m^2/s at 23 °C,

respectively. The variation of the rolling angle for the simulation is shown in Fig. 4.2. The maximum rolling angle of the tank was about 4 degrees. The reference point of rolling motion was the center of the tank bottom.

For the second case, an elastic bar with the length of 114.8 mm was clamped on the bottom of the tank. The sunflower oil was filled to the tip of the bar. The material characteristics of the bar and oil were as same as the first case. The configuration of the sloshing tank is illustrated in Fig. 4.3. The maximum rolling angle was about 4 degrees, but the frequency of the rolling was different from the first case as shown in Fig. 4.4.

The last case had an elastic bar hanging on the top of the tank as shown in Fig. 4.5. The length of the bar was 287.1 mm. The material of the bar was a commercial neoprene rubber with the density of 1900 kg/m^3 and the Young's modulus of 4.0×10^6 Pa. The variation of the rolling angle for this case is shown in Fig. 4.6. The maximum rolling angle was about 2 degrees, but it was asymmetric. The tank was filled with fresh water to the tip of the bar.

4.2.2 Grid System

Overset grids for the fluid solver are shown in Fig. 4.7, which consist of a boundary layer grid and a background grid. The grid sizes used for Case 2 and Case 3 were 156k and 616k grid points for the boundary layer and background, respectively. For Case 1 134k and 531k grid points were used for the boundary layer and background.

The background grid was oscillated around the reference point. The boundary layer grid enclosed the elastic bar and it was deformed with the bar. For the deformation of the boundary layer grid, the linear FEM solver was applied to minimize the deterioration of grid quality. To save computation time, only the outer boundary of the boundary layer grid was solved with a fixed boundary condition on the points where attached on the tank wall and a Dirichlet boundary condition on the bar surface. The deformed outline of the boundary layer gird is shown in Fig. 4.8. The interior grid was

then deformed using a linear interpolation function, which is compared with the initial grid in Fig. 4.9. The orthogonality of the grid was not maintained perfectly, but the deterioration of the grid quality was minimized.

One issue that arose for large deformation was the computation of the overset hole-cutting, which SUGGAR performed as default at the beginning of the computation. Large deformations required reinitialization of the hole-cutting geometry automatically, which needed to be added to SUGGAR. In this thesis the reinitialization was performed at each time step, but not at the inner iterations where the deformation was relatively small. The interpolated and active points of the deformed grid are compared with those of the initial grid in Fig. 4.10.

The bar was assumed as plane stress structure, so the gird for the structure solver was two-dimensional with concentrated point masses at the middle nodes as shown Fig. 4.11. A fictitious structure grid, which was three-dimensional, was used for the association between the fluid and structure grids.

4.3 Results and Discussion

4.3.1 Verification and Validation

Prior to the simulation of a sloshing tank with the free surface, the developed linear and nonlinear structure solvers were validated through ANSYS version 12.0 for Case 3 without fluid. The grid size for ANSYS and CFDShip-Iowa were 289×5 and 300×5, respectively. All simulations in air were performed without elastic damping, and the time step was 0.01 seconds. As shown in Fig. 4.12 both results for the nonlinear solveers showed very good agreement. The linear solvers had small discrepancy because ANSYS and CFDShip-Iowa used the full method and the modal superposition, respectively. The displacements of the linear solvers were 10 times larger than those of the nonlinear solvers, with unrealistic deformation elongating the bar. The pahses were also very different. It showed that the linear solvers were not able to simulate the

problems with geometrical nonlinearity. The displacement is defined here as the horizontal distance of the bar tip from the initial position in the coordinate fixed to the tank. Four different grid sizes were tested for the structure grid as shown in Fig. 4.13. With grid size 200×3, the solution nearly converged. Thus, the 200×3 grid size was used to simulate for Case2 and Case 3, while Case 1 used 100×3 grid size.

4.3.2 Numerical Results of Case 1

Figure 4.14 shows the comparison of the horizontal displacement of the bar tip with experiment and simulation of Idelsohn et al. (2008b). Rayleigh damping coefficients of $\alpha = 0.0$ and $\beta = 0.05$ were applied in the present simulation. The simulation time step was 0.0002 seconds. A large time step would not converge when the deformation was accelerated, since the solution interacting between fluid and structure oscillated in an implicit coupling. The amplitude of the present simulation was larger than the experiment. The phase of the displacement, however, was very similar to the experiment. The maximum displacements at positive and negative directions were almost symmetric in the present simulation, while the maximum displacement at positive direction was larger than the other direction in the experiment and the other simulation even though the rolling angle was symmetric. The spectral analyses for the horizontal displacements at the bar tip are compared in Fig. 4.15. The frequencies of the first peak were observed at 0.6 Hz for all results, but the amplitude of the present simulation was about 60% larger than the experiment. The second peak at 1.8 Hz was observed in the present simulation, which was caused by the wiggly shape in the second period of the displacement. The displacements of the bar without/with interaction with fluid are compared in Fig. 4.16. The displacement increased about 100 times due to the fluid forces, with a phase lag.

The deformation of bar and the elevation of free surface are compared with the experiment at 0.62, 0.95, 1.35, 1.62, and 1.88 seconds in Fig. 4.17. Pressure contours and velocity vectors are also included the figure. The simulation results at 1.62 and 1.88

seconds had rough free surface, while the experiment had smooth free surface. A possible reason was that surface tension was not implemented in the present simulation even though that of sunflower oil must be much larger than fresh water. The present simulation showed that when the rolling angle increased the fluid overflowed and a bubble cavity was observed near the bar tip. The velocity of the overflow was much faster than other fluid flow, resulting in strong vorticity. These phenomena can be more clearly observed in Fig. 4.18 which shows the sequential vorticity contours from 2.10 to 3.20 seconds. Due to the velocity difference between inside and outside of the overflow a vortex pair was created at the position where the overflow attached on the free surface as shown at 2.30 seconds. The bubble cavity disappeared through the free surface increasing when the rolling angle changed to the opposite direction. The vortex pair travelled and diminished near the bar, and then merged to a new vortex pair.

4.3.3 Numerical Results of Case 2

The horizontal displacement of the tip is compared with the experimental and simulation results (2008b) in Fig. 4.19. The time step in the present simulation was 0.0002 seconds, and Rayleigh damping coefficients of $\alpha = 0.0$ and $\beta = 0.025$ were applied. The present simulation showed good agreement with the experiment, while the amplitude and phase were slightly different. The displacement amplitude of the present simulation increased with time, whereas that of the experiment did not change after 2.5 seconds.

The first peaks of the spectral analyses for the horizontal displacements were observed at 0.8 Hz for the experiment and simulations as shown in Fig. 4.20. The amplitudes of the first peak were 0.064 m, 0.079 m, and 0.074 m for the experiment, the simulation of Idelsohn et al. (2008b), and the present simulation, respectively.

Figure 4.21 compares the tip displacement of the dry bar to the result with fluid. The phases of both results were exactly same, but the peak time was delayed due to the

interaction with the fluid. The amplitude of the simulation without fluid was 0.0027 m at 0.8 Hz showing huge difference from the simulation with fluid. The maximum vertical displacement of the bar with fluid was about 0.05 m as shown in Fig. 4.22. It showed small hysteresis around maximum displacement position.

The bar deformation and free surface elevation are compared for one period in Fig. 4.23. The displacement of the bar and the free surface elevation were in good agreement with the experiment. As mentioned in Case 1, however, the present simulation had rough free surface in all time steps as compared with the experiment due to the effect of surface tension. The difference of the bar displacements was clear when the bar passed zero displacement position as shown at 2.23 and 2.83 seconds. The velocity of the fluid was maximized due to the channel effect when the fluid passed over the bar. Then it made a strong vortex pair between the bar tip and the free surface. The vorticity generated on the free surface created a secondary wave on the free surface as shown at 2.09 and 2.83 seconds. This can be clearly observed from the vorticity contours shown in Fig. 4.24. The secondary waves at 2.70 and 3.20 seconds were produced by the vorticity generated on the free surface at 2.60 and 3.10 seconds, respectively. As the vorticity generated in one side passed to the other side when the bar started to restore from maximum displacement, the vorticity structure became more complex.

4.3.4 Numerical Results of Case 3

The horizontal displacements at the middle and tip of the bar for Case 3 are compared with experiments and simulations, carried out by Idelsohn et al. (2008b), in Fig. 4.25 and 4.26. The time step in the present simulation varied automatically between 0.00045 seconds and 0.00035 seconds according to the convergency of the implicit interaction between fluid and structure. Rayleigh damping coefficients were $\alpha = 0.0$ and $\beta = 0.025$.

In this simulation the impacts of free surface at the bar occurred at 1.95, 2.80, 3.64, 4.48, and 5.33 seconds, while the impacts were observed at 1.95, 2.74, 3.63, 4.46, and 5.29 seconds in the experiment. The interval time of impact moments in the present simulation was fairly constant at about 0.85 seconds, but that in the experiment varied from 0.79 to 0.89 seconds. The peaks at the middle of the bar showed a time lag of about 0.05 seconds in this simulation. On the other hand, in the experiment the peaks at the middle of bar were almost coincident with the peaks at the tip. The peak at 3.62 seconds was larger than that at 4.32 seconds for the middle of the bar and vice versa for the tip of the bar, while the peak at 3.69 seconds was smaller than that at 4.32 seconds for the middle of the bar showing a constant trend with the tip of the bar. It was suspected from these results that the elastic bar in the experiment might be stiffer than in the present simulation. Nevertheless, the displacements in this simulation tended to confirm trends in the experiment even though the amplitude of displacement was larger than the experiment. This was true at 3.0 seconds, the first large deformation due to strong free surface impact. As a consequence, the peaks in this simulation at 3.46 and 3.64 seconds were much lower than in the experiment.

Comparisons of the spectral analysis for the displacements are illustrated in Fig. 4.27 and 4.28 for the middle and tip of the bar, respectively. Dominant peaks for the tip of the bar were observed at 0.67, 1.00, 1.33, 1.82, and 2.99 Hz in both the present simulation and experiment. On the other hand, the second and third dominant peaks were at 1.34 Hz and 1.82 Hz in the simulation of Idelsohn et al. (2008b). The dominant peaks for the middle of the bar in the present simulation had only 0.01 Hz difference from those for the tip, and showed all the peaks presented in the experiment. However, the first peaks of the middle and tip of the bar in the present simulation were larger than the experiment, with the bigger difference at the tip. The first peak at 0.67 Hz was strongly related to the rolling motion of the tank because a peak at the same frequency was also observed through the spectral analysis of the displacement for the tip in air as shown in

Fig. 4.30. The second peak at 1.17 Hz in the dry case was not observed in the case with fluid because the decelerating and accelerating moments of the tip around zero displacement in air changed dramatically due to free-surface impact. Instead, the second and third peaks were observed at 1.00 and 1.33 Hz in the case with fluid. As shown in Fig. 4.29 the impact events due to the free surface occurred twice in one oscillation period. The impacts were observed, for instance, at 3.64 and 4.48 seconds during the third period of the tip displacement in the case with fluid. The impact occurred while the tip was restoring to zero displacement and pushed the bar against its direction of motion. The second positive large displacement occurred at 4.69 seconds. This was smaller than the first peak at 3.00 seconds, since the restoring acceleration before the impact at 4.48 seconds was larger than at 2.80 seconds. Figure 4.31 compares the horizontal displacement at the tip of the bar versus the rolling angle of the sloshing tank. This more clearly illustrates the second and third peaks. The impact events occurred when the rolling angle was approximately ±1 degrees.

The hysteresis of the displacement at the tip of the bar is shown in Fig. 4.32. The displacement increased due to the impact and inertia forces, while only the inertia forces enforced the displacement to decrease. This was why the vertical displacement during the increase of the displacement was larger than that during the decrease.

The deformation of bar and the elevation of free surface are compared with the experiment at fifteen sequential times in Fig. 4.33. Pressure contours and velocity vectors in the water region are also shown in the figure. This simulation agreed well with the experiment in the deformation and the free-surface elevation except for some points. The numerical simulation showed larger deformation at 2.69, 2.82, 3.02, 3.55, 3.69, and 4.42 seconds, and wave propagation in the simulation was slightly faster than in the experiment at 2.69, 3.69, and 3.89 seconds.

Vorticity contours from 4.40 seconds to 5.50 seconds with 0.10 seconds interval are shown in Fig. 4.34. A strong vortex pair was created while the free surface was

detaching from the bar, as shown at 4.70 and 5.50 seconds. Another vortex pair was generated near the wall while the free surface level was decreasing after the impact on the wall. The vortex pair was traveling up and down until it dissipated, as shown at 5.10 to 5.50 seconds.

The sequential contours of von Mises stress in the bar are shown in Fig. 4.35. The maximum stress was 22.3 kPa at 4.60 seconds, right after the water impact on the bar, which was observed around the middle of the bar. The maximum stresses at the top of the bar were 46.7 kPa and 44.5 kPa at 4.70 and 4.80 seconds, respectively. The stress at the top of the bar varied from 8.9 kPa to 46.7 kPa.

4.3.5 Study on sloshing impact on the wall

The time histories of the dynamic pressure at P1 and P2 illustrated in Fig. 4.5 are compared for the cases without the bar or with different bar material properties from Case 3 – without bar, with an elastic bar, and with a rigid bar – in Fig. 4.36 and 4.37, respectively. The impact pressures were observed around 3.2 and 4.9 seconds for both P1 and P2. There was no difference on the dynamic pressure at the first peak around 1.7 seconds. The peaks at P2 were sharper and larger than those at P1, but the duration periods of pressure fluctuation were shorter.

The second and third peaks at P1 are zoomed in Fig 4.38 and 4.39, respectively. The maximum amplitudes at P1 and P2 decreased with a bar showing smallest peaks in the case of a rigid bar. A phase lag developed, with the third peak showing larger phase lag than the second peak. The trends of the second and third peaks for amplitude and phase at P2 were very similar to P1, as shown in Fig. 4.40 and 4.41. For the case without bar, the third peak amplitude was larger than the second peak amplitude at P2, while they were similar at P1. The maximum impact pressure of the case with a rigid bar decreased up to 60% at the third peak as compared with the case without bar.

Spectral analyses of the dynamic pressure histories at P1 and P2 are shown in Fig. 4.42 and 4.43. The effect of the rigid bar on reducing the dynamic pressure increased at high frequency region. It might be useful to decrease the vibration induced by sloshing event in a liquid cargo tank.

4.4 Conclusions

A nonlinear FEM structure solver for large deformation FSI problems was developed and validated with ANSYS. For the deformable boundary layer grid in the fluid domain a linear FEM solver was applied to deform the outer line of the boundary layer grid to minimize the deterioration of grid quality. Then the interior grid was deformed using a linear interpolation function. The structure solver was coupled with a RANS solver.

As application examples three sloshing tanks with an elastic bar clamped to its bottom or top were simulated and compared with the experiments and other numerical simulation results using the PFEM. Even though the present simulations had slightly larger amplitudes than the experiments for all cases, they showed good agreement with the experiments in the bar deformation as well as the free surface elevation. The present simulations for Case 1 and Case 2 had rough free surface because they might not consider surface tension. The spectral analyses of the present simulation results agreed well with the experimental results, showing much better performance than computations with the PFEM, especially for Case 3. The vorticity behavior due to the interaction with fluid was studied to understand the flow structure. The vorticity generated from the free surface created a secondary wave. The tip displacements of the bars were compared with those in the dry cases to investigate the effect of fluid forces. The displacement for Case 1 increased about 100 times. The maximum von Mises stress was 46.7 kPa at the top of the bar for Case 3. The stress on the middle of the bar increased to 22.3 kPa after the moment of water impact on the bar.

The effect of the bars on reducing the dynamic impact pressure acting on the tank wall was studied through the cases without bar, with an elastic bar, and a rigid bar on the top. The rigid bar was more effective than the elastic bar. It showed the possibility to reduce the vibration induced by the sloshing through decreasing the dynamic pressure at high frequency regions. The effect of the bar on the sloshing impact, however, should be validated in three-dimensional tank, and the geometry and rigidity of the bar should be also studied to maximize the effect.

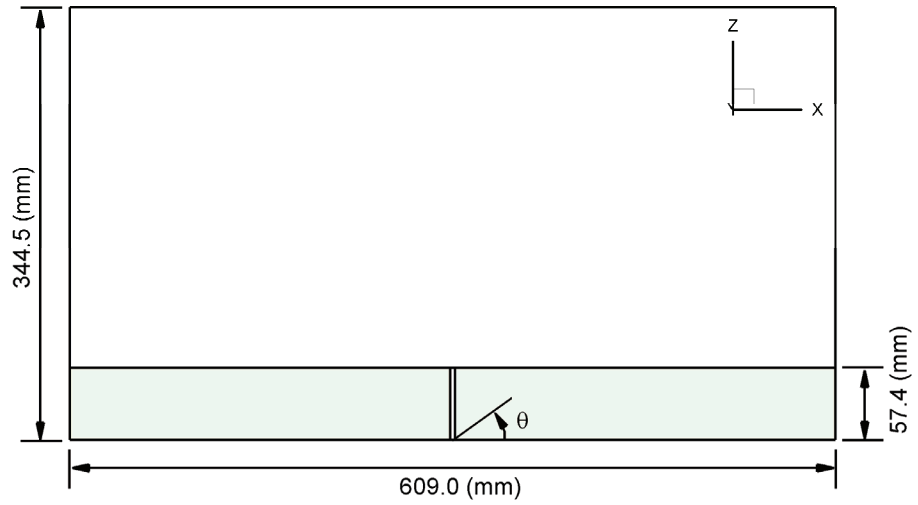

Figure 4.1 Sloshing tank with an elastic bar clamped on the bottom in shallow sunflower oil (Case 1)

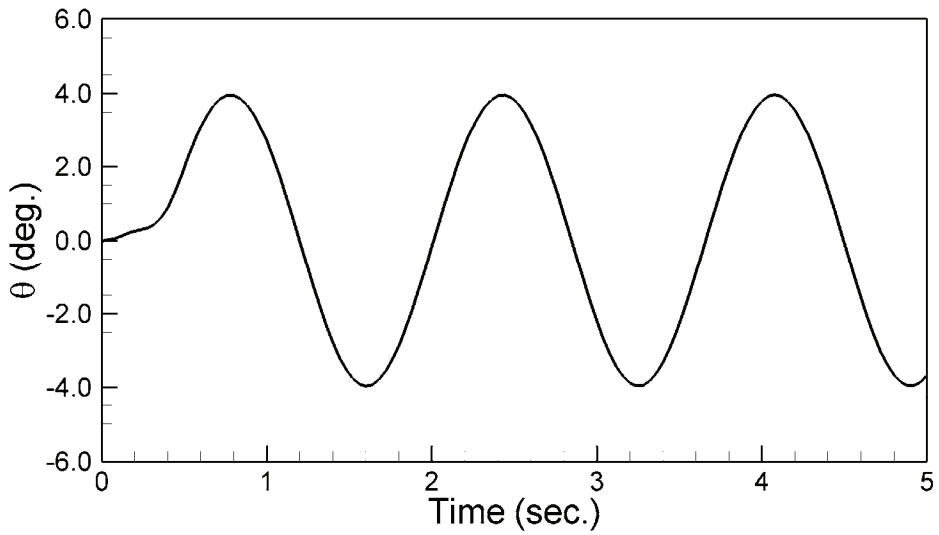

Figure 4.2 Variation of the tank rolling angle for Case 1

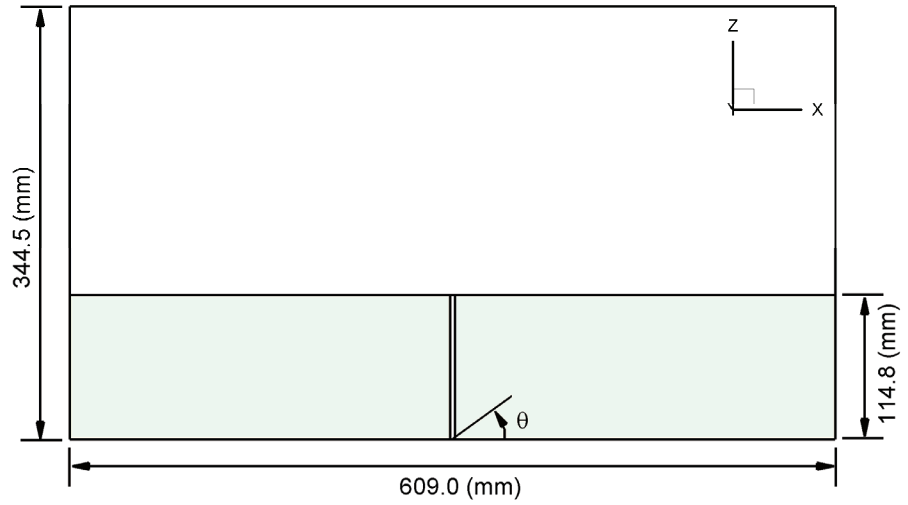

Figure 4.3 Sloshing tank with an elastic bar clamped on the bottom in deep sunflower oil (Case 2)

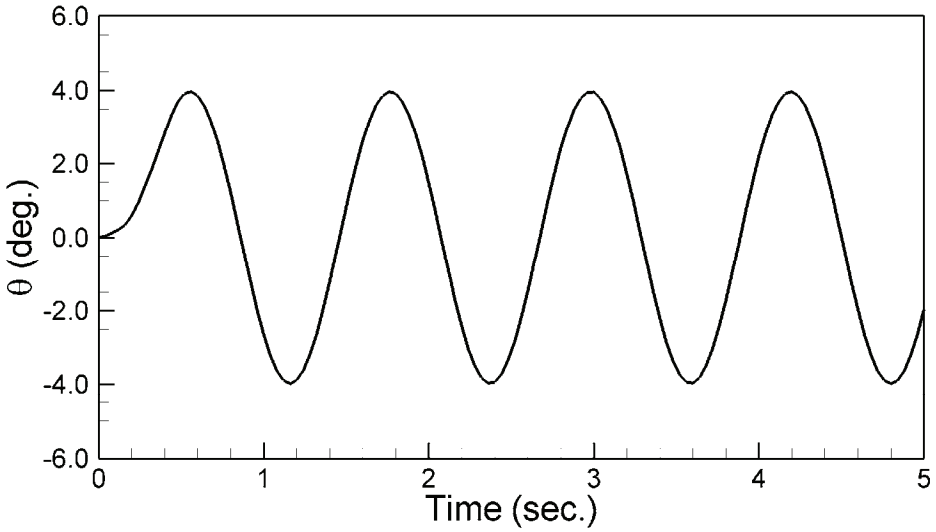

Figure 4.4 Variation of the tank rolling angle for Case 2

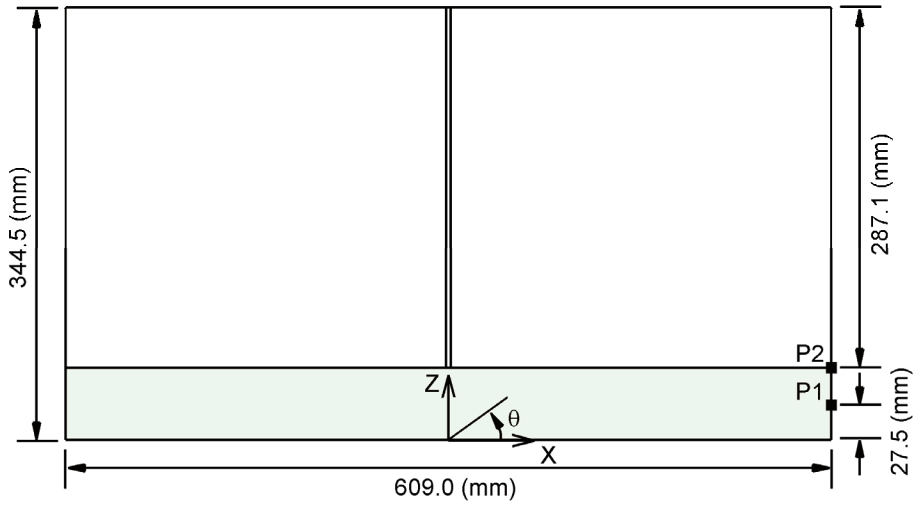

Figure 4.5 Sloshing tank with an elastic bar clamped at the top above shallow fresh water (Case 3)

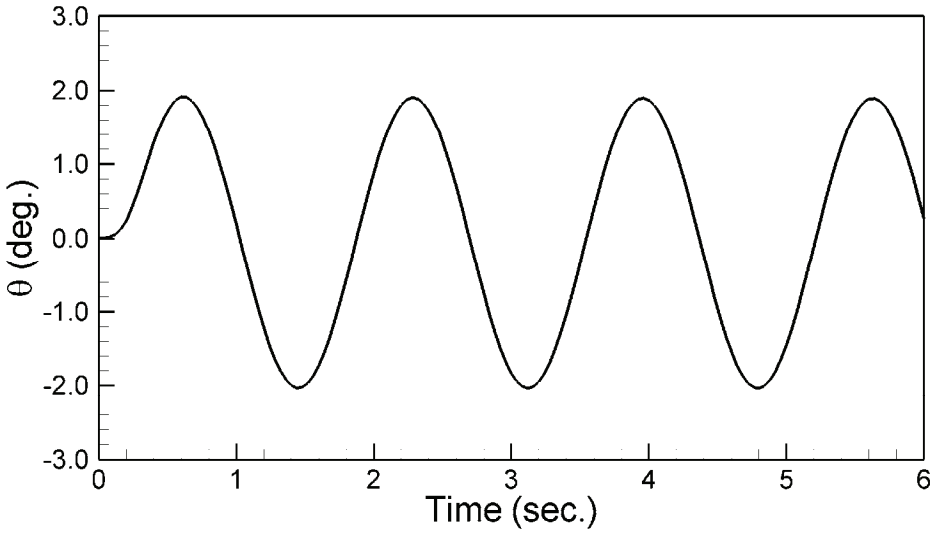

Figure 4.6 Variation of the tank rolling angle for Case 3

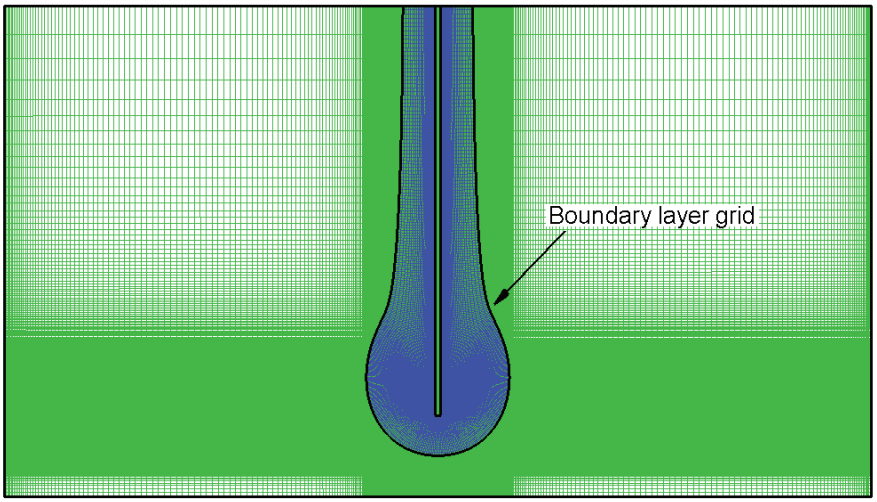

Figure 4.7 Overset grids of the fluid domain for Case 3

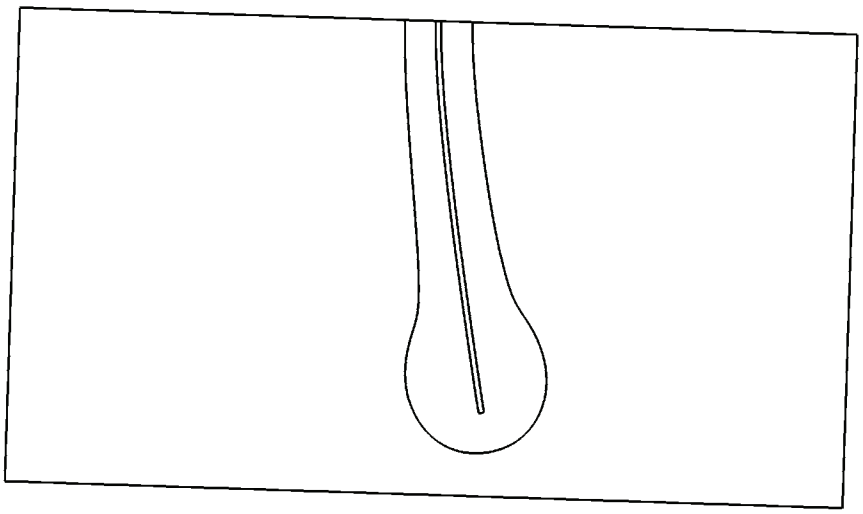

Figure 4.8 Deformation of the fluid boundary layer grid outline for Case 3

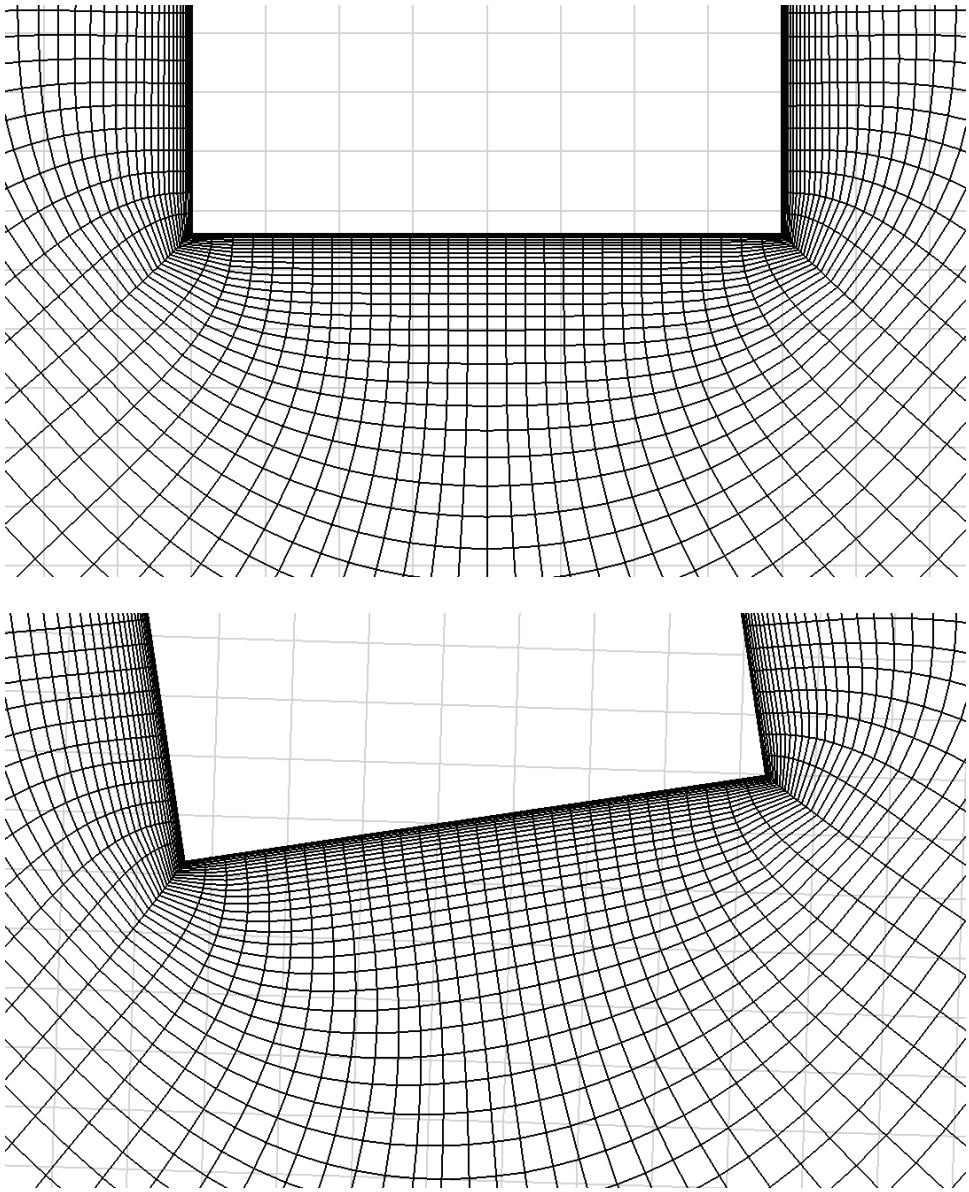

Figure 4.9 Interior grid near the bar surface of the fluid boundary layer gird for Case 3: initial grid (top) and deformed grid (bottom)

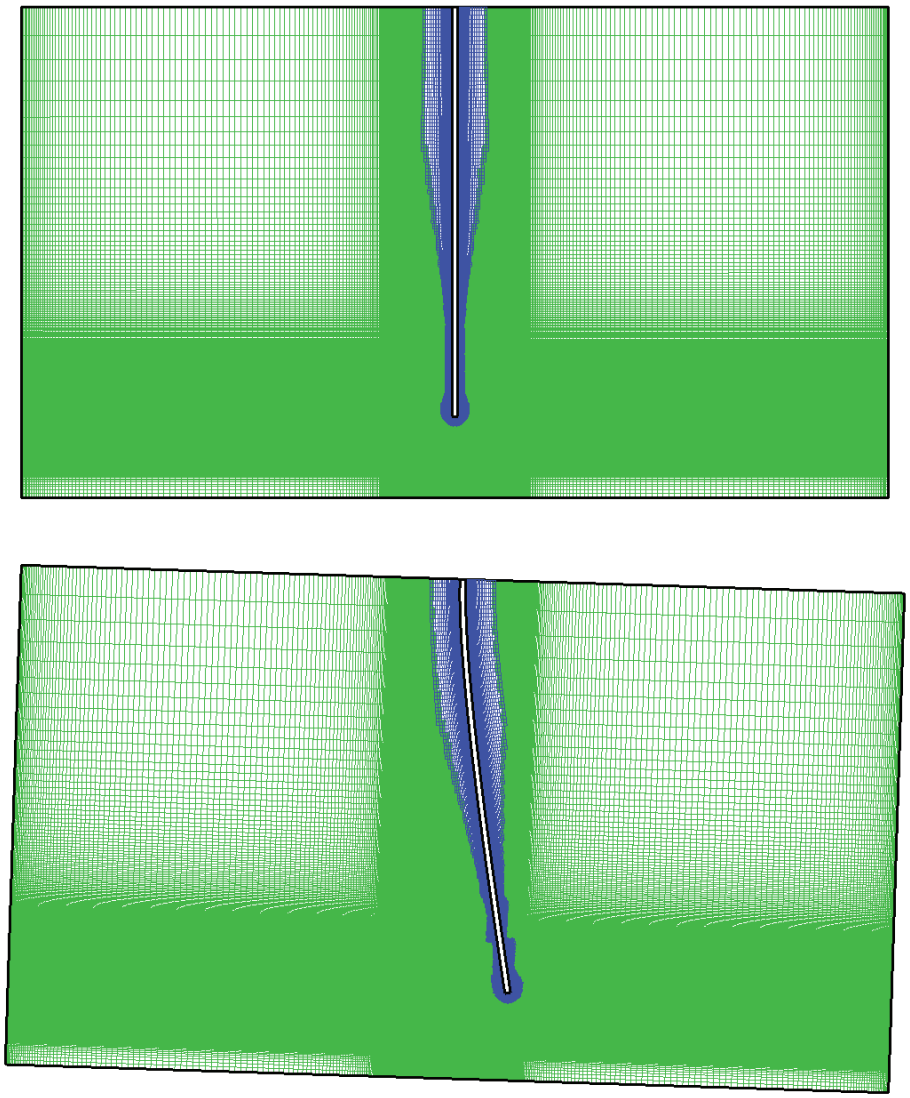

Figure 4.10 Overset grid arrangement of interpolated and active points for Case 3: initial grid (top) and deformed grid (bottom)

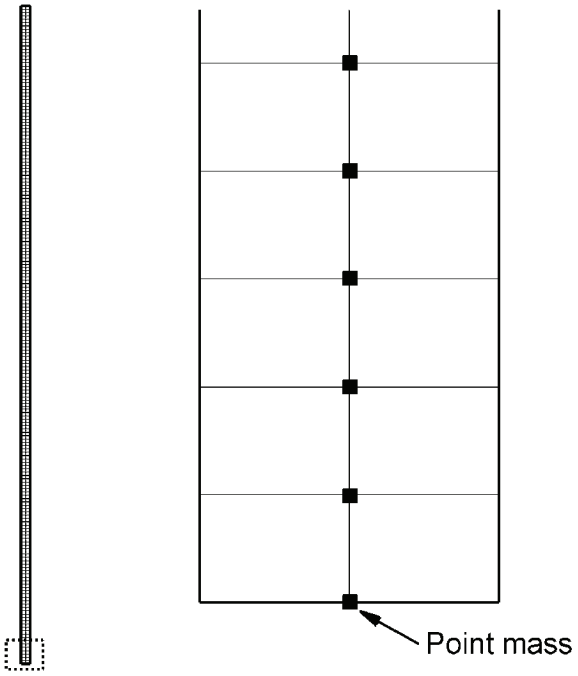

Figure 4.11 Structure grid and concentrated point masses for the elastic bar

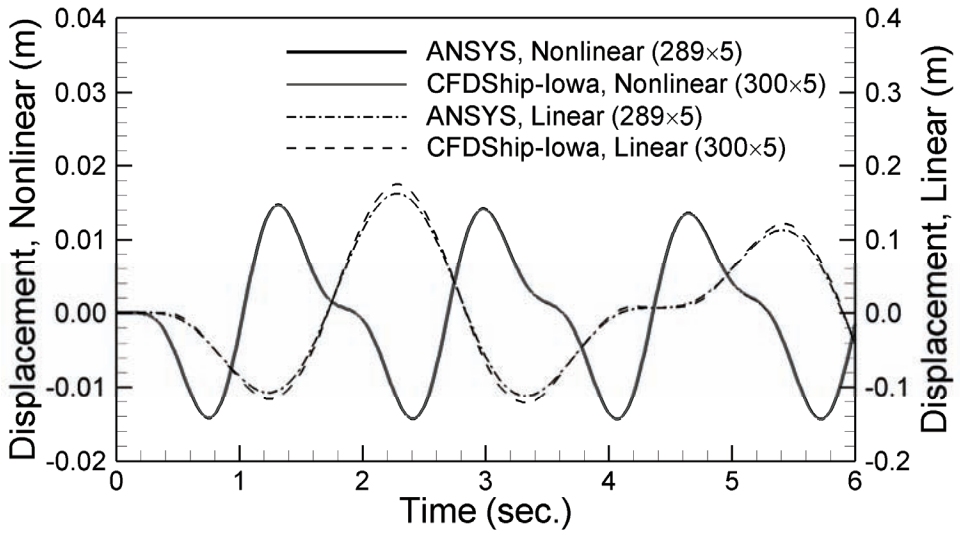

Figure 4.12 Comparison of the displacements at the bar tip using CFDShip-Iowa and ANSYS for the dry condition of Case 3

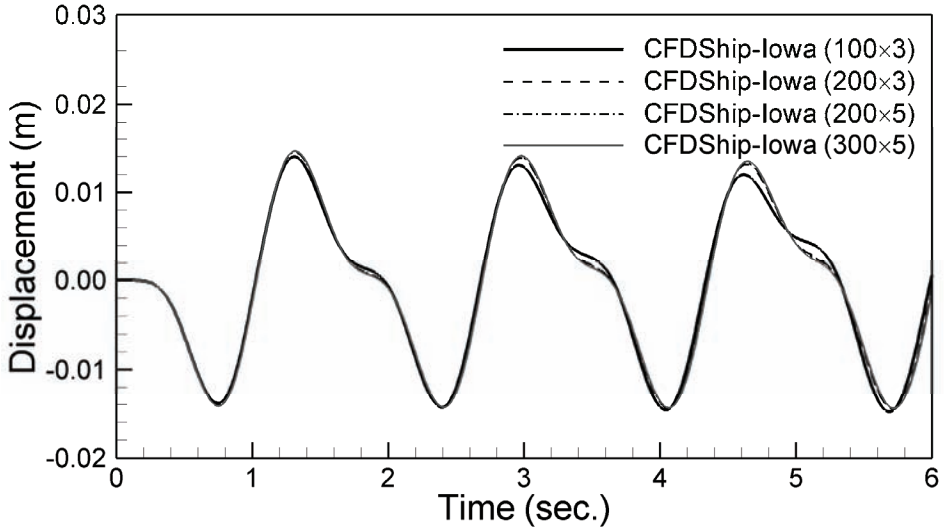

Figure 4.13 Grid size test of the structure grid for the dry condition of Case 3

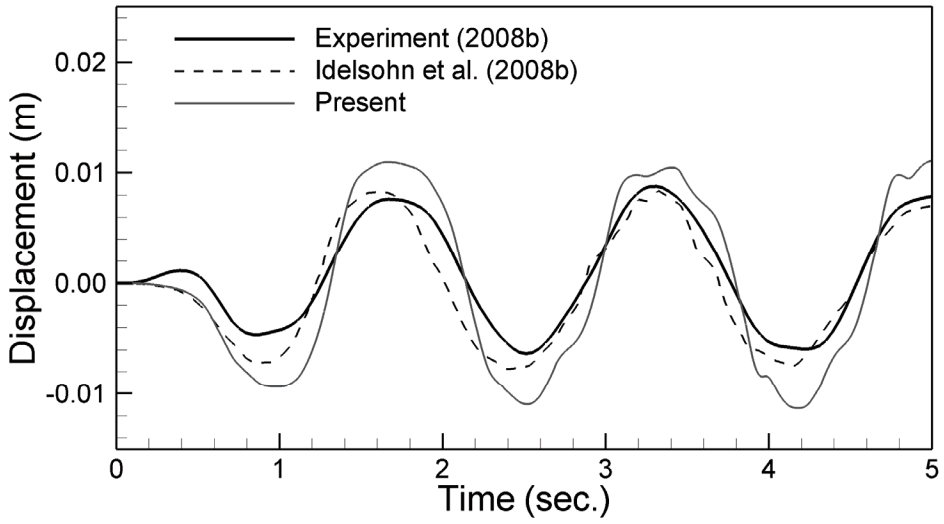

Figure 4.14 Comparison of the horizontal displacements at the bar tip for Case 1

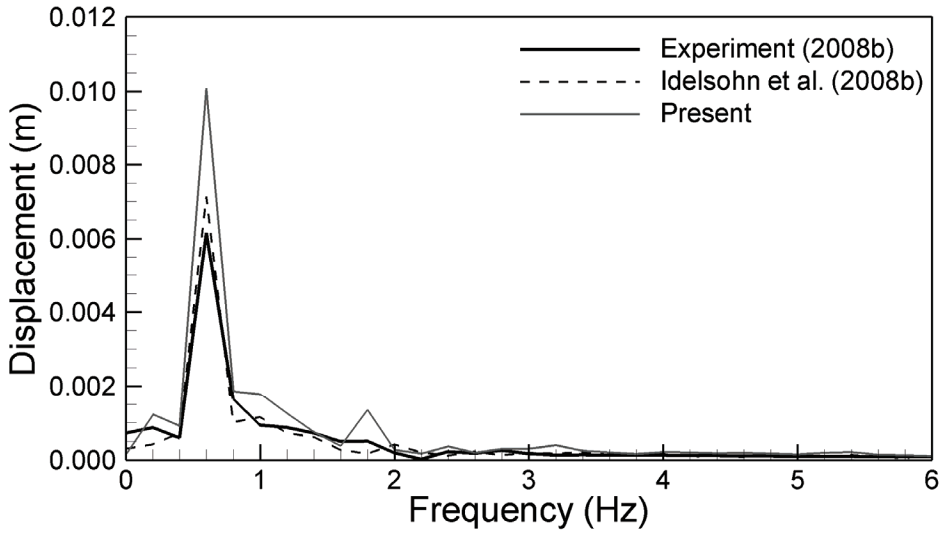

Figure 4.15 Comparison of the spectral analyses for the horizontal displacements at the bar tip for Case 1

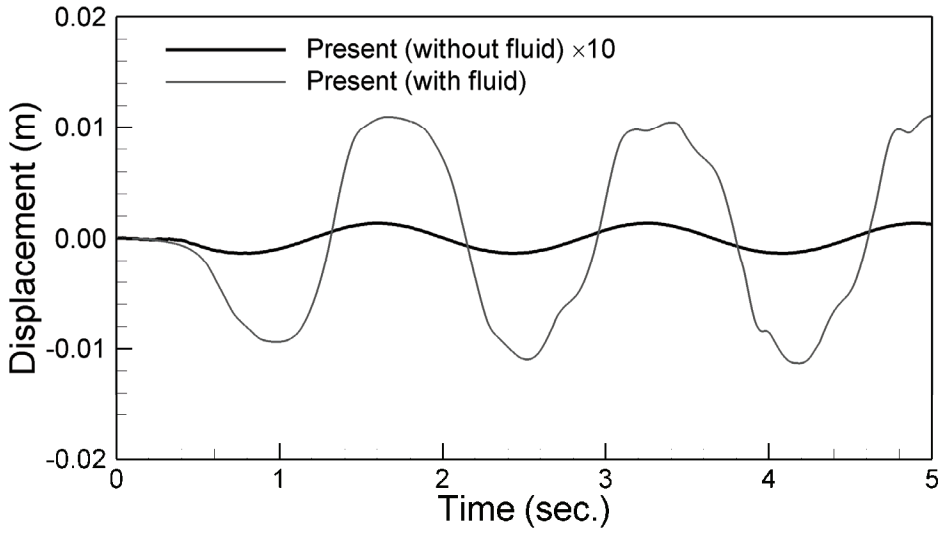

Figure 4.16 Comparison of the horizontal displacements at the bar tip in the cases with and without fluid for Case 1

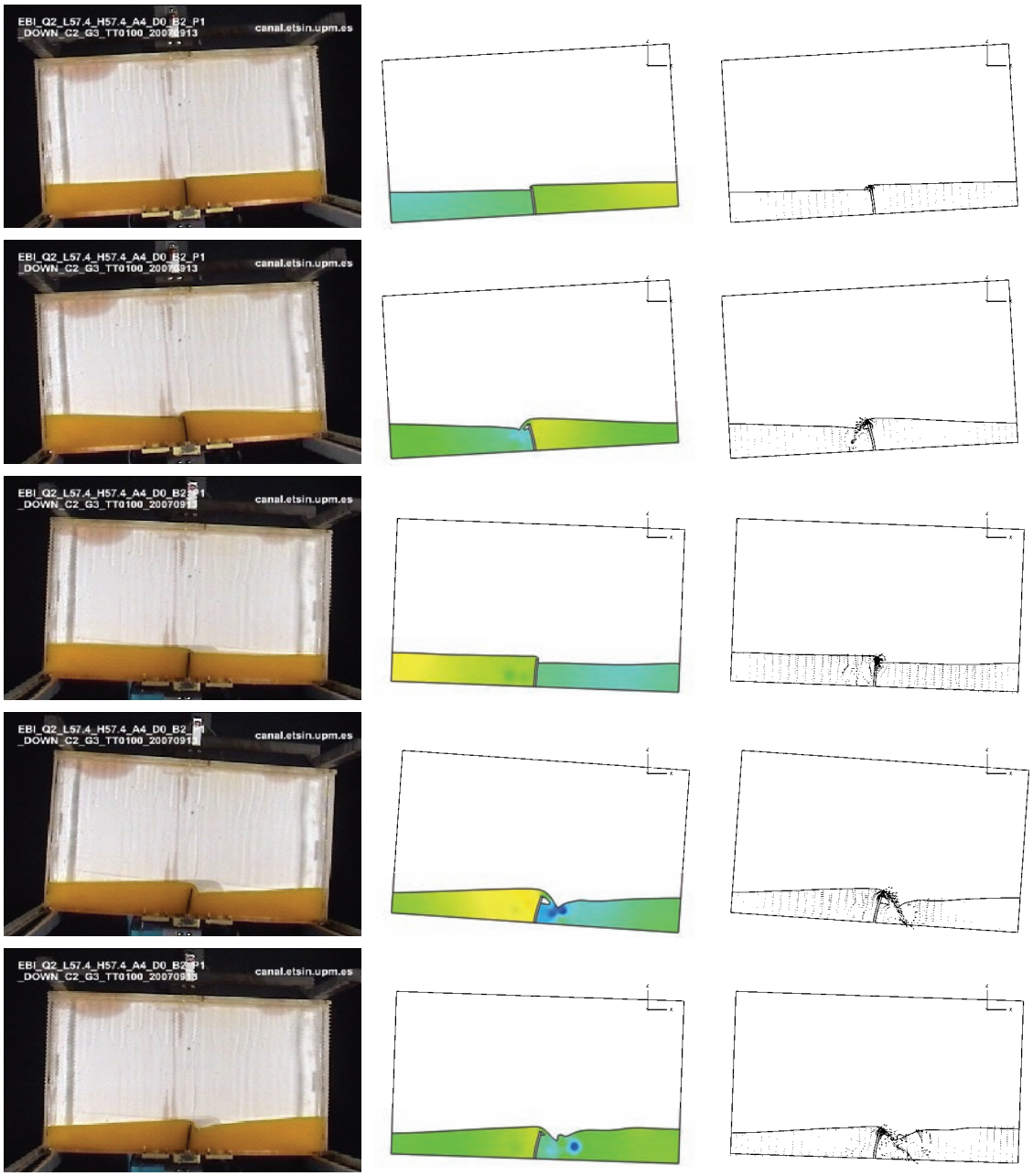

Figure 4.17 Comparison of the deformation of bar and the elevation of free surface vs. experiment (left) for Case 1: pressure contours (middle) and velocity vectors (right) at t=0.62, 0.95, 1.35, 1.62, and 1.88 seconds

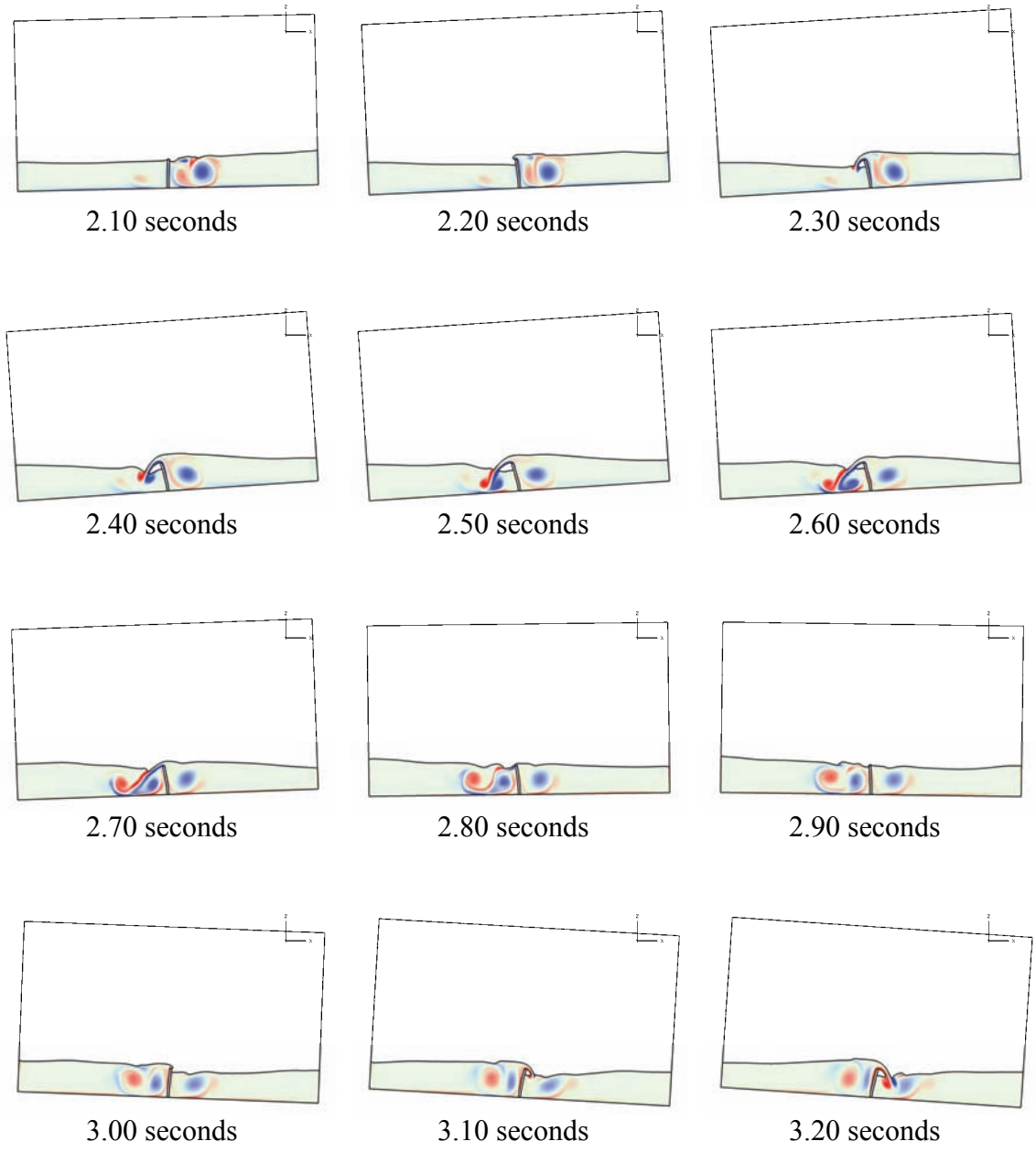

Figure 4.18 Sequential vorticity contours for Case 1

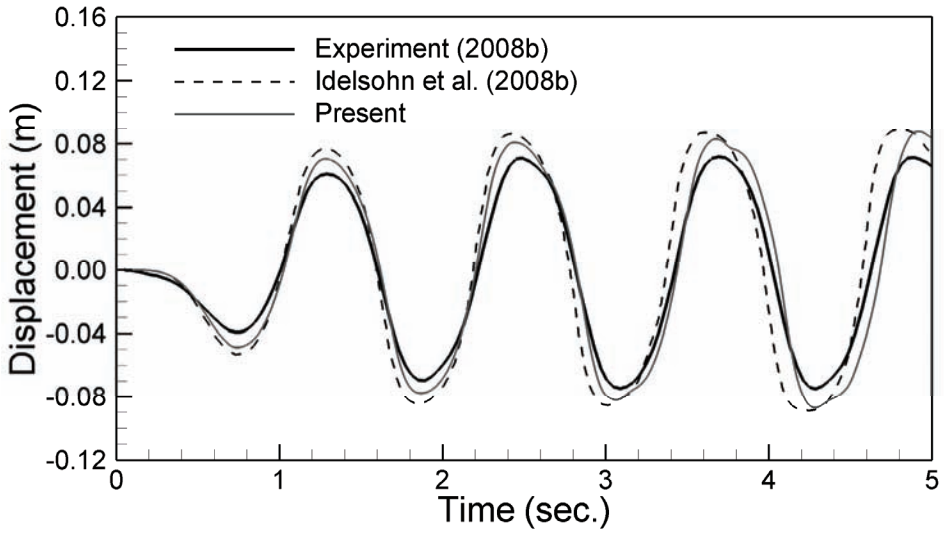

Figure 4.19 Comparison of the horizontal displacements at the bar tip for Case 2

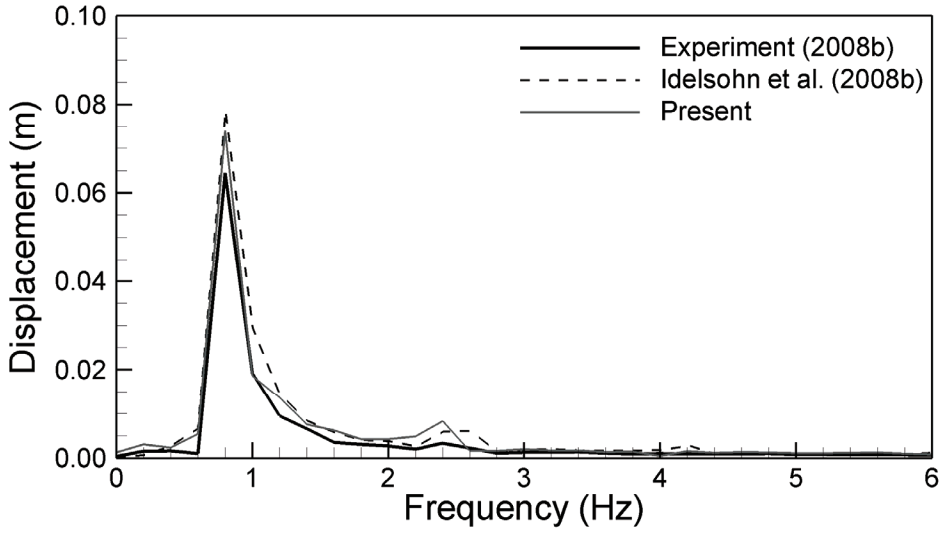

Figure 4.20 Comparison of the spectral analyses for the horizontal displacements at the bar tip for Case 2

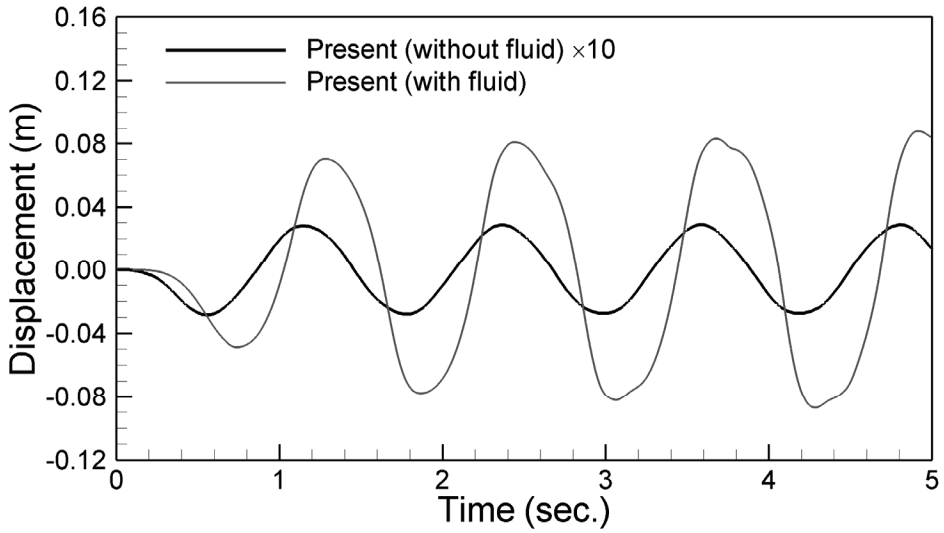

Figure 4.21 Comparison of the horizontal displacements at the bar tip in the cases with and without fluid for Case 2

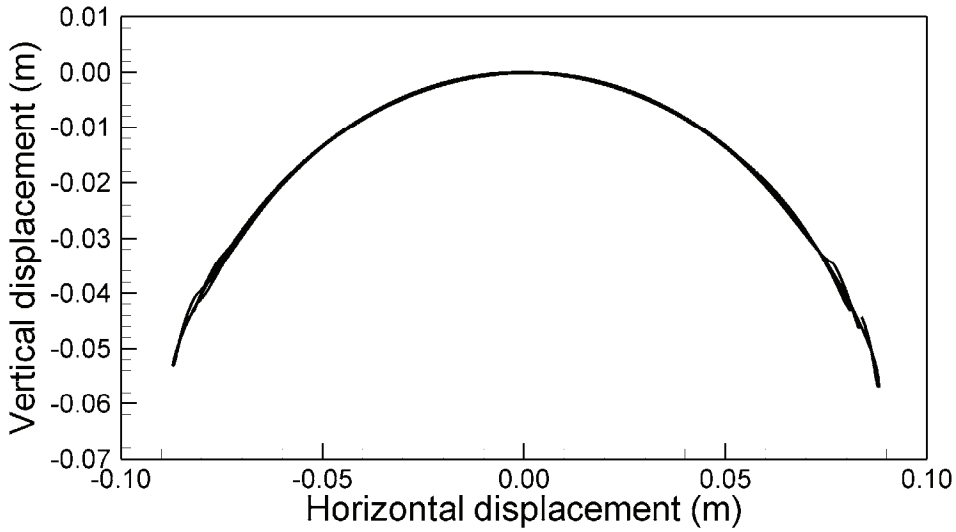

Figure 4.22 Trajectory of the bar tip displacement for Case 2

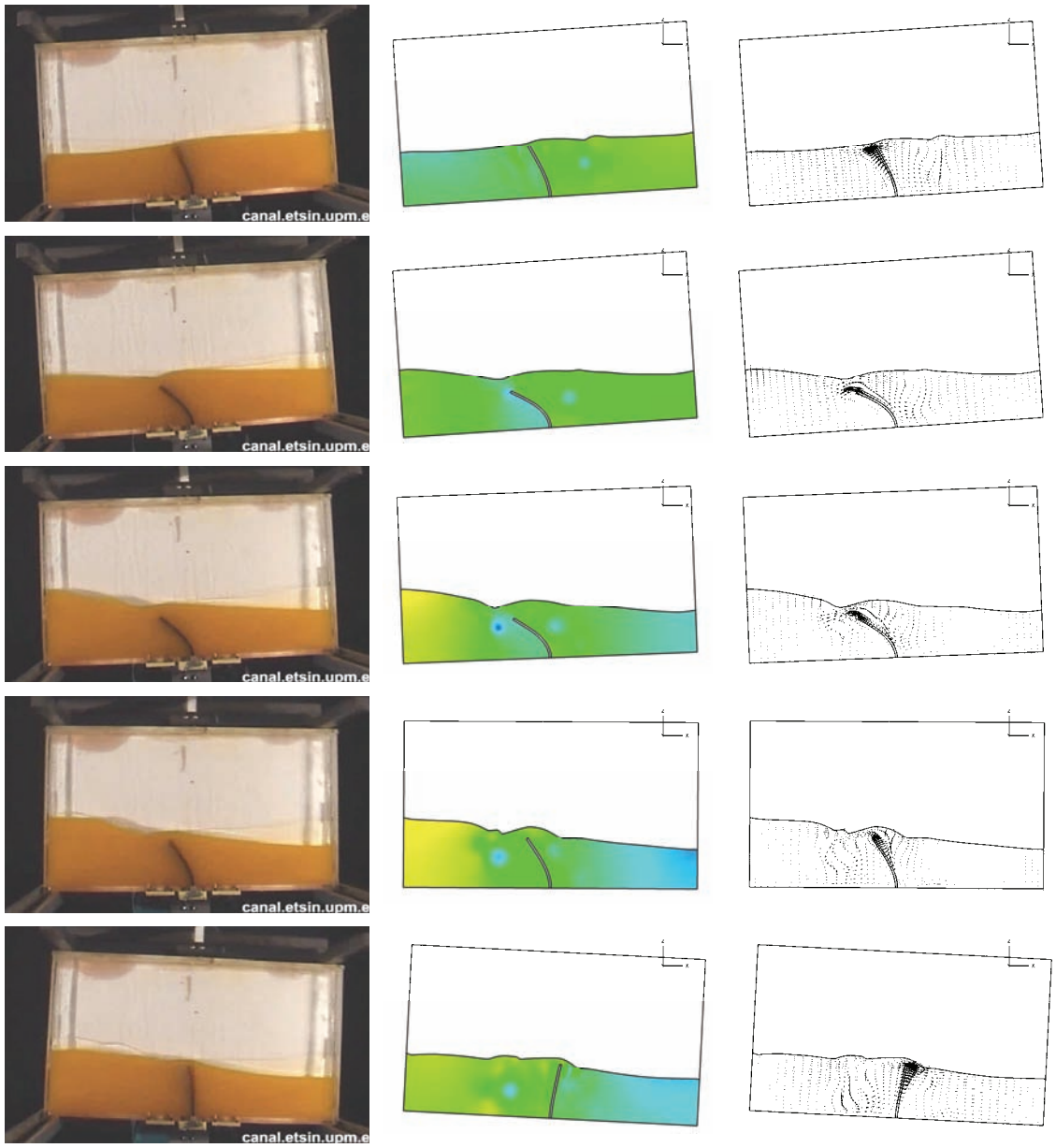

Figure 4.23 Comparison of the deformation of bar and the elevation of free surface vs. experiment (left) for Case 2: pressure contours (middle) and velocity vectors (right) at t=1.69, 1.83, 1.96, 2.09, 2.23, 2.36, 2.56, 2.69, 2.83, and 2.96 seconds

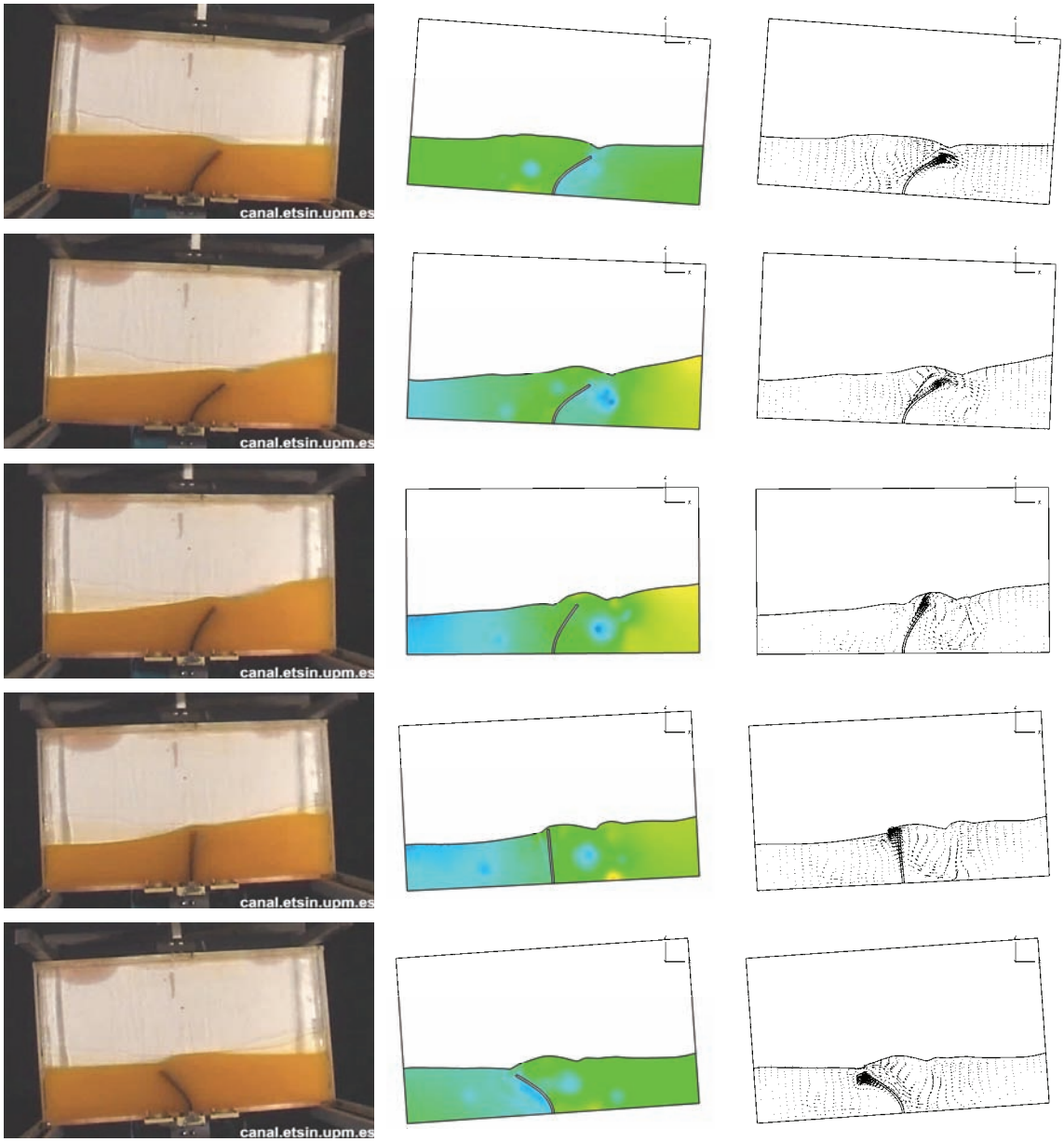

Figure 4.23 Continued

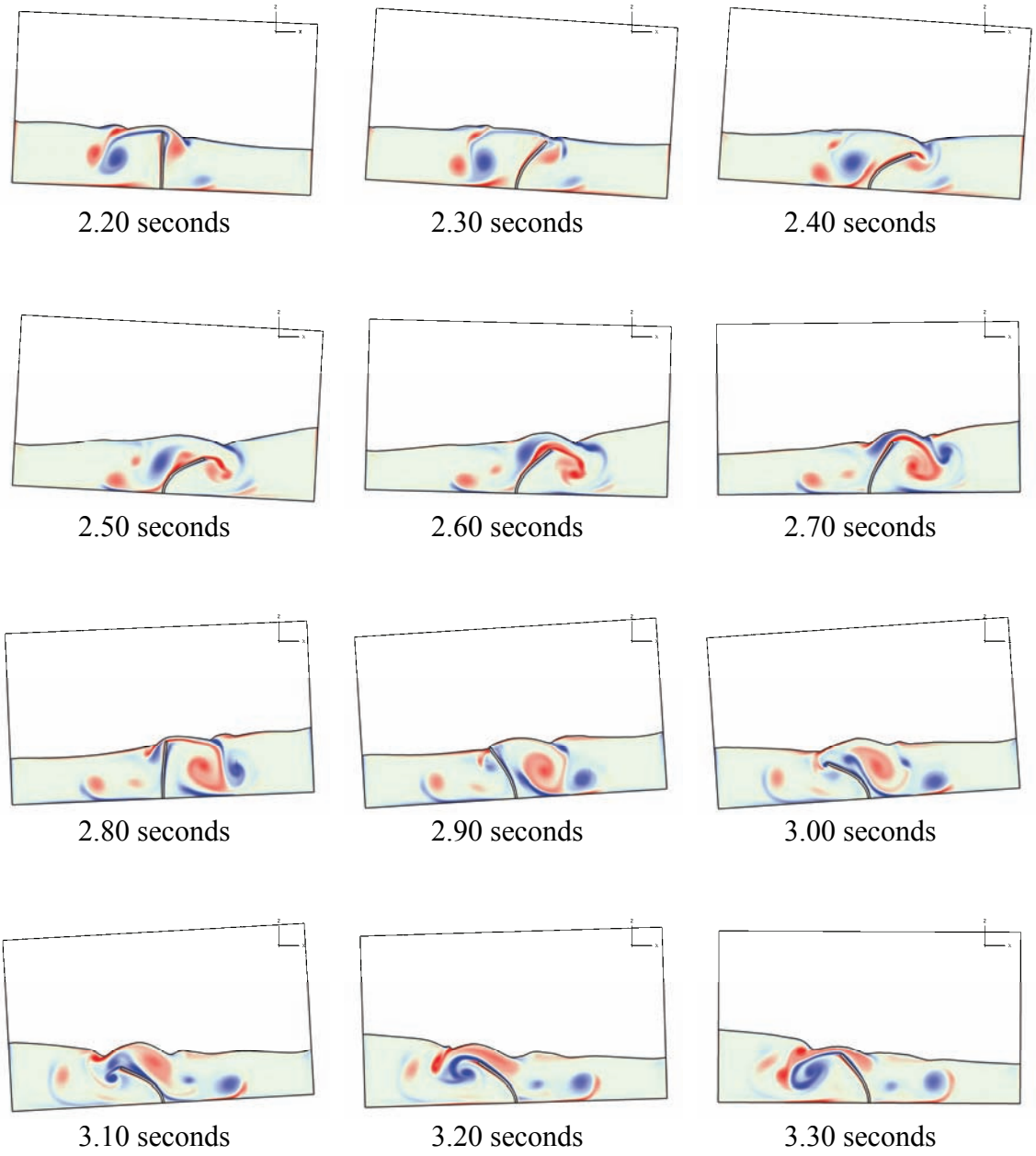

Figure 4.24 Sequential vorticity contours for Case 2

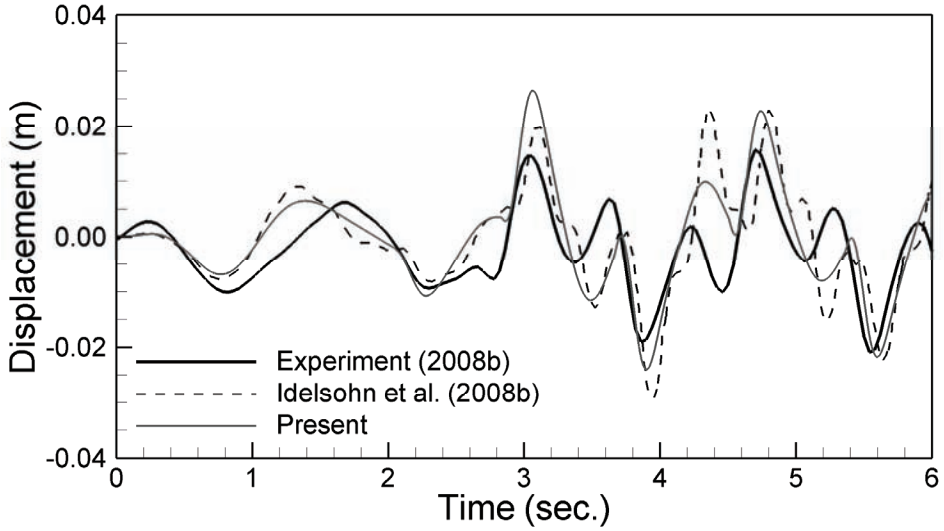

Figure 4.25 Comparison of the horizontal displacements at the middle of the bar for Case 3

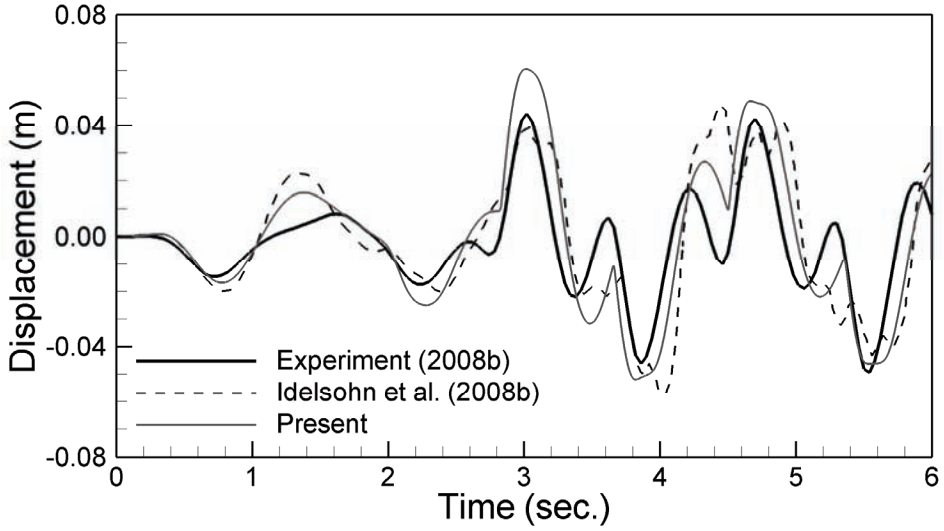

Figure 4.26 Comparison of the horizontal displacements at the tip of the bar for Case 3

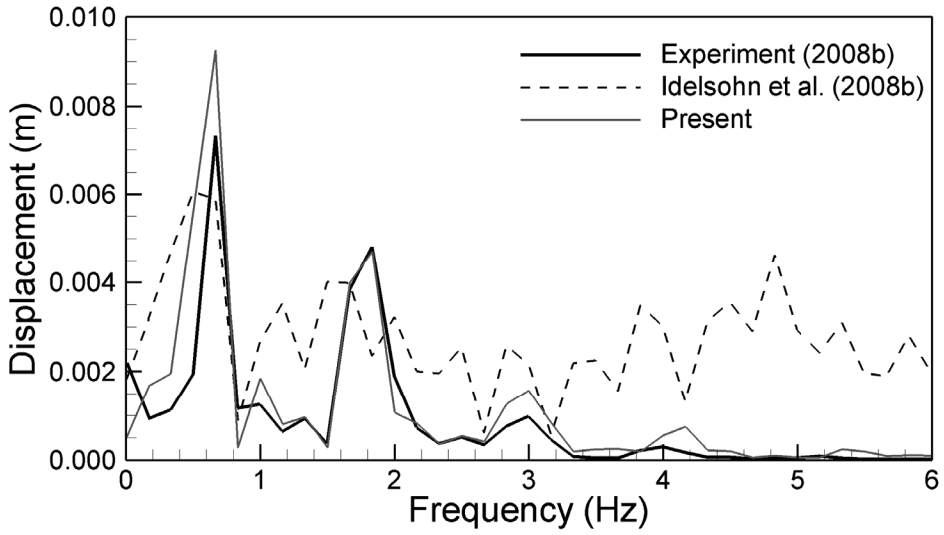

Figure 4.27 Spectral analysis for the horizontal displacements at the middle of the bar for Case 3

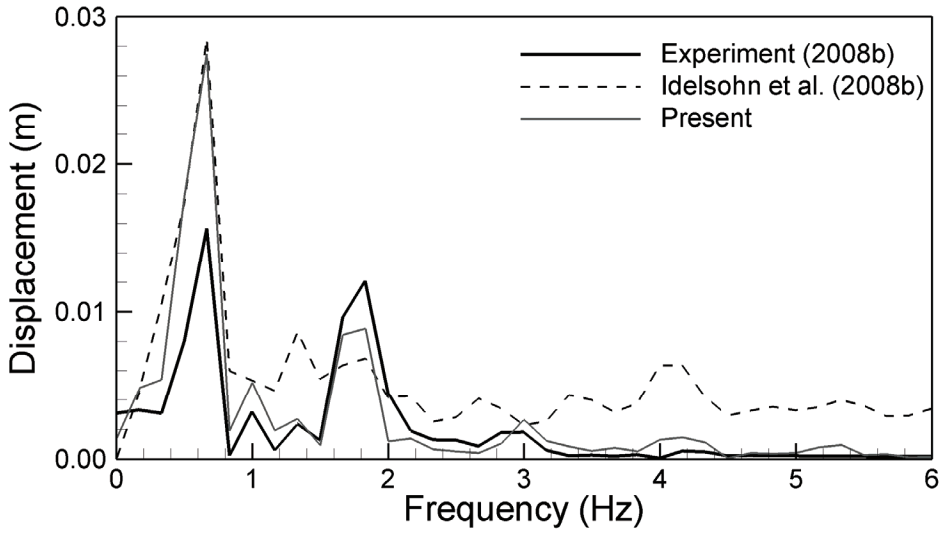

Figure 4.28 Spectral analysis for the horizontal displacements at the tip of the bar for Case 3

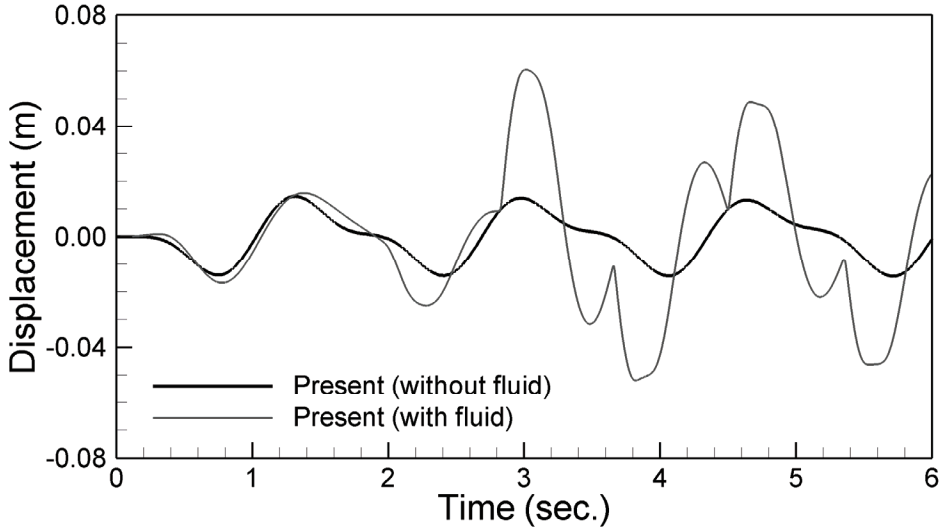

Figure 4.29 Comparison of the horizontal displacements at the bar tip in the cases with and without fluid for Case 3

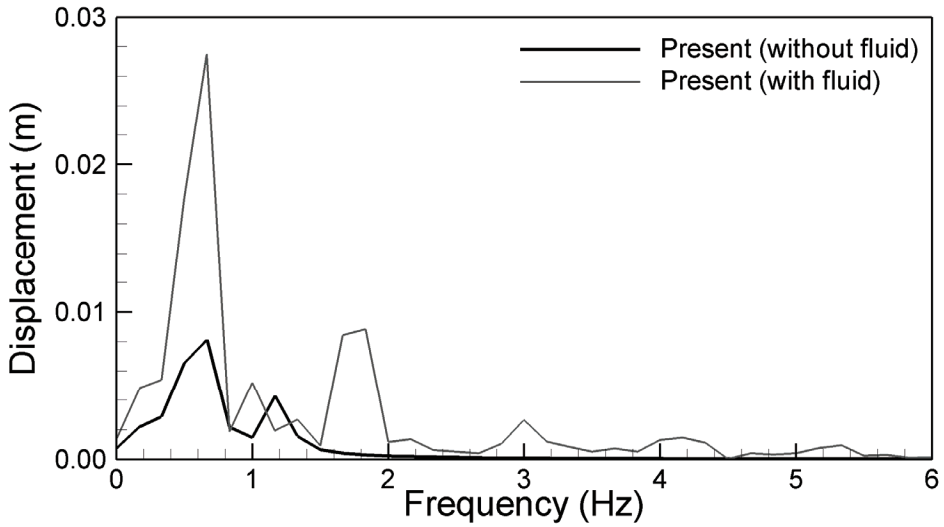

Figure 4.30 Comparison of the spectral analyses for the horizontal displacements at the bar tip in the cases with and without fluid for Case 3

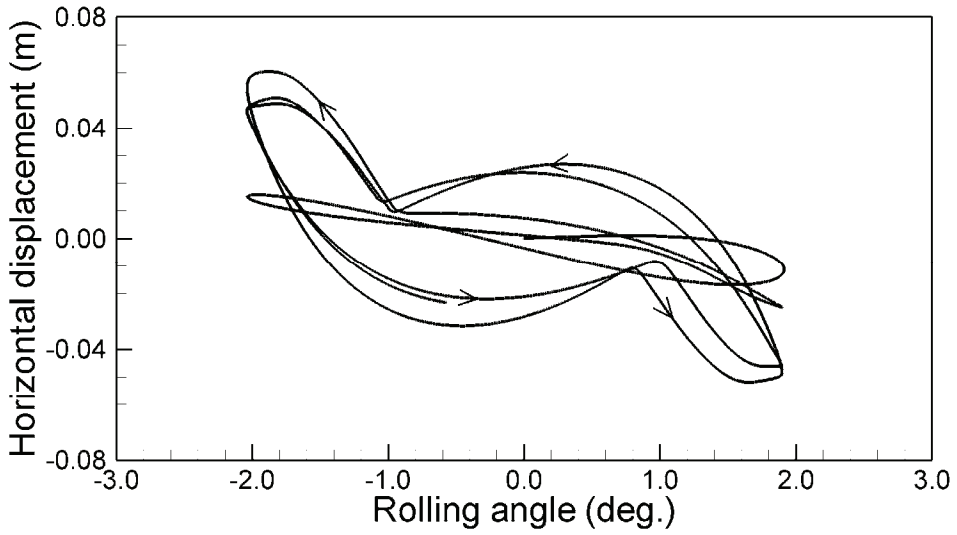

Figure 4.31 Trajectory of the horizontal displacement at the bar tip vs. the tank rolling angle for Case 3

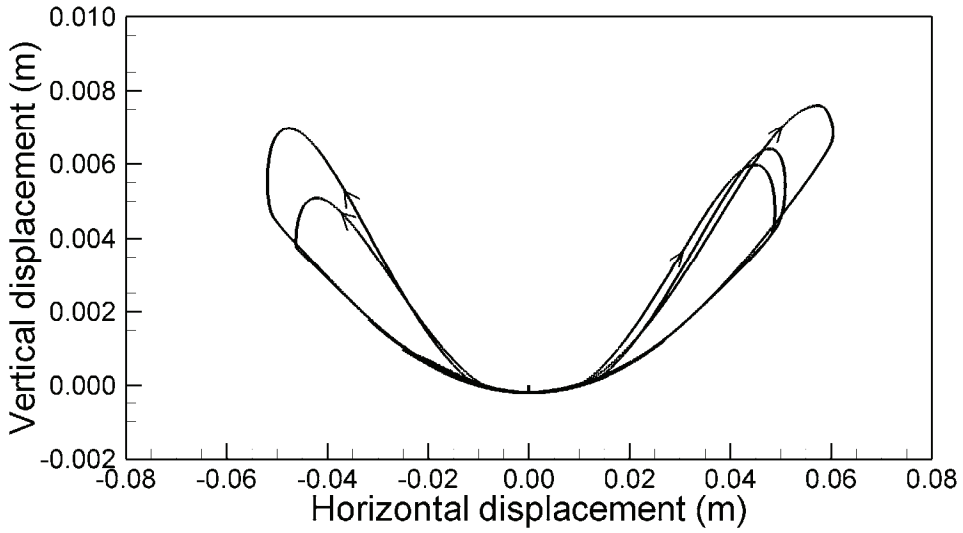

Figure 4.32 Trajectory of the tip displacement of the bar for Case 3

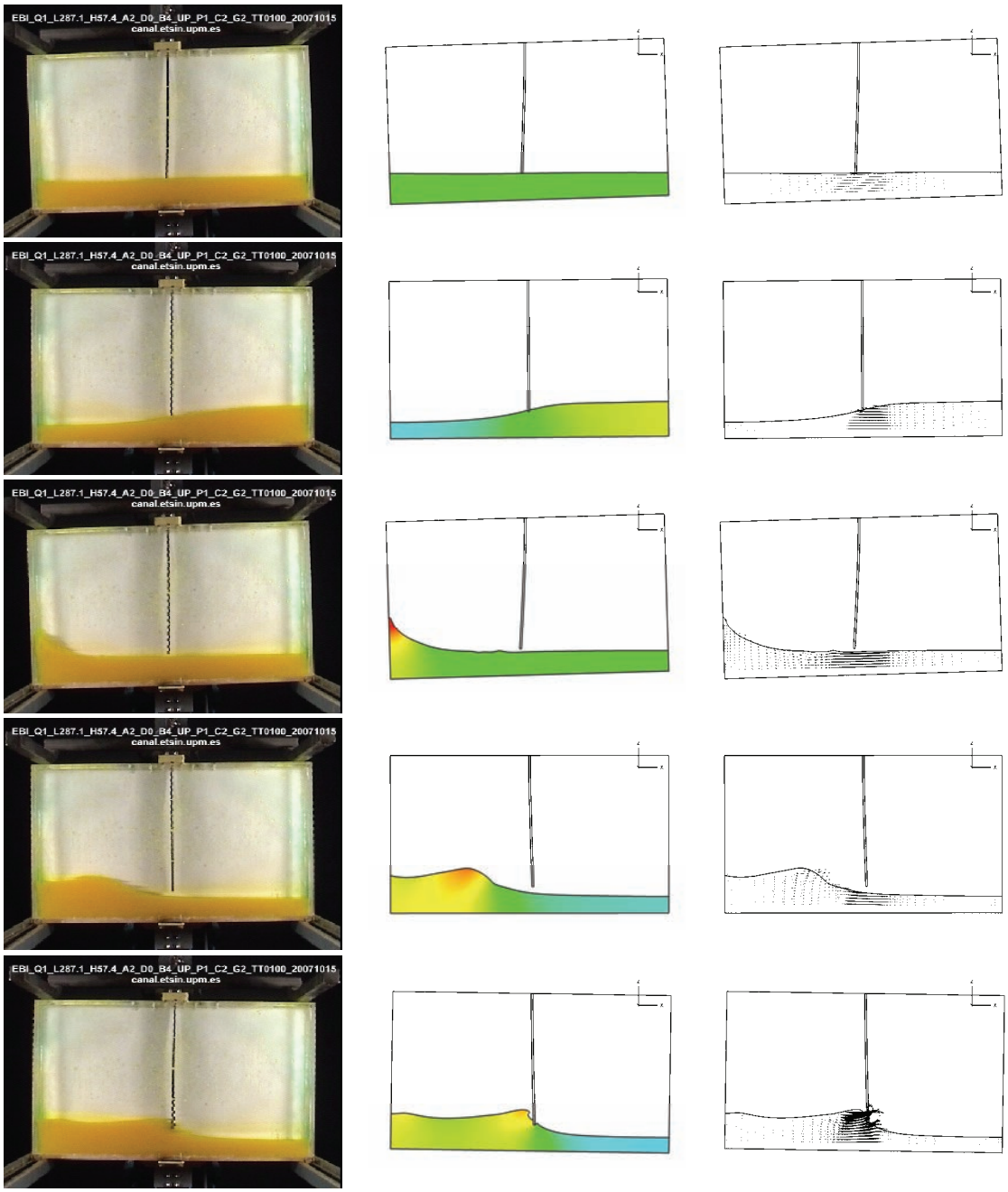

Figure 4.33 Comparison of the deformation of bar and the elevation of free surface vs. experiment (left) for Case 3: pressure contours (middle) and velocity vectors (right) at t=0.69, 1.95, 2.42, 2.69, 2.82, 3.02, 3.29, 3.55, 3.69, 3.89, 4.09, 4.42, 5.15, 5.35, and 5.55 seconds

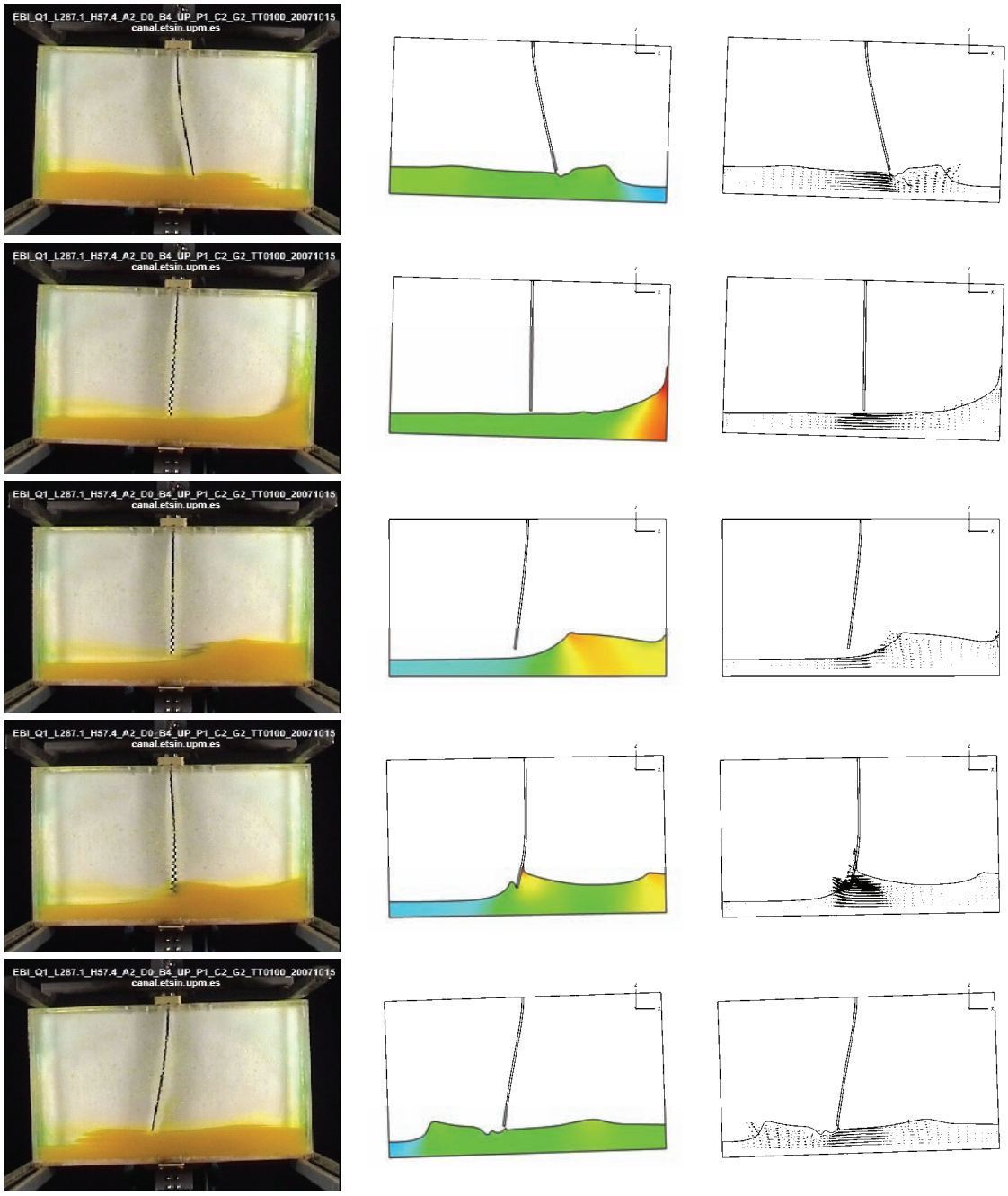

Figure 4.33 Continued

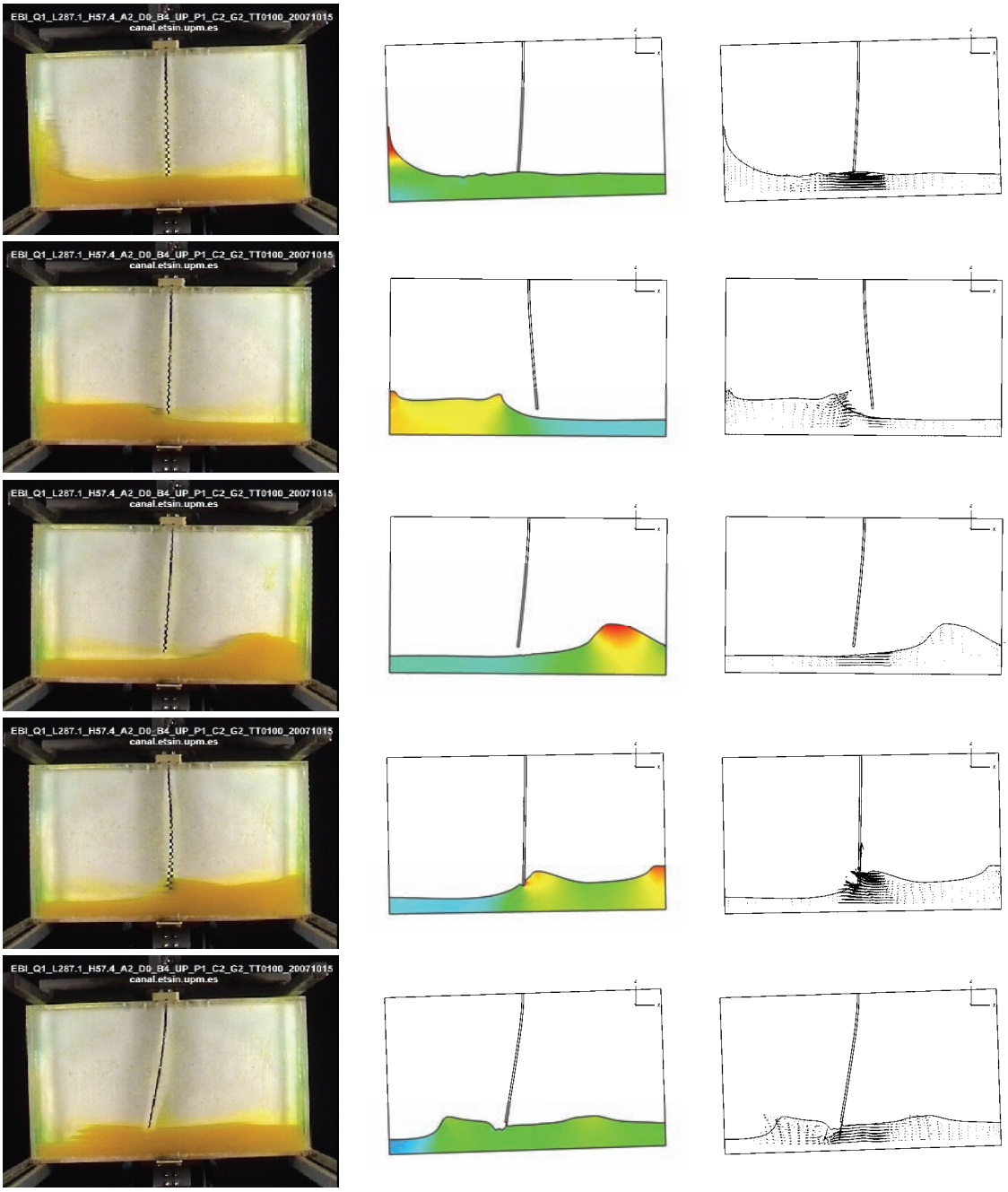

Figure 4.33 Continued

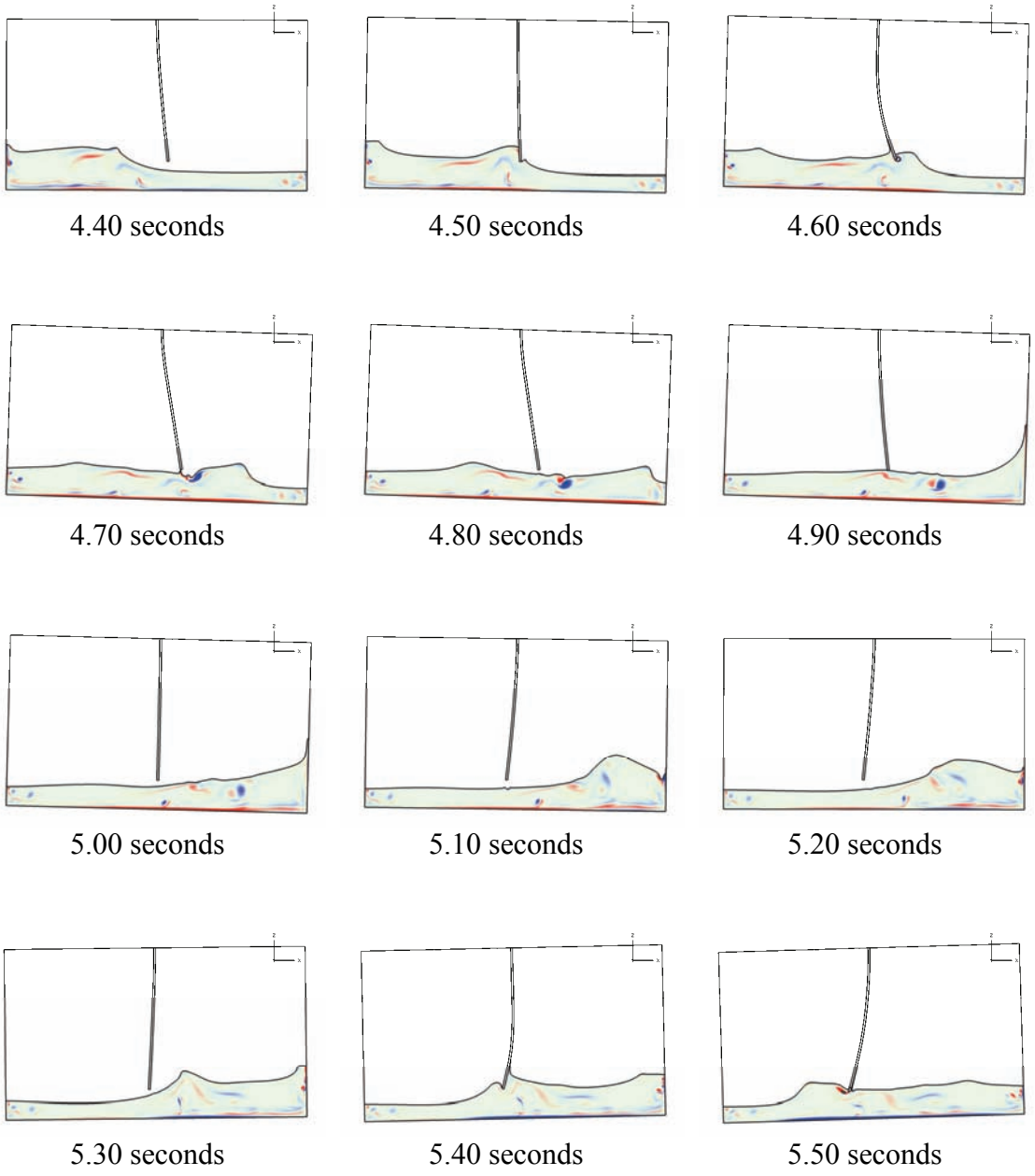

Figure 4.34 Sequential vorticity contours for Case 3

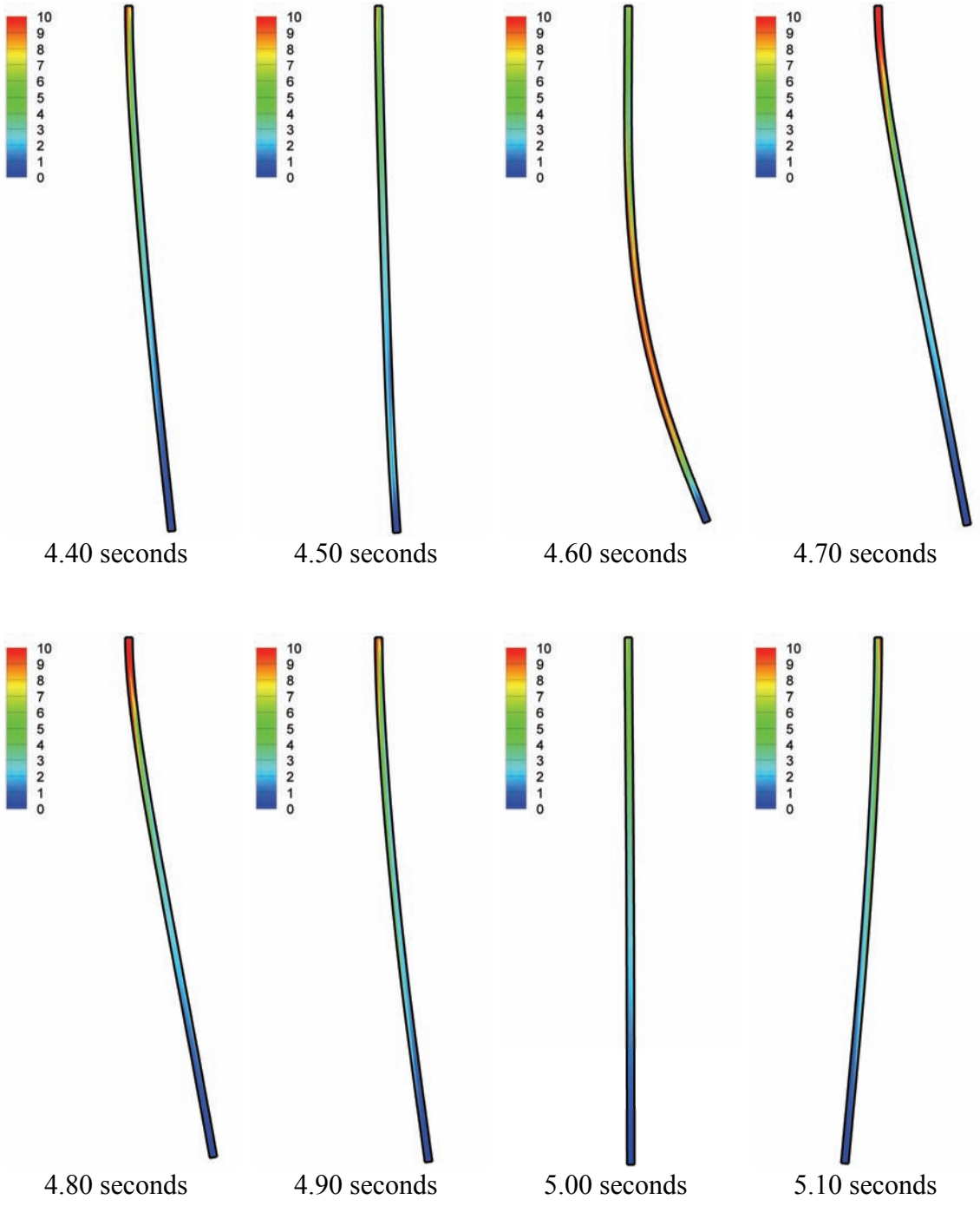

Figure 4.35 Sequential contours of the von Mises stress (unit: kPa) in the bar for Case 3

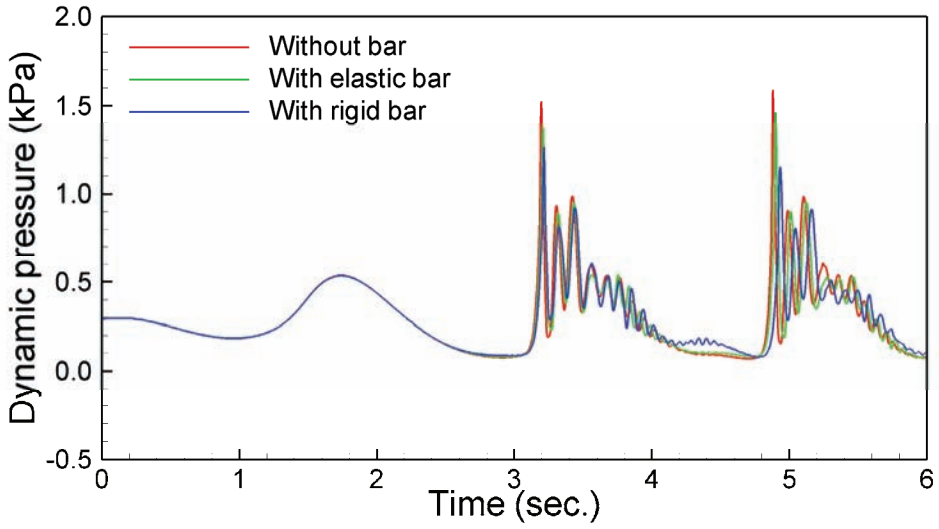

Figure 4.36 Comparison of the dynamic pressure histories at P1 vs. the bar rigidity for Case 3

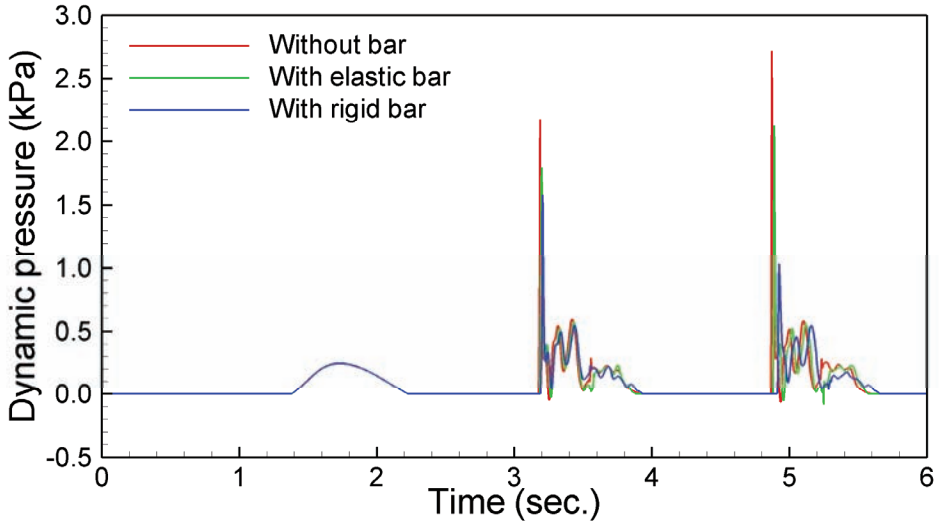

Figure 4.37 Comparison of the dynamic pressure histories at P2 vs. the bar rigidity for Case 3

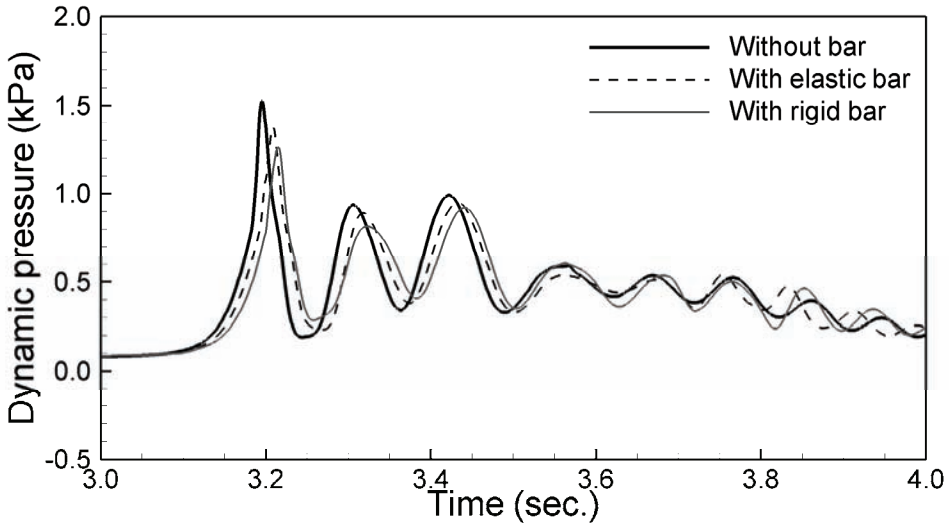

Figure 4.38 Zoom view around the second peak of the comparison of the dynamic pressure histories at P1 vs. the bar rigidity for Case 3

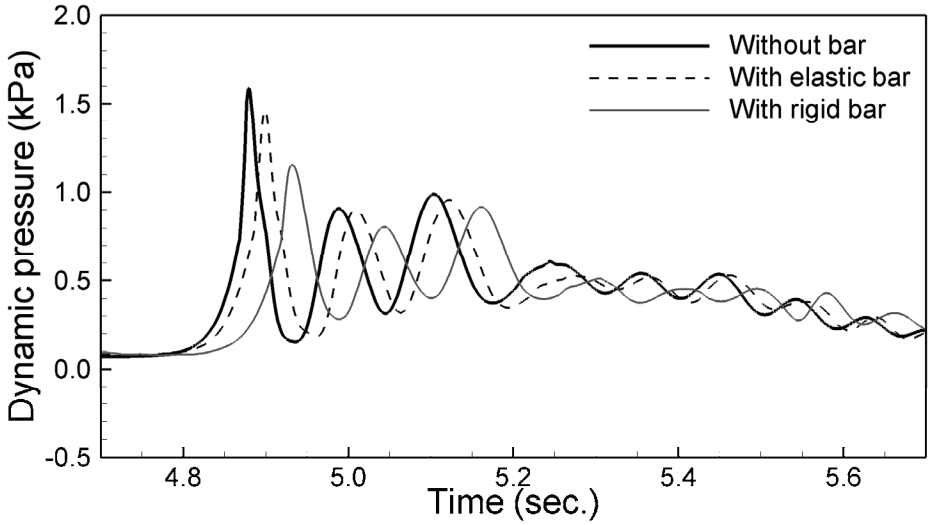

Figure 4.39 Zoom view around the third peak of the comparison of the dynamic pressure histories at P1 vs. the bar rigidity for Case 3

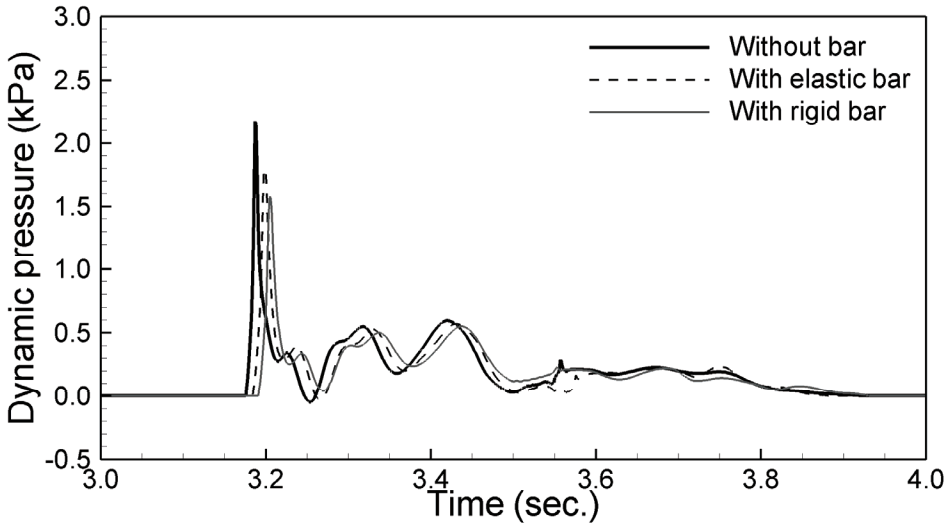

Figure 4.40 Zoom view around the second peak of the comparison of the dynamic pressure histories at P2 vs. the bar rigidity for Case 3

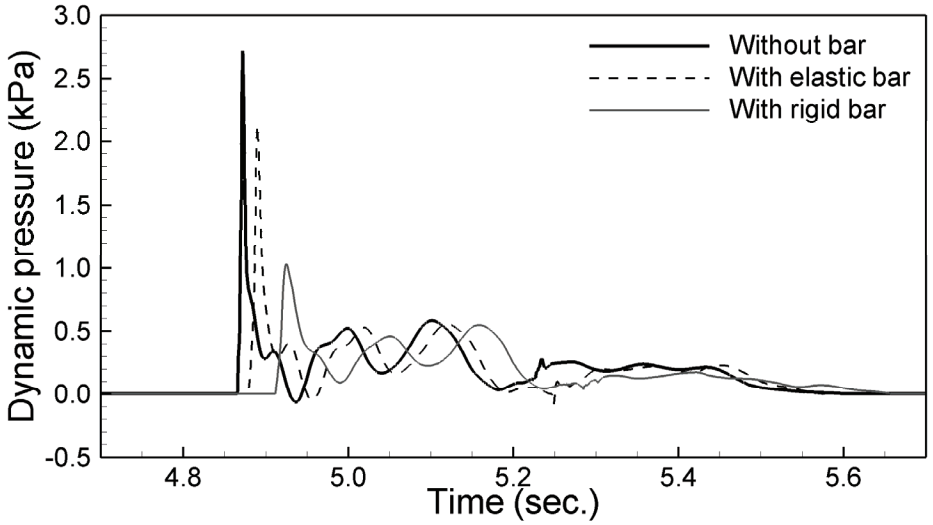

Figure 4.41 Zoom view around the third peak of the comparison of the dynamic pressure histories at P2 vs. the bar rigidity for Case 3

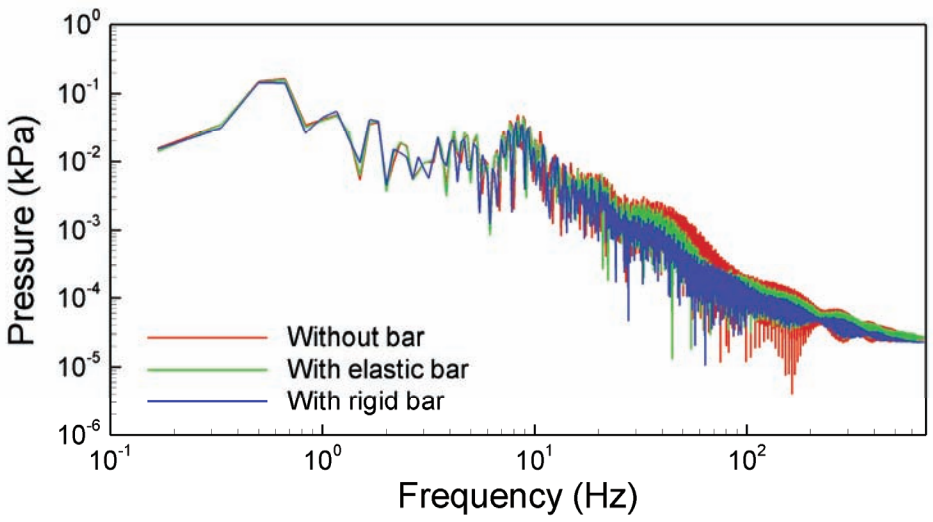

Figure 4.42 Spectral analysis of the dynamic pressure histories at P1 vs. the bar rigidity for Case 3

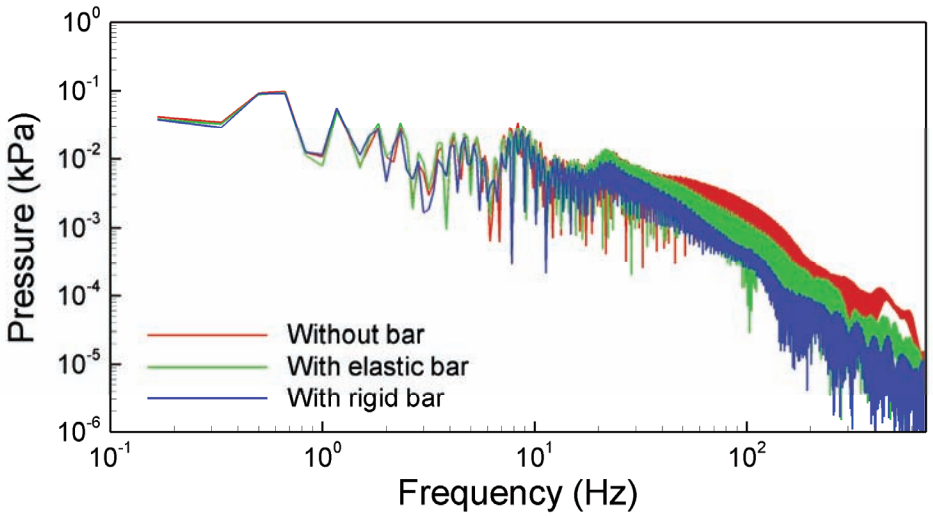

Figure 4.43 Spectral analysis of the dynamic pressure histories at P2 vs. the bar rigidity for Case 3

CHAPTER 5

CONCLUSIONS

Linear and nonlinear FSI methods to compute structural responses on surface ships or marine structures were presented. For the structure solver the modal superposition transient analysis was used for linear FSI problems and the nonlinear FEM structure solver was developed for large deformation FSI problems. The structure solver was coupled with CFDShip-Iowa version 4, which is a general-purpose URANS/DES overset fluid solver based on the Arbitrary Lagrangian–Eulerian (ALE) formulation.

The gluing method was applied to communicate the forces and displacements on non-matching grids for fluid and structure domains. The nodal forces on the structure grid were determined through Gauss integration using nine Gauss points which were associated to the nearest point on the fluid element. The displacements on the fluid grid node were projected from the associate point on the structure element. The forces and displacements on the associate points were interpolated using the Lagrange interpolation function.

For large deformation problems, the outer boundary of the boundary layer grid in the fluid domain was deformed using the linear FEM solver to minimize deterioration of the grid quality, which could occur due to large deformations of the structure surface. On the other hand, the outer boundary deformation of the fluid boundary layer grid was ignored in small deformation problems. Deformation of an interior point in the boundary layer grid was obtained using linear interpolation in both linear and nonlinear deformation problems.

As a linear problem the wave-induced structural loads on the S175 containership in regular waves were simulated and compared with experimental data. The natural

frequencies and mode shapes for the modal superposition were obtained from the commercial code ABAQUS version 6.8. The heave and pitch responses of the present simulation showed good agreement with the experiments. The time histories of VBM were calculated in the approaches of rigid model, one-way coupling, and two-way coupling. The VBMs predicted by the one-way and two-way coupling captured the ringing of the VBM observed in the experiments, which was caused principally due to bow flare slamming, while those phenomena were not observed in the rigid model. In general, the one-way coupling method showed similar results to the two-way coupling method. The effects of structural deformation on the amplitude and phase of VBM and the fluctuation of heave and pitch accelerations, however, were observed in the two-way approach.

Three sloshing tanks with an elastic bar clamped to bottom or top were simulated and compared with experiments to validate the FSI method developed for nonlinear problems with large deformations. Results were also compared with other numerical simulations using the PFEM. The present simulation results showed reasonable agreement with the experiments in the bar deformation and the free surface elevation, even though those had slightly larger amplitude of the bar deformation. The present simulation showed much better performance than the PFEM, especially, in the case interacting intricately with the free surface. It was observed by the vortical structure that a secondary wave was created by the vorticity generated at the free surface. To study the effect of the bar on the sloshing impact acting on the tank wall, a sloshing tank without bar was compared with sloshing tanks with an elatic bar or a rigid bar. The existence of the bar helped to reduce the impact pressure, and the rigid bar was more effective than the elastic bar. However, it remains further study of the problem in a three-dimension tank. Optimization of the geometry and rigidity of the bar are also necessary.

As future work, the transfer of forces and displacements between fluid and structure domains and the structure solver need to be peformed in multiple processors

based on MPI as done in the fluid solver. The current capability for nonlinear structure solver, limited to two-dimensional problems, should be extended to three-dimensions.

REFERENCES

Alonso, J. J., Jameson, A., 1994. Fully-implicit time-marching aeroelastic solutions. *AIAA Paper* 94-0056.

Antoci, C., Gallati, M., Sibilla, S., 2007. Numerical simulation of fluid–structure interaction by SPH. *Computers & Structures* 85, 879-890.

Balay, S., Buschelman, K., Gropp, W., Kaushik, D., Knepley, M., Curfman, L., Smith, B., Zhang, H., 2002. *PETSc User Manual*. ANL-95/11-Revision 2.1.5, Argonne National Laboratory.

Bathe, K.-J., Zhang, H., 2004. Finite element developments for general fluid flows with structural interactions. *International Journal for Numerical Methods in Engineering* 60, 213-232.

Batina, J., 1990. Unsteady Euler airfoil solutions using unstructured dynamic meshes. *AIAA Journal* 28, 1381-1388.

Bhatti, M. A., 2006. *Advanced Topics in Finite Element Analysis of Structures*. Wiley, New York, NY.

Bletzinger, K.-U., Wüchner, R., Kupzok, A., 2006. Algorithmic treatment of shells and free form-membranes in FSI. *Lecture Notes in Computational Science and Engineering* 53, 336-355. Springer.

Blom, F. J., 1998. A monolithical fluid–structure interaction algorithm applied to the piston problem. *Computer Methods in Applied Mechanics and Engineering* 167, 369-391.

Blom, F. J., Leyland, P., 1998. Analysis of fluid–structure interaction by means of dynamic unstructured meshes. *Journal of Fluids Engineering* 120, 792-798.

Braess, H., Wriggers, P., 2000. Arbitrary Lagrangian Eulerian finite element analysis of free surface flow. *Computer Methods in Applied Mechanics and Engineering* 190, 95-109.

Carrica, P. M., Wilson, R. V., Stern, F., 2007a. An unsteady single-phase level set method for viscous free surface flows. *International Journal for Numerical Methods in Fluids* 53, 229-256.

Carrica, P. M., Wilson, R. V., Noack, R. W., Stern, F., 2007b. Ship motions using single-phase level set with dynamic overset grids. *Computers & Fluids* 36, 1415-1433.

Carrica, P. M., Paik, K.-J., Hosseini, H. S., Stern, F., 2008. URANS analysis of a broaching event in irregular quartering seas. *Journal of Marine Science and Technology* 13, 395-407.

Cavagna, L., Quaranta, G., Ghiringhelli, G. L., Mantegazza, P., 2005. Efficient application of CFD aeroelastic methods using commericial software. *International Forum on Aeroelasticity and Structural Dynamics IFASD-2005*, Germany.

Chaplin, J. R., Rainey, R. C. T., Yemm, R. W., 1997. Ringing of a vertical cylinder in waves. *Journal of Fluid Mechanics* 350, 119-147.

Chen, X., Zha, G.-C., Yang, M.-T., 2007. Numerical simulation of 3-D wing flutter with fully coupled fluid–structure interaction. *Computers & Fluids* 36, 856-867.

Chen, Y. G., Djidjeli, K., Price, W. G., 2009. Numerical simulation of liquid sloshing phenomena in partially filled containers. *Computers & Fluids* 38, 830-842.

Cho, J. R., Lee, S. Y., 2003. Dynamic analysis of baffled fuel-storage tanks using the ALE finite element method. *International Journal for Numerical Methods in Fluids* 41, 185-208.

Degand, C., Farhat, C., 2002. A three-dimensional torsional spring analogy method for unstructured dynamic meshes. *Computers & Structures* 80, 305-316.

Delorme, L., Souto Iglesias, A., Abril Pérez, S., 2005. Sloshing loads simulation in LNG tankers with SPH. *International Conference on Computational Methods in Marine Engineering*, MARINE 2005.

Donea, J., Giuliani, S., Halleux, J. P., 1982. An arbitrary Lagrangian–Eulerian finite element method for transient dynamic fluid-structure interactions. *Computer Methods in Applied Mechanics and Engineering* 33, 689-723.

Duggal, A. S., Niedzwecki, J. M., 1995. Dynamic response of a single flexible cylinder in waves. *Journal of Offshore Mechanics and Arctic Engineering* 117, 99-104.

Dunne, T., Rannacher, R., 2006. Adaptive finite element approximation of fluid–structure interaction based on an Eulerian variational formulation. *Lecture Notes in Computational Science and Engineering* 53, 110-145. Springer.

Engel, M., Griebel, M., 2006. Flow simulation on moving boundary-fitted grids and application to fluid-structure interaction problems. *International Journal for Numerical Methods in Fluids* 50, 437-468.

Faltinsen, O. M., 2000. Hydroelastic slamming. *Journal of Marine Science and Technology* 5, 49-65.

Farhat, C., Lesoinne, M., Maman, N., 1995. Mixed explicit/implicit time integration of coupled aeroelastic problems: there-field formulation, geometric conservation and distributed solution. *International Journal for Numerical Methods in Fluids* 21, 807-835.

Farhat, C., Lesoinne, M., LeTallec, P., 1998a. Load and motion transfer algorithms for fluid/structure interaction problems with non-matching discrete interfaces: momentum and energy conservation, optimal discretization and application to aeroelasticity. *Computer Methods in Applied Mechanics and Engineering* 157, 95-114.

Farhat, C., Degand, C., Koobus, B., Lesoinne, M., 1998b. Torsional springs for two-dimensional dynamic unstructured fluid meshes. *Computer Methods in Applied Mechanics and Engineering* 163, 231-245.

Farhat, C., Geuzaine, P., Brown, G., 2003. Application of a three-field nonlinear fluid–structure formulation to the prediction of the aeroelastic parameters of an F-16 fighter. *Computers & Fluids* 32, 3-29.

Feng, Z., Soulaïmani, A., 2006. Nonlinear aeroelasticity computations in transonic flows using tightly coupling algorithms. *2006 ASME Pressure Vessels and Piping Division Conference*, Canada.

Feng, Z., Soulaïmani, A., 200. Nonlinear aeroelasticity modeling using a reduced order model based on proper orthogonal decomposition. *2007 ASME Pressure Vessels and Piping Division Conference*, USA.

Fonseca, N., Guedes Soares, C., 1998. Time-domain analysis of large-amplitude vertical ship motions and wave loads. *Journal of Ship Research* 42, 139-153.

Fonseca, N., Guedes Soares, C., 2002. Comparison of numerical and experimental results of nonlinear wave-induced vertical ship motions and loads. *Journal of Marine Science and Technology* 6, 193-204.

Fonseca, N., Guedes Soares, C., 2004a. Validation of a time-domain strip method to calculate the motions and loads on a fast monohull. *Applied Ocean Research* 26, 256-273.

Fonseca, N., Guedes Soares, C., 2004b. Experimental investigation of the nonlinear effects on the vertical motions and loads of a containership in regular waves. *Journal of Ship Research* 48, 118-147.

Fonseca, N., Guedes Soares, C., 2004c. Experimental investigation of the nonlinear effects on the statistics of vertical motions and loads of a containership in irregular waves. *Journal of Ship Research* 48, 148-167.

Fonseca, N., Guedes Soares, C., 2005. Comparison between experimental and numerical results of the nonlinear vertical ship motions and loads on a containership in regular waves. *International Shipbuilding Progress* 52, 57-89.

Gingold, R. A., Monaghan, J. J., 1977. *Monthly Notices of the Royal Astronomical Society* 181, 375.

Glück, M., Breuer, M., Durst, F., Halfmann, A., Rank, E., 2001. Computation of fluid-structure interaction on lightweight structures. *Journal of Wind Engineering and Industrial Aerodynamics* 89, 1351-1368.

Greco, M., Landrini, M., Faltinsen, O. M., 2004. Impact flows and loads on ship-deck structures. *Journal of Fluids and Structures* 19, 251-275.

Hansen, M. H., 2007. Aeroelastic instability problems for wind turbines. *Wind Energy* 10, 551-577.

Hron, J., Mádlík, M., 2007. Fluid-structure interaction with applications in biomechanics. *Nonlinear Analysis* 8, 1431-1458.

Idelsohn, S. R., Oñate, E., Del Pin, F., Calvo, N., 2006. Fluid–structure interaction using the particle finite element method. *Computer Methods in Applied Mechanics and Engineering* 195, 2100-2123.

Idelsohn, S. R., Marti, J., Limache, A., Oñate, E., 2008a. Unified Lagrangian formulation for elastic solids and incompressible fluids: Application to fluid–structure interaction problems via the PFEM. *Computer Methods in Applied Mechanics and Engineering* 197, 1762-1776.

Idelsohn, S. R., Marti, J., Souto Iglesias, A., Oñate, E., 2008b. Interaction between an elastic structure and free-surface flows: experimental versus numerical comparisons using the PFEM. *Computational Mechanics* 43, 125-132.

Ishihara, D., Yoshimura, S, 2005. A monolithic approach for interaction of incompressible viscous fluid and an elastic body based on fluid pressure Poisson equation. *International Journal for Numerical Methods in Engineering* 64, 167-203.

Issa, R. I., 1986. Solution of the implicit discretized fluid flow equations by operator-splitting. *Journal of Computational Physics* 62, 40-65.

Kirk, C. L., Etok, E. U., Cooper, M. T., 1979. Dynamic and static analysis of a marine riser. *Applied Ocean Research* 1,125-135.

Koshizuka, S., Oka, Y., 1996. Moving particle semi-implicit method for fragmentation of incompressible fluid. *Nuclear Science and Engineering* 123, 2649-2667.

Kuhl, E., Hulshoff, S., de Borst, R., 2003. An arbitrary Lagrangian Eulerian finite-element approach for fluid–structure interaction phenomena. *International Journal for Numerical Methods in Engineering* 57, 117-142.

Le Cunff, C., Biolley, F., Fontaine, E., Étienne, S., Facchinetti, M. L., 2002. Vortex-induced vibrations of risers: theoretical, numerical and experimental investigation. *Oil & Gas Science and Technology* 57, 59-69.

Lee, T.-H., Zhou, Z., Cao, Y., 2002. Numerical simulations of hydraulic jumps in water sloshing and water impacting. *Journal of Fluids Engineering* 124, 215-226.

Lee, C. J. K., Noguchi, H., Koshizuka, S., 2007. Fluid–shell structure interaction analysis by coupled particle and finite element method. *Computers & Structures* 85, 688-697.

Liu, C., Walkington, N. J., 2001. An Eulerian description of fluids containing visco-elastic particles. *Archive for Rational Mechanics and Analysis* 159, 229-252.

Lu, Y., Chai, S., 2008. CFD simulation and engineering mitigation of liquid sloshing in topside process vessel on floating production platform. *The 2008 SPE Annual Technical Conference and Exhibition*, Colorado, USA.

Lucy, L. B., 1977. A numerical approach to the testing of the fission hypothesis. Astronomical Journal 82, 1013-1024.

Lv, X., Zhao, Y., Huang, X. Y., Xia, G. H., Su, X. H., 2007. A matrix-free implicit unstructured multigrid finite volume method for simulating structural dynamics and fluid-structure interaction. *Journal of Computational Physics* 225, 120-144.

Maess, M. K., Gaul, L., 2007. Simulation of structural deformations of flexible piping systems by acoustic excitation. *Journal of Pressure Vessel Technology* 129, 363-371.

Maman, N., Farhat, C., 1995. Matching fluid and structure meshes for aeroelastic computations: a parallel approach. *Computers & Structures* 54, 779-785.

Markou, G. A., Mouroutis, Z. S., Charmpis, D. C., Papadrakakis, M., 2007. The ortho-semi-torsional (OST) spring analogy method for 3D mesh moving boundary problems. *Computer Methods in Applied Mechanics and Engineering* 196, 747-765.

Melville, R. B., Morton, S. A., Rizzetta, D. P., 1997. Implementation of a fully-implicit aeroelastic Navier–Stokes solver. *AIAA Paper* 97-2039.

Mendes, P. A., Branco, F. A., 1999. Analysis of fluid–structure interaction by an arbitrary Lagrangian–Eulerian finite element formulation. *International Journal for Numerical Methods in Fluids* 30, 897-919.

Menter, F. R., 1994. Two-equation eddy viscosity turbulence models for engineering applications. *AIAA Journal* 32, 1598-1605.

Monaghan, J. J., 1994. Simulating free surface flows with SPH. *Journal of Computational Physics* 110, 399-406.

Newmark, N. M., 1959. A method of computation for structural dynamics. *Journal of the Engineering Mechanics Division, Proceedings of the American Society of Civil Engineers*, 67-94.

O'Dea, J., Powers, E., Zselecsky, J., 1992. Experimental determination of non-linearities in vertical plane ship motions. *Proceedings of the 19th Symposium on Naval Hydrodynamics*, Seoul, Korea, pp. 73-91.

Piperno, S., Farhat, C., Larrouturou, B., 1995. Partitioned procedures for the transient solution of coupled aeroelastic problems Part I: Model problem, theory and two-dimensional application. *Computer methods in Applied Mechanics and Engineering* 124, 79-112.

Ramos, J., Guedes Soares, C., 1998. Vibratory response of ship hulls to wave impact loads. *International Shipbuilding Progress* 45, 71-87.

Ramos J., Incecik A., Guedes Soares C., 2000. Experimental study of slam-induced stresses in a containership. *Marine Structures* 13, 25-51.

Sakamoto, N., Carrica, P. M., Stern. F., 2008. URANS and DES simulation of static and dynamic maneuvering for surface combatant, *Proceedings of SIMMAN 2008*, Lyngby, Denmark.

Sames, P. C., Schellin, T. E., Muzaferija, S., Peric, M., 1999. Application of a two-fluid finite volume method to ship slamming. *Journal of Offshore Mechanics and Arctic Engineering* 121, 47-52.

Schäfer, M., Heck, M., Yigit, S., 2006. An implicit partitioned method for the numerical simulation of fluid–structure interaction. *Lecture Notes in Computational Science and Engineering* 53, 171-194. Springer.

Shi, X., Lim, S. P., 2007. A LBM-DLM/FD method for 3D fluid–structure interactions. *Journal of Computational Physics* 226, 2028-2943.

Shin, Y., Kim, J. W., Lee, H., Hwang, C., 2003. Sloshing impact of LNG cargoes in membrane containment systems in the partially filled condition. *Proceedings of The Thirteenth International Offshore and Polar Engineering Conference*, Hawaii, USA, 509-515.

Sigrist, J.-F., Garreau, S., 2007. Dynamic analysis of fluid-structure interaction problems with modal methods using pressure-based fluid finite elements. *Finite Elements in Analysis and Design* 43, 287-300.

Singh, S. P., Sen, D., 2007. A comparative linear and nonlinear ship motion study using 3-D time domain methods. *Ocean Engineering* 34, 1863-1881.

Souto Iglesias, A., Pérez Rojas, L., Zamora Rodríguez, R., 2004. Simulation of anti-roll tanks and sloshing type problems with smoothed particle hydrodynamics. *Ocean Engineering* 31, 1169-1192.

Souto Iglesias, A., Delorme, L., Pérez Rojas, L., Abril Pérez, S., 2006. Liquid moment amplitude assessment in sloshing type problems with smooth particle hydrodynamics. *Ocean Engineering* 33, 1462-1484.

Stein, K., Tezduyar, T., Benney, R., 2003. Mesh moving techniques for fluid–structure interactions with large displacements. *Journal of Applied Mechanics* 70, 58-63.

Watanabe, I., Ueno, M., Sawada, H., 1989. Effects of bow flare shape to the wave loads of a container ship. *Journal of the Society of Naval Architects of Japan* 166, 259-266.

Xia, G., Lin, C.-L., 2008, An unstructured finite volume approach for structural dynamics in response to fluid motions. *Computers & Structures* 86, 684-701.

Zeng, D., Ethier, C., 2005. A semi-torsional spring analogy model for updating unstructured meshes in 3D moving domains. *Finite Elements in Analysis and Design* 41, 1118-1139.